DETERMINATION AND QUANTITATIVE EVALUATION OF IMAGE-BASED REGISTRATION ACCURACY FOR ROBOTIC NEUROSURGERY

by

JENNIFER RUTH CUTTER

A thesis submitted to the University of Birmingham for the degree of
DOCTOR OF PHILOSOPHY

PSIBS Doctoral Training Centre

College of Engineering and Physical Sciences

University of Birmingham

September 2017

Abstract

Stereotactic neurosurgical robots allow quick, accurate location of small targets within the brain, relying on accurate registration of preoperative MRI/CT images with patient and robot coordinate systems. Fiducial markers or a stereotactic frame are used as registration landmarks and the patient's head is fixed in position. An image-based system could be quick, non-invasive and allow the head to be moved during surgery giving greater ease of access. Submillimetre surgical precision at the target point is required.

The in-house Birmingham surface capture system, which uses structured light to image 3D surfaces, was tested in a phantom study and attained a median distance of 0.269 mm from the ground truth. Three registration algorithms are tested for accuracy in registering representative surface point clouds. Full volume point clouds extracted from MRI data are used to assess the absolute error within the head resulting from surface registration.

An octant representation is utilized to investigate full region of interest (ROI) head registration using parts only, with registration performed using the Iterative Closest Point (ICP) algorithm. Use of two octants sequentially obtained a mean RMS distance of 0.813±0.026 mm ([mean]±[standard deviation]); adding subsequent octants did not significantly improve performance. An RMS distance of 0.812±0.025 mm was obtained for three octants used simultaneously.

ICP was compared with Coherent Point Drift, and 3D Normal Distribution Transform, with and without added or smoothed noise, and was least affected by starting position or noise added; a mean accuracy of 0.884±0.050 mm across ten noise levels and four starting positions was achieved, which was shown to translate to submillimetre accuracy at points within the head. The mean time taken by ICP to perform these registrations was 286±181 s. This corresponded to 67.2±35.1 iterations of the algorithm. ICP surface registration from multiple starting points was shown to correspond to a median accuracy at points within the head of 0.272±0.066 mm.

To my parents, John and Valerie, and my brother, David, with deepest gratitude for all your love and support over the years.

Acknowledgements

I would like to thank my supervisors Hamid Dehghani, Iain Styles and Aleš Leonardis for all their help and encouragement with this project. I am also grateful to Rob Harrison, Emma Portman and Stephen Anderson at Renishaw plc for their advice, expertise and practical assistance.

I am grateful to past and present members of the CS imaging group, in particular to Hector Basevi for help with surface capture imaging, Xue Wu for helping me process MRI data, Sean Bastable for helping me install PCL when I was at my wits' end, and Sophie Glinton for tea and general encouragement. Thank you to my PSIBS 'buddies', Emma Lonnen and Naomi Waterman for providing support and sympathy, and sitting through my meetings. I am also grateful to Elizabeth Randall and Shelley Taylor for reading work for me and encouraging me to keep going, and to everyone at the PSIBS and Sci-Phy CDT who ate lunch with me, made cakes, and cheered me up when I needed it.

I also wish to sincerely thank my oldest friends, Cathy Stewart and Julia Merchant, for always being there for me.

I gratefully acknowledge financial support from the EPSRC through a studentship from the PSIBS Doctoral Training Centre (EP/F50053X/1).

Contents

List of Figures

List of Tables

List of Abbreviations

3D-NDT	**3D N**ormal **D**istribution **T**ransform
CPD	**C**oherent **P**oint **D**rift (algorithm)
CSF	**C**erebro**s**pinal **F**luid
CT	**C**omputed **T**omography
DBS	**D**eep **B**rain **S**timulation
DRR	**D**igitally **R**econstructed **R**adiograph
EM	**E**xpectation-**M**aximisation
ES	**E**lectrical **S**timulation
ET	**E**ssential **T**remor
GMM	**G**aussian **M**ixture **M**odel
ICP	**I**terative **C**losest **P**oint (algorithm)
IR	**I**nfra**r**ed
LINAC	**Lin**ear Particle **Ac**celerator
MR	**M**agnetic **R**esonance
MRI	**M**agnetic **R**esonance **I**maging
PCA	**P**rincipal **C**omponent **A**nalysis
PDF	**P**robability **D**ensity **F**unction
PET	**P**ositron **E**mission **T**omography
RMS	**R**oot **M**ean **S**quare
ROI	**R**egion **O**f **I**nterest
SDK	**S**oftware **D**evelopment **K**it
SEEG	**S**tereotactic **E**lectro**e**ncephalo**g**raphy
SPECT	**S**ingle-**P**hoton **E**mission **C**omputerized **T**omography
SVD	**S**ingular **V**alue **D**ecomposition
US	**U**ltra**s**ound
VBH	**V**ogele-**B**ale-**H**ohner (registration device)

Chapter 1

Introduction

1.1 Stereotactic neurosurgery

Stereotactic neurosurgery is a technique in which targets within the head are located based on their coordinates, in order to perform actions such as ablation, biopsy and injection; it was first applied to humans in the late 1940s. Spiegel et al. [1] describe the adaptation for humans of a stereotactic frame developed by Horsley and Clarke [2] in 1908. The technique allows small targets within the head to be accurately reached without the need for open brain surgery. Choosing the best route to the target is important in order to avoid damage to eloquent areas of the brain (the parts of the brain which control motor functions, speech, and senses).

Stereotactic neurosurgery allows procedures such as biopsy [3], neuroendoscopy [4] and electroencephalography [5] to be performed accurately and minimally invasively (see section 2.3). Use of a stereotactic robot can improve speed and accuracy by removing the need to locate manually the required entry point and direction for each action on the patient's head; for this, accurate registration (spatial alignment) between the patient, robot, and preoperative images is needed. A stereotactic frame or fiducial markers [6] can provide physical landmarks for preoperative registration; the frame also keeps the patient's head in place throughout the surgical procedure [7]. However, if registration could be performed quickly and accurately using a simple, image-based technique such as 3D surface capture, it would allow the head to be moved during surgery to a more convenient position and re-registered, allowing the surgical plan to be adjusted accordingly. The lack of features in the proposed imaging area (the back and top of the head) makes the problem more difficult.

1.2 Surgical robotics

Surgical robotics is still a relatively new and expanding field. It is believed that the first clinical use of a robot occurred in 1985, when an industrial robot was used stereotactically to assist in a brain biopsy [8, 9]. Due to safety concerns, work with this initial robot (a Puma 560) was discontinued and robots began to be designed specifically for surgical purposes [10].

Surgical robots can be used in various ways, for different purposes. This work focuses on stereotactic robots, which work solely using coordinates: the robot is instructed to move to, or perform an action at, a particular point within its coordinates system. Therefore, in order for surgery to be successfully performed, accurate registration is required between the coordinate systems of the robot, patient and preoperative images, such that for any target coordinate identified on a preoperative image, the corresponding coordinates in the other two systems can be accurately determined.

Stereotactic robots are particularly suitable for use in neurosurgery as the skull provides a rigid frame allowing relatively little movement within the brain, so the coordinates of a target point remain fixed. In the rest of the body target points are less likely to have a fixed coordinate and robots which are directly guided by the surgeon based on visual and haptic feedback are more suitable. Some examples of surgical robots which require registration are given in section 2.2.

1.3 Registration

Registration is the process of bringing different images of an object or scene into spatial alignment. The images may be taken from different directions, at different times and/or using different modalities. Medical imaging modalities might include X-ray, CT, MRI, ultrasound, PET and many others, which can provide complementary information about the patient; registration can allow useful integration of the different types of data.

In stereotactic surgery accurate registration is particularly important because it allows any chosen point on the preoperative images to be physically located on or within the patient. The patient's coordinate system may defined with reference to a stereotactic frame fixed to the patient's head and this must be registered in theatre to preoperative images and, if used, the robot's coordinate system. To do this, a correspondence between the images must be established. This can be feature-based, in which features or landmarks such as regions, lines or points are identified within both images, or area/intensity-based, in which the full image or subimages are used and correlations are sought between intensity patterns in the images. Frequency or Fourier based registration methods also exist. Features or landmarks must be visible in both modalities used in registration to be useful. Landmarks used for registration in stereotactic neurosurgery are discussed in section 2.1.6. One image is treated as the 'reference' image and the other as the 'source' (also known as the 'sensed' image); a transformation must be determined to bring the source into the best possible alignment with the reference.

Various algorithms exist to calculate this transformation, depending on the type of data being registered: these are discussed in section 2.1. [11, 12]

In this work, registration between two 3D images is considered, although registration between a 2D and a 3D image, or between two 2D images may be possible with the same methods. It is assumed that there is no change in the subject over the time period between the images being taken. The work aims to explore the possibility of registration between a surface capture image and preoperative MRI/CT images. Surface capture devices commonly produce (at least in raw data form) a set of coordinates at which the surface has been measured, also known as a point cloud. A surface point cloud can also be extracted from MRI/CT data, so the following work focuses on methods for registration of surface point clouds.

1.3.1 Transformation models

Once the correspondence between images has been established, the transformation required to bring the source image into optimal spatial alignment with the reference image must be estimated. The transformation model will depend on the nature of the images. Transformations can be linear or elastic: the former preserves straight lines and planes, whereas the latter allows local distortion. Linear transformations can be rigid, allowing translation, rotation, scaling and reflection, or affine, which also allows shearing. In the context of registration of medical images for stereotactic neurosurgery, a rigid transformation without reflection is suitable; scaling may not be necessary if the imaging method gives absolute distance values for the surface. Preoperative CT/MRI images and surface capture images are not expected to show shearing or local distortion; image distortion could make the resulting registration unsafe for use in surgery.

1.4 Thesis aims and summary

The aim of this project is to use surface capture images to accurately locate targets points within the head, based on preoperative CT or MRI data, during surgery. In order to do this, registration must be performed between the surface capture data and the preoperative data; it is assumed that the physical relationship between the positions of the robot and surface imaging camera is known. This will allow a patient to be moved during surgery, giving better access to all parts of the head, and for the head to be quickly re-registered with the robot and preoperative images. Although it is usually for patients' heads to be draped during surgery, it is assumed that drapes can be removed at the time of imaging. It is also assumed that it will be possible to image the surface of the patient's head, i.e. that hair will be removed if necessary.

In chapter 2 background information from the relevant literature is given, including descriptions of registration methods and algorithms, stereotactic surgical robots and how they are registered to patients in surgery, and types of neurosurgery which can make use of stereotactic robots. The choice of registration algorithms used in this work is explained.

In chapter 3 two surface capture imaging devices are assessed as to their accuracy and suitability for taking 3D images that can be registered to preoperative CT/MRI data: the in-house Birmingham Surface Capture System and the Microsoft Kinect v1. The aim of this is to demonstrate that small, inexpensive devices can produce sufficiently accurate and dense point clouds to register the patient's location with the robot coordinate system and preoperative data. For this to work, the precise position of the imaging device with respect to the robot must be known. One possibility would be to mount the imaging device on the robot, close to the end effector. Images were taken of a phantom with both systems and the resulting point clouds were registered to the ground truth for the phantom. The median distance from the points to the ground truth was 0.269 mm for the Birmingham system, as compared to 1.80 mm for the Kinect; the Birmingham system also produced denser point clouds.

In chapter 4 the accuracy of the Iterative Closest Point (ICP) registration algorithm for registering representative point clouds extracted from MRI data is examined, in terms of root mean square (RMS) distance between surface point clouds. A region of interest (ROI) is defined from the surface point clouds. The effects of reducing point cloud density are examined, with the finding that up to 60% of points in the point cloud can be removed without significant loss of accuracy. The ROI point clouds are divided into octants and the effects of partial registration using one or more octants are examined. The effects of registration using a single octant are examined and compared with the effects of using multiple octants, either simultaneously, or by adding octants to the registration process sequentially. The results were to some extent dependent on which octants were chosen, but it was found that for sequential registration, for six of the eight possible initial octants, there was no significant improvement in using more than two octants, giving a mean RMS error of 0.813±0.026 mm. For the simultaneous version, a mean RMS error of 0.812±0.025 mm was found where three octants were used.

ICP is compared with the Coherent Point Drift (CPD) algorithm in chapter 5. CPD is expected to be more robust to noise and less affected by initial global alignment of the point clouds. The effects of initial transformation of the point cloud, adding noise and smoothed noise, and prealigning the point clouds using Principal Component Analysis (PCA) are examined. CPD is tested with and without the option of prenormalising the data before registration and denormalising it afterwards. ICP was found to have the best registration accuracy, which was unaffected by initial rotations of up to

$\frac{\pi}{5}$ radians and added noise levels of up to 10% of the standard deviation of the point cloud. An RMS distance of 0.889±0.049 mm was achieved across all transformations and noise levels. CPD was more affected by initial transformation and noise levels, but accuracy was improved by prealignment, from an overall mean of 0.999±0.166 mm to 0.912±0.057.

In chapter 6, another probabilistic algorithm, the three dimensional normal distribution transform (3D-NDT) algorithm is examined. The accuracy of 3D-NDT in registering ROI point clouds, with and without added noise, is compared with the accuracy of ICP and CPD. As expected, 3D-NDT is not affected by initial transformations of up to $\frac{\pi}{5}$ radians, achieving a mean RMS distance of 0.882±0.052 mm, which is comparable to ICP. Where noisy point clouds were used, 3D-NDT RMS distance increased with noise level from 0.883±0.052 mm at 1% noise, to 1.04±0.10 mm at 10% noise, suggesting that 3D-NDT does not deal with noise as effectively as ICP.

Since target coordinates will be located inside the head, in chapter 7 the relationship between errors at the surface, as measured in the previous chapters, and errors at points within the head, is investigated. Full volume point clouds extracted from MRI data are used. Surface registration is performed with ICP and the resulting errors at points within the head are calculated. The effect on internal registration accuracy of initial rotation about each of the three main axes is explored and it is found that the poorest accuracy is obtained when initial rotation is about the (vertical) z-axis. Prealignment with PCA is found to reduce internal errors to below 0.5 mm.

Conclusions are drawn, limitations are discussed, and suggestions for further work are made in chapter 8.

1.5 Thesis Contributions

In this work progress is made towards the aim of performing image based registration for a neurosurgical robot. Surface capture imaging with the Birmingham surface capture system suggests that an inexpensive 3D surface capture device could be suitable for the purpose.

Three registration algorithms, ICP, CPD and 3D-NDT, are selected and evaluated using representative surface point clouds extracted from MRI data. The effects of different starting positions and prealignment using principal component analysis are also tested. ICP is found to be the most robust of the three algorithms to noise and starting conditions.

Partial registration using ICP is also examined. ICP is found to be unaffected by reduction of point cloud density above a threshold of 40% of initial cloud density, using the same representative point clouds. The effect on ICP registration accuracy of dividing the point clouds into octants is also explored, with the finding that two or three octants can be sufficient to obtain optimum registration accuracy.

Full volume MRI point clouds are used to demonstrate that the above results of surface registration using ICP would lead to submillimetre accuracy within brain. Initial rotation about the vertical axis through the head leads to poorer final alignment, but this can be mitigated by performing a prealignment step using principal component analysis.

Chapter 2

Background and Literature Review

In this chapter, relevant background information is given, including registration methods and algorithms (section 2.1), examples of stereotactic robots and how they are registered to the patient and preoperative data (section 2.2), and examples of stereotactic neurosurgical procedures (section 2.3).

2.1 Registration methods and algorithms

In order to perform stereotactic neurosurgery, accurate registration (spatial alignment) is required between the coordinates systems of the patient, the preoperative images, and (if used) the stereotactic robot. Image registration is performed by determining how the images correspond and using a registration algorithm to identify the transformation that will give the best possible alignment of the system. Often the correspondence between images is determined using suitable landmarks which can be seen in both the modalities which are to be registered. Finding the best registration position may require using mathematical optimisation, often iterative, to find the values for the transformation parameters (such as x, y, and z translation distances, angles of rotation) which give the minimum difference between the images. Examples include Newton's method, using the Hessian (containing the second derivatives of the parameters), gradient descent methods and interpolation. Registration methods used by specific robots are discussed in section 2.2.

Registration methods can be divided into area-based, which ’deal with the images without attempting to detect salient objects’, instead using either subimages defined by windows of chosen size, or the entire image, and feature-based methods, using landmarks [12].

2.1.1 Area-based methods

Area-based methods are voxel property-based: they make use of image of subimage greyscale values rather than extracting features from the image.

2.1.1.1 Cross-correlation

Correlation-like methods are often applied to registering 2D images, but can be extended to 3D registration. A ’window’ size and shape is chosen and each possible window or subimage of this size and shape in the source image is compared to each possible window in the reference image. The similarity between each pair of windows is computed using normalised cross-correlation and the maximum similarity gives the registered position. This method can work exactly for translation only, but can also be applied where slight rotation and scaling are present. If a large number of pairs of images must be compared, the method can be computationally expensive. [12]

As a similarity measurement, cross-correlation may be used as part of a variety of registration algorithms. Normalised cross-correlation has been reported as one of the best motion estimators in real-time ultrasound based techniques [13]. Cross-correlation is most effective as a measure of similarity where there is a lot of structure within the windows used and less effective where they are more uniform [14]. Interpolation can be used to register at a sub-pixel level [15]. Malinsky et al. [16] describe the use of normalised cross-correlation in the registration of 3D MRI data, in conjunction with a template-matching algorithm.

2.1.1.2 Phase correlation

Fourier or phase correlation methods transform the images into Fourier space, calculate the cross-power spectrum and apply the inverse Fourier transform to obtain the normalised cross-correlation between the images, the peak of which gives the registered position. This is less computationally expensive than the cross-correlation method and may be preferred for inter-modality registration or where frequency dependent noise is present. Interpolation can again be used to register at a sub-pixel level [17].

Phase correlation can be used in 3D medical image registration, for example Foley et al. [18] describe the use of a 3D phase correlation algorithm to register and compare CT images of patient anatomy over the course of radiotherapy treatment for prostate cancer. Bican and Flusser [19] describe using a 3D cylindrical phase correlation method to perform intra-modal registration in brain imaging, using both MRI data and pre- and post-treatment single-photon emission computerized tomography (SPECT). Hacihaliloglu et al. [20] describe using a phase correlation method to inter-modally register partial ultrasound (US) volumes to full CT volumes in US-guided orthopaedic surgery.

2.1.1.3 Mutual information

Mutual information registration methods make use of the joint histogram or feature space between the two images. This is constructed from the greyscale values of the two overlaid images: for each point in the source image there is a corresponding point in the reference image based on their current alignment and the two points each have a greyscale value (where the images do not overlap the absent value can be treated as blank space). The histogram is a plot with the greyscale values of the two images along the axes; for every pair of greyscale values from the images, the corresponding point or bin is increased by one. The feature space thus depends on the alignment between the images: when the alignment is good (a state of low entropy/high mutual information), clusters are formed and when it is poor, the clusters are dispersed. Registration can therefore be performed by minimising the joint entropy of the images/maximising the mutual information. The method has been used for both intra- and inter-modal registration in and between modalities including MRI, CT, SPECT, PET and US [21].

Registration techniques can in some cases be combined. For example, Andronache et al. [22] combine cross-correlation and mutual information in a hierarchical method by using joint intensity histograms on lower-level images and switching to a cross-correlational similarity measure at higher levels, testing their algorithm on CT-MRI registration. Loeckx et al. [23] describe the extension of the method of maximisation of mutual information for use in non-rigid registration, using conditional mutual information.

2.1.2 Feature-based registration methods

Feature-based registration methods make use of features or landmarks within the image and may therefore be less computationally expensive than using the full image. The features can be intrinsic to the image, such as anatomical features, or extrinsic, such as fiducial markers which are added to a scene to provide reference points. Images may need to be segmented to extract salient points.

2.1.2.1 Point based methods

In point based methods both images are represented as a point cloud, or a set of coordinates that represent the image. These can be based on specific features or simply a set of points at which a surface has been measured. Where fiducial markers or anatomical features are used there may be a direct one to one correspondence between the two sets of points, but where they are simply spread across a surface, as with surface capture imaging, this will not be the case.

Iterative closest point A classic and widely used point based method is the Iterative Closest Point (ICP) algorithm, which is described in detail in Chapter 4, in which source points are paired to their nearest neighbour in the reference point cloud and the transformation needed to bring them into alignment is determined iteratively, using singular value decomposition (SVD) to estimate rotation. Lee et al. [24] describe using ICP to register facial data from patient CT images with surface images of the patient for a cranial augmented-reality system. ICP requires good initial global alignment of point clouds and can become trapped in local minima. Yang, Li, and Jia [25] propose a ’Globally Optimal ICP’ (Go-ICP) to negate this problem, using a ’branch-and-bound’ approach to search the space of possible solutions and ICP to provide locall optimisation. Alternatively, Münch, Combès, and Prima [26] add surface normals to the ICP algorithm to perform non-linear registration, avoiding local minima.

ICP and variants thereof are commonly used in a wide variety of robotic and medical imaging scenarios. Standard point-to-point ICP uses the root mean square (RMS) Euclidean distance between point pairs as a measure of point cloud alignment, whereas point-to-plane ICP makes use of surface normals and replaces the direct distance between a point pair with the shortest distance from a point to the tangent plane of its paired point [27]. The point-to-plane technique ′has come into widespread use as a more robust and accurate variant of standard ICP when presented with 2.5D range data′ (2.5D range data contains both depth and colour information) [28].

Segal, Haehnel, and Thrun [28] combine these approaches to produce Generalized-ICP (GICP), which they describe as ′plane-to-plane′. The algorithm attaches a probabilistic model to the minimisation step of ICP, by which it ′models the sensor noise and utilizes the local continuity of the surface sampled through the cloud′ [29]. In effect, a distance error function is produced which is bounded by the point-to-point method, which gives its maximum, and the point-to-plane method, which gives its minimum. Serafin and Grisetti [29] propose a Normal ICP (NICP) algorithm, which ′combines and extends the point-to-plane error metric proposed in GICP, while using a scene representation inspired by the Normal Distribution Transform (NDT)′ (see below and chapter 6 for further discussion of the NDT registration algorithm). Serafin and Grisetti [29] find that their algorithm gives ′better results and higher robustness to poor initial guesses′ in reconstructing a scene from range sensor images than GICP and NDT, but the methods have not been tested in a medical imaging context.

Shin et al. [30] propose a weighted version of ICP for registering a patient's facial surface with preoperative CT scans, in order to perform frameless, markerless intracerebral haematoma removal surgery. Weights are used to preferentially register with those areas of the face that deform the least. Zhang, Choi, and Park [31] propose a variant of ICP for partially overlapping surfaces using biunique correspondence, searching multiple closest points to identify which parts of the images overlap; they define a ′No-Correspondence Outlier′, which is not in an overlapping region and make use of a coarse-to-fine approach. This method is tested using range images. In some cases ICP is used to provide a coarse registration step before an alternative final method is used [32].

Probabilistic methods Probabilistic registration algorithms may also be applied to point clouds. For example, the Coherent Point Drift (CPD) algorithm (outlined in chapter 5), treats registration as a probability density estimation problem, in which the source point cloud is deemed to be composed of Gaussian mixture model centroids and iteratively fitted to the reference point cloud by maximising the likelihood. Examples of the use of CPD in medical imaging include non-rigid registration of blood vessels: this was performed using landmarks as an extension to CPD to improve speed and accuracy and validated using MRI data [33]. Non-rigid CPD was also used by Koch et al. [34] to model the deformable shape of the left atrium. Farnia et al. [35] compare CPD with ICP in registering intraoperative US with preoperative MRI images in a phantom study to assess brain deformation during neurosurgery, finding CPD to be more accurate and less affected by initial global alignment than ICP. In another extension to the CPD algorithm, Xia, Zhao, and Liu [36] proposed combining CPD with the scale invariant feature transform method (SIFT) for multimodal image registration by constructing phase congruency representations of the images to be registered.

The 3D Normal Distributions Transform algorithm (see chapter 6) also represents one point cloud as a probability distribution function and uses Newton's method of optimisation to find the best alignment of the point clouds. This method was developed for use in 3D scan registration [37, 38] and is not known to have been used in a medical imaging context.

2.1.3 Deformable models

Some of the algorithms discussed above allow, or have been modified to allow, non-rigid or deformable models of registration. As discussed in section 1.3.1, these require affine or elastic transformation models. Where there is some variation in the subject over time, such as when monitoring the progress of radiotherapy treatment for cancer, deformable models can be used to register together images taken at different time points. This requires the image to be segmented anatomically to ensure that the correct parts of the image correspond on deformation. The data structure is commonly represented as active contours (splines) or nets rather than points, and elastic modelling constraints are imposed on the data.

Deformable transformation methods can be categorised as parametric and non-parametric. In non-parametric methods, the ’transformation is described by an arbitrary displacement field regularized by some smoothing criteria’ [39], while ’parametric methods are based on some piecewise polynomial interpolation of a displacement field using a set of control points placed in the image domain’ [39]. B-splines, thin-plate splines and Bezier functions can all be used for interpolation. As the current problem requires a rigid transformation model, deformable registration models will not be further considered.

2.1.4 Deep Learning

More recently, researchers have begun applying machine or deep learning methods to image registration problems. These methods are predominantly so recent that they were not published when choosing registration algorithms for this project and are thus only briefly touched upon here.

Litjens et al. [40] describe two main strategies: ’(1) using deep-learning networks to estimate a similarity measure for two images to drive an iterative optimization strategy, and (2) to directly predict transformation parameters using deep regression networks.’ The first category includes the work of Cheng, Zhang, and Zheng [41] who use stacked auto-encoders to learn a similarity metric between CT and MRI images patches; Simonovsky et al. [42], who use convolutional neural networks on T1- and T2-weighted MRI brain scans of newborns; and Wu et al. [43] who use an unsupervised approach, combining independent subspace analysis and convolutional layers to extract features from brain MRI input patches [40]. These methods have shown improvements over the use of mutual information and cross-correlation similarity measures.

Into the second category falls the work of Yang, Kwitt, and Niethammer [44], who ’design a patch-based deep encoder-decoder network which learns the pixel/voxel-wise mapping between image appearance and registration parameters’, using large deformation diffeomorphic metric mapping registration and testing their approach on MRI data. Miao, Wang, and Liao [45] use a convoluted neural network regression approach to registering 2D DRRs and 3D CT data, directly estimating transformation parameters from image features. Their approach allows real-time registration ’with a significantly enlarged capture range when compared to intensity-based methods’ [45].

2.1.5 Choice of registration algorithms

In choosing suitable algorithms to test for the purpose of registering surface capture images with CT/MRI data, important considerations are the types of data to be registered, how a correspondence between data types can be established, and the most suitable transformation model for the purpose.

Surface capture data, in its raw form, consists of depth information, which can be used to represent the surface as a 3D surface point cloud, and (usually) RGB colour data for each point. The latter cannot be used for registration with CT/MRI data, as CT/MRI do not record colour. Similarly the internal information provided by CT/MRI data has no corresponding feature in the surface capture data and cannot be used in registering with it. Registration must be performed between the surface capture point cloud and the head surface as extracted from preoperative data. Use of Nirfast software [46] makes extraction of a surface point cloud from MRI data relatively simple and numerous algorithms exist which register two point clouds together, making the point cloud method of data representation a good choice. The RMS distance between points can be used as a distance measure for registration.

Little to no deformation is expected of the surface of the head, which closely follows the rigid skull. Therefore, a rigid transformation model, consisting of translation, rotation and, if needed, scaling is required.

The main requirements for a suitable algorithm, therefore, are a point-based method and a rigid transformation model. ICP, as a widely used and simple algorithm, is an obvious choice to test. CPD is also widely used for point cloud registration, allows rigid transformations and is reported to be robust to noise and outliers [47]. Both algorithms have been used in a variety of medical imaging tasks. 3D-NDT is not known to have been used for medical imaging tasks, but is reported to be efficient and robust to starting conditions [37]. These algorithms are therefore chosen for testing; they are discussed in detail in chapters 4, 5 and 6 respectively.

2.1.6 Landmarks

Currently, physical points of reference to be used in registration are commonly taken from either a stereotactic frame (a frame fixed to a patient's head, which provides reference points for registration) or fiducial markers, which are fixed to the patient and provide points of reference in each coordinate system. The frame or markers must be visible in both imaging modalities used. In either case the patient's head must be clamped or pinned in place using a head holder (Fig. 2.3c).

Whether a frame-based or frameless system is used, the robot must be accurately registered with the patient in theatre.

2.1.6.1 Frame-based system

In the frame-based system, the frame must be physically calibrated with a known position on the robot. One method is to use a calibration cage or localiser box attached to the robot end effector and placed about the patient's head (Fig. 2.1a). The sides of the cage are implanted with beads which are opaque to X-rays and two X-ray images are taken showing the beads and markers on the patient's frame, allowing the transformation matrix between the patient and robot to be determined [48]. Alternatively, the box can be used in CT or MRI preoperative imaging.

Since 2009, the neuromate® frame adaptor has been designed to interface with the O-arm (Meditronic), which is used to perform X-ray/CT in theatre, allowing registration of the robot and patient to be performed (Fig. 2.1b) [5].

2.1.6.2 Frameless system

In a frameless system, fiducial markers provide landmarks for registration. These markers must be visible in preoperative imaging and for in-theatre registration with

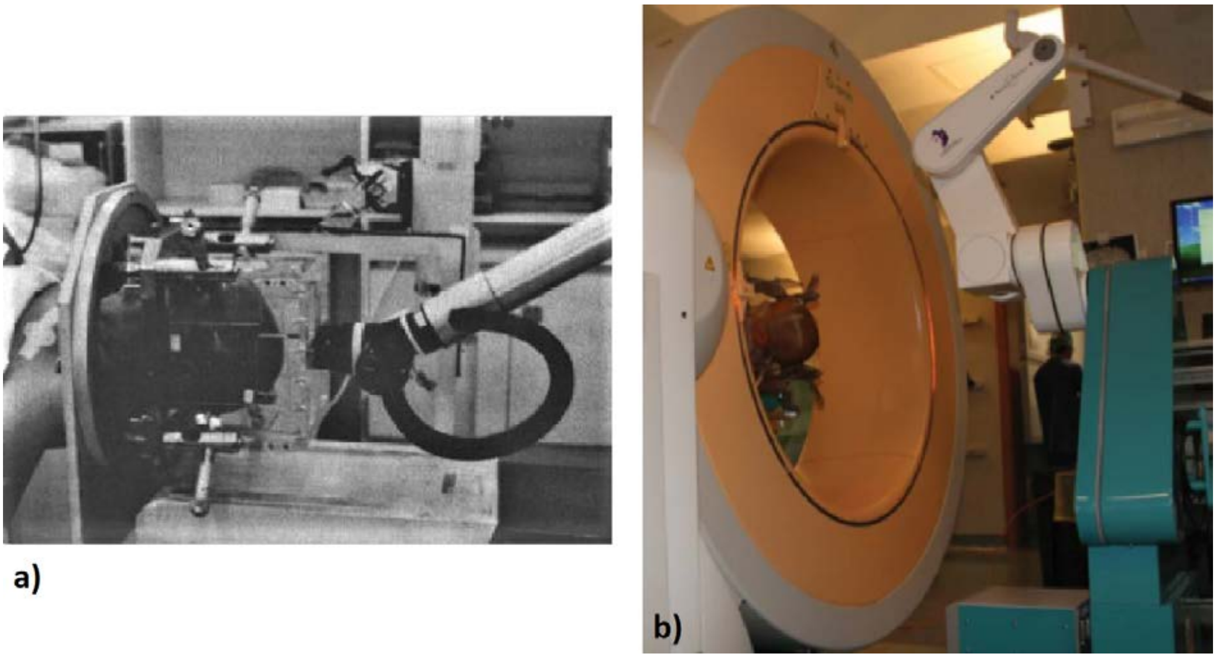

FIGURE 2.1: Calibration of robot with patient: a) calibration cage held by robot, taken from [48], originally from [49]; b) neuromate® robot interfacing with O-arm (Meditronic), from Cardinale et al. [5]: patient's head is held in a stereotactic frame, which is attached to the robot with a frame adaptor. CT imaging allows the patient, frame and robot to be registered in theatre.

the robot. Fiducial markers are generally pinned or screwed to the skull to prevent movement.

The frameless system for neuromate® requires a fiducial base plate to be screwed into the skull and anchored with three biocompatible pins. A CT/MRI compatible image localiser is attached to the base plate for pre-imaging with CT and MRI visible markers on the end of each spoke (Fig. 2.2a). During surgery this is replaced with an ultrasound microphone array with a similar shape to the localiser. An array of four ultrasound emitters is attached to the robot arm, allowing registration of the robot and patient for surgery (Fig. 2.2b) [6].

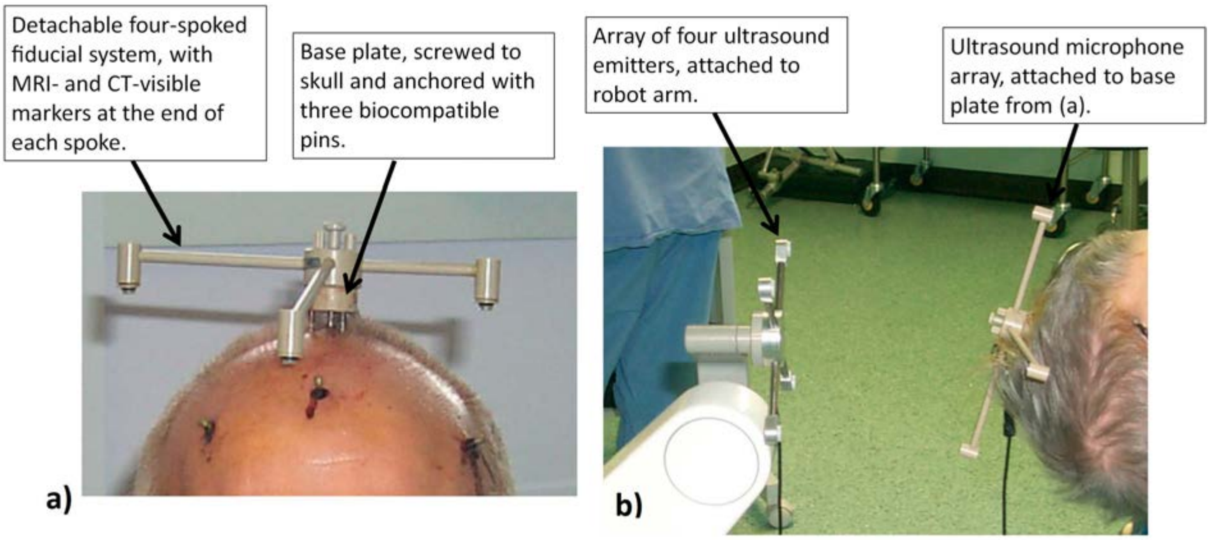

FIGURE 2.2: Registration of robot with patient: a) preoperative images are taken with the CT and MI compatible image localiser in place; b) ultrasound registration of robot to patient in theatre. The three pins at the front of the head are not believed to be part of the registration system. Images from Varma and Eldridge [6]

.

Frameless methods are generally quicker but less accurate than frame-based techniques; they are more invasive due to the need to screw markers into the skull, but may provide less obstruction to the robot than a frame [50]. Where fiducial markers are used, the pins used to attach the patient's head to a head-holder may cause some displacement of the markers, or 'skin shift', reducing accuracy [51].

2.1.6.3 Frameless *v.* frame-based systems

Frame-based methods have been shown to be more accurate than the frameless system [7], but provide less flexibility. Li et al. [7] achieved a root mean square (RMS) error of 1.95±0.44 mm for the frameless system, as compared with 0.86±0.32 mm in the frame-based configuration; Varma and Eldridge [6] showed an application accuracy of 1.29 mm using frameless ultrasound registration. Both phantom studies used the neuromate®. Bjartmarz and Rehncrona [52] compared non-robotic frame-based and frameless stereotaxy for DBS electrode implantation in patients with essential tremor, finding that the frameless technique resulted in larger medial-lateral (1.9±1.3 mm as opposed to 0.5±0.5 mm for frame-based) and anterior-posterior (0.9±0.8 mm *v.* 0.4±0.4 mm) errors as compared to the frame-based technique, but similar errors in the superior-inferior direction. The frameless electrode implantation was performed using Nexframe (a frameless stereotactic technique) and Stealth Treon plus (a neuronavigation system); five fiducial markers were screwed into the skull and registered using CT imaging. The frame-based technique used the Leksell G-frame, which was fixed to the skull bone before pre-operative MRI imaging.

Bot et al. [53] also compared the accuracy of DBS lead implantation using Nexframe with that using the Leksell frame, finding equivalent overall 3D accuracy. The Leksell frame performed better in the anterior-posterior plane (1.2±1.0 mm as opposed to 1.7±1.2 mm for Nexframe, $p = 0.04$), while Nexframe had higher accuracy in the dorsal-ventral plane (1.0±0.9 mm *v.* 1.3±0.9 mm for Leksell, $p = 0.04$). Performances were similar in the medial-lateral plane (1.4±1.3 mm for Nexframe, 1.4±1.0 mm for Leksell).

In general, frameless systems are less accurate than frame-based, but may offer more flexibility in allowing easier access to the patient's head. Whether frameless systems are faster is uncertain. Smith et al. [54] report that frame-based stereotactic brain biopsies 'required a mean of 114±3 min of operating room time, while frameless biopsies required 185±6 min' and that lengths of hospital stay were 1.8±0.2 and 3.2±0.6 days respectively. However, Dammers et al. [55] showed operating times of 149±32 minutes for frame-based and 127±33 minutes for frameless brain biopsies and hospital stays of 4.9±4.5 days and 3.9±3.4 days respectively. Operating times may in part depend on the surgeons' preference and level of experience with the system in question.

Frame-based systems are likely to be required where submillimetre accuracy is needed, such as in the treatment of Parkinson's disease, whereas frameless techniques may be more suitable for tumour biopsy or therapy, where an accuracy of 2-3 mm is sufficient [56].

2.1.6.4 Alternative methods

Woerdeman et al. [57] compared less invasive registration methods for frameless, image-guided neurosurgery: adhesive markers, surface matching and anatomical landmarks, obtaining mean application errors of 2.49±1.07 mm, 5.03±2.30 mm and 4.97±2.29 mm, respectively. For each patient, between six and eight adhesive fiducial markers were applied, 'avoiding regions likely to undergo gross skin displacement or those particularly susceptible to registration difficulties', approximately 300 surface points were obtained 'by smoothly stroking the entire scalp surface with the passive probe' and between five and eight anatomical landmarks were chosen. The authors concluded that adhesive markers provide the best accuracy of the three non-invasive techniques, but that where marker accuracy is compromised by using the results of an earlier imaging study, the other techniques form equally accurate alternatives.

Ortler et al. [58] compared the accuracy of historic framed-based implantation of depth electrodes with that of implantation performed using the Vogele-Bale-Hohner (VBH) system, 'a maxillary fixation system that permits frameless stereotactic instrument guidance with minimal invasiveness'. The VBH system includes a mouthpiece and registration frame: pre-operative CT and MRI imaging was performed with these in place. Lateral target localization error was 2.433±0.977 mm for the VBH system, as compared with 1.803±0.392 mm for the frame-based method.

A purely image-based technique for collecting data for registration could potentially be quick, accurate, more flexible and less invasive than the use of a frame or markers. In order to get a sufficiently close and unobstructed view of the patient's head an imaging device attached to the robot arm may be suitable, as a fixed device is more likely to be obstructed by theatre staff or to get in their way. To get the best registration results a 3D imaging method is likely to be necessary. This would produce a set of coordinates at which the surface was measured, known as a point cloud, which could be used as a set of landmarks. A similar surface point cloud could be extracted from CT or MRI data and registration performed between the two point clouds.

2.2 Stereotactic robots

Stereotactic robots are particularly suitable for use in neurosurgery, as the rigidity of the skull prevents significant movement of the brain and gives a reliable frame of reference unavailable in the rest of the body. The robots described below are used in stereotactic radiotherapy or neurosurgery. All are or include a robot which can move about the patient to act at the required coordinates with the required trajectory and all must be registered to the patient and preoperative images. Each system has its own proprietary software for registration and planning; registration methods and algorithms as available in the literature are described below. More detailed explanations of the surgical procedures described are given in section 2.3.

2.2.1 neuromate®

This project is primarily concerned with the neuromate® (Renishaw plc), which is a stereotactic robot (Fig. 2.3). The neuromate® is a stereotactic robot, development of which began in 1987: it finally became commercially available in 1999, and was the first stereotactic robot to be used for procedures other than biopsies [61]. By 2001, neuromate® had assisted in 1600 neurosurgeries [48] and as of 2014 more than 30 robots are installed worldwide [62]. These procedures included electrode implantation procedures for Deep Brain Stimulation (DBS), and Stereotactic Electroencephalography (SEEG) [5], as well as stereotactic applications in neuro-endoscopy and biopsy [3]. Neuromate® has recently been used in a frame-based technique for placement of intracerebral electrodes for investigation of focal epilepsy at Frenchay Hospital in Bristol, allowing a less invasive procedure than conventional electrocorticography involving a craniotomy. The Leksell stereotactic frame was used, which works on a ’centre-of-arc’

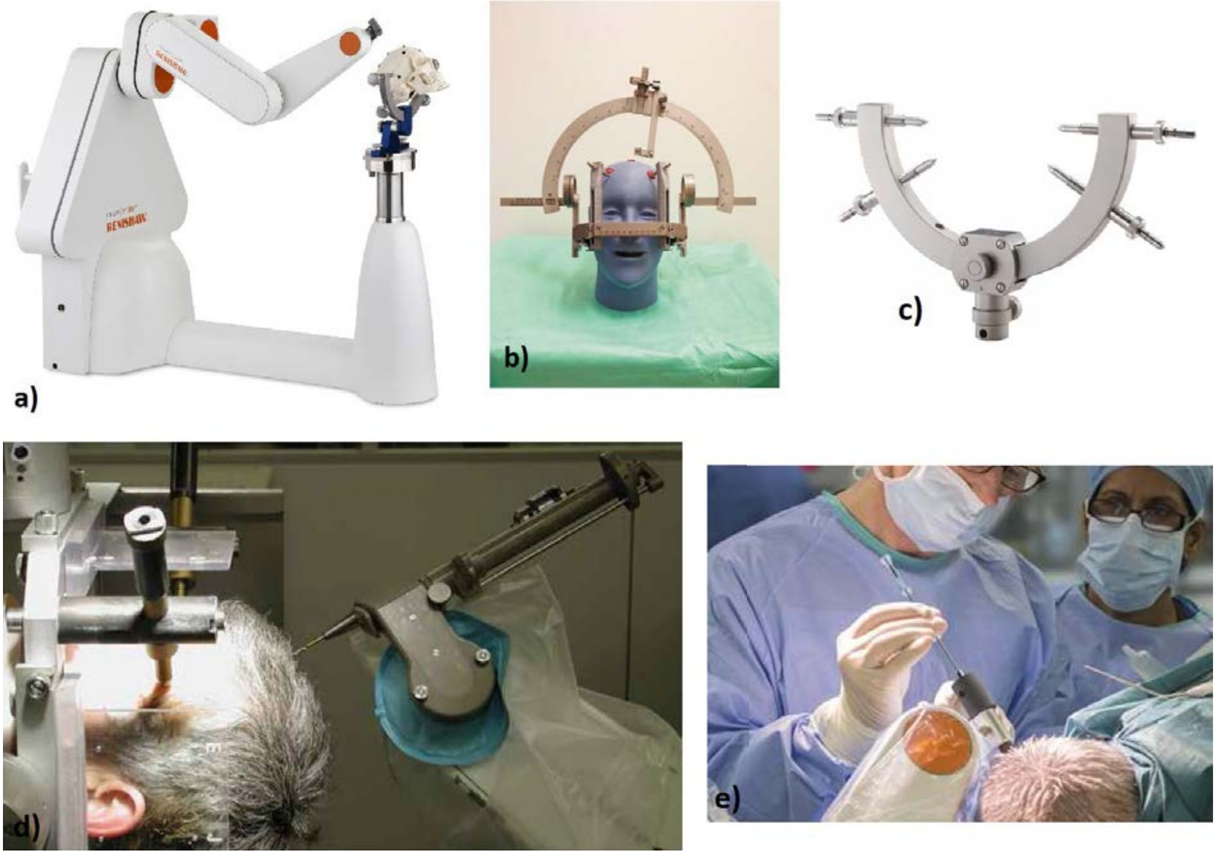

FIGURE 2.3: (a) neuromate® with skull phantom in head holder; (b) Leksell stereotactic frame [59]; (c) head holder (Mizuho Medical Innovation) (f) patient with neuromate® robot with drill attachment and frame, robot arm is covered with a sterile drape; (g) Insertion of a biopsy needle through a tool guide mounted on the neuromate® arm. Except where stated, images are from Renishaw plc [60].

principle: from any position on the arc the effector (which is perpendicular to the arc) points directly to the target (Fig. 2.3b) [63].

The neuromate® has also recently been used in direct electrical stimulation (ES) of the human insular cortex during surgical procedures for epilepsy [64]. Varma and Eldridge [6], using the robot in a frameless mode, showed an application accuracy of 1.29 mm in targeting fiducial markers screwed into a phantom (i.e. at the surface). Li et al. [7] saw a root mean square (RMS) error of 0.86±0.32 mm in a frame-based configuration and 1.95±0.44 mm in a frame-based system; CT images of the phantom were used for registration, 10 measurement points were selected representing 'a volumetric cube of 100 mm', and target points for the frameless system were provided by three semi-invasive screw markers. The robot can achieve any given position in a variety of ways, due to its six degrees of freedom (five rotational and one linear) [65], meaning that assessment of its accuracy must take into account the accuracy of each movement that it may make [7].

Registration for neuromate® is performed using the Neuroinspire software package (Renishaw plc), which performs rigid body registration using normalised mutual information as a cost function. Geevarghese et al. [66] found that registration between preoperative CT and MRI images for a single subject undergoing deep brain stimulation (DBS) took 5-10 minutes.

2.2.2 ROSA

The ROSA (Robotic Stereotactic Assistance) system (Medtech Surgical, Inc) is a stereotactic neurosurgical robot, similar to the neuromate® in that it consists of a robotic arm with six degrees of freedom, coupled to a planning station. ROSA also has haptic capabilities. ROSA uses a laser measuring system to perform patient registration without the use of landmarks. Gonzalez-Martinez et al. [67] report on using ROSA to place a laser ablation catheter, using intraoperative MRI to check catheter position. Registration was achieved using facial features as surface landmarks.

Lefranc et al. [68] describe using ROSA to perform 100 stereotactic brain biopsies. Preoperative MRI and CT scans were registered together by Rosana (Medtech) software, using a rigid, linear algorithm. The majority of cases used frameless robotic surface registration; others used bone or scalp fiducial markers. The laser measuring system was used for frameless registration. 'Around 5000 to 8000 points of the face, dorsum, edges of the nose, forehead, and temples are automatically registered. Accuracy of the registration was confirmed by the surgeon on several landmarks such as the root of the nose, internal and external canthus, temples, midline, and free landmarks chosen by the surgeon.' Registration with fiducial markers was performed in theatre using 3D flat panel CT imaging with the robot linked to the CT scanner. This work followed a phantom study, which reported mean target accuracies of 1.59 mm for 3T MRI guided frameless surgery, 0.3 mm for flat panel CT-guided frameless surgery, and 0.3 mm for CT-guided frame-based surgery [69].

Serletis et al. [70] report on the use of the ROSA system in 78 stereoelectroencephalographic electrode implantation procedures in patients with epilepsy, with comparable success rates to manual implantation using a Leksell stereotactic frame. ROSA has also been used in Deep Brain Stimulation (DBS) by Vadera et al. [71]. In this case registration was performed using five bone fiducial markers, which were CT imaged intraoperatively and registered to the robot by 'contacting a pointer probe mounted to the robotic arm to each bone fiduciary'; the robot planning station was used to fuse the intraoperative CT data with preoperative MRI images. The authors report that the use of bone fiducial markers is required for DBS with ROSA, in order to obtain improved accuracy over the laser-guided registration method. Brandmeir, Acharya, and Sather [72] report on the use of ROSA to treat a hypothalamic hamartoma (benign tumor) with laser ablation, also performing registration using five fiducial markers.

2.2.3 CyberKnife

The CyberKnife (Accuray) is an image-guided frameless robotic radiosurgery system comprising a robot arm mounted with a linear particle accelerator (LINAC) used to direct radiation to the body from any direction. It is used for treatment of cancer and other radiosurgical procedures and is an open system, allowing 'unobstructed treatment of the whole body' [73]. Kilby et al. [74] give the targeting accuracy of the 2010 CyberKnife VSI system as $\leq$0.95 mm (static) and $\leq$1.5 mm (with respiratory motion). Accurate registration of the patient with the system and preoperative images is required. Prior to treatment, a 3D patient model is generated from a volumetric CT scan of the patient. At the time of treatment, beam alignment with the patient is performed by registering orthogonal 3D digitally reconstructed radiographs (DRRs) from the 3D patient model with X-ray projection images taken by the treatment room imaging system. The transformations obtained by the 2D registrations are combined to determine the 3D transformation using geometric back projection. As the relations between the X-ray imaging system, CyberKnife and patient couch are known, this allows registration to be performed. [74, 75]

The landmarks and precise system used for registration depend on the surgical target. '6D skull tracking' is used for targets in the brain, head and and neck, using high contrast bone information to perform registration as described above. Optimized pattern intensity and the sum of the squared difference between images are used as similarity measures; multiresolution matching, steepest descent minimization, and one-dimensional search are used as search methods in the registration process [76].

Targets in the spine or at a fixed position relative to it are registered and tracked using Xsight® Spine Tracking. In this case image processing filters are applied to enhance skeletal structures in DRRs and X-ray images, and the DRRs can be restricted to the region surrounding the spine. Registration is performed in the relevant and neighbouring vertebrae only [75].

Xsight Lung Tracking can be used to track in real-time lung tumours which move during treatment due to the patient's breathing. Initial global registration is performed as before and the tumour is tracked by matching the DRR tumour region image intensity pattern to the most similar region in the X-ray image, with a matching window defined by the tumour silhouette in each projection [74].

The CyberKnife system can also make use of radiopaque fiducial markers such as cylindrical gold seeds to track soft tissue targets which are not fixed relative to the skull or spine. These are implanted in the region of interest at least a week prior to the treatment planning CT scan, and are visible in the DRR images and treatment room X-rays, acting as landmarks in the registration process [74]. Mu, Fu, and Kuduvalli [77] describe the process used to accurately identify markers within X-ray/CT images and determine marker correspondence between images.

2.2.4 Novalis Tx

Novalis Tx (Brainlab) is a stereotactic image-guided radiosurgery system, with beam shaping technology and treatment planning; like the CyberKnife, a linear accelerator directs radiation to any part of the body. Rather than a multi-jointed robot arm, the LINAC is gantry mounted and is rotated about the patient; translation and vertical rotation are performed by the patient couch. The system has six degrees of freedom: three translational and three rotational. Frame-based and frameless registration are currently available. The ExacTrac image guidance system is based on stereoscopic X-ray imaging and infrared (IR) marker detection. IR body markers are attached to the patient and imaged by two ceiling-mounted IR cameras and used to perform initial patient localisation. Two X-ray images are then taken and registered to DRRs (similarly to the CyberKnife system) to perform the final localisation. Localisation is physically performed by automatic couch movement. The frame-based system uses either a standard stereotactic head frame or a relocatable mask, both of which used the same CT stereotactic localiser box. The frameless system requires a custom-fitted thermoplastic mask. Montgomery and Collins [78] report positional accuracy of <1 mm. [79, 80, 81]

2.3 Stereotactic Neurosurgical Procedures

Stereotactic neurosurgery permits access to areas of the brain which would otherwise be hard to reach. Some of the procedures which make use of stereotaxis, with or without robotic assistance, are described below, with particular reference to use of the neuromate® robot.

2.3.1 Deep Brain Stimulation

Deep Brain Stimulation (DBS) is used to treat a variety of conditions, including Essential Tremor (ET), Parkinson's Disease, Primary Dystonia, Epilepsy and many others

[82]. DBS involves surgically implanting electrodes within the brain in order to electrically stimulate particular areas, thereby altering brain activity. Electrical stimulation was initially used to map cortical function [83] before the development of stereotaxy; the development of stereotactic devices allowed deeper structures to be stimulated [84]. In treatments developed in the 1960s for conditions such as cerebral palsy [85] and Parkinson's [86], the response to electrical stimulation was used to determine the best location for the creation of lesions (used to reduce involuntary movements); stimulation later began to be used directly to treat pain, movement disorders and epilepsy via electrodes implanted on the surface of the cerebellar cortex [84]. DBS began to be used therapeutically with implantable electrodes and pulse generators in the 1990s [87, 88]. Stereotaxy is required in order to stimulate deep brain structures with sufficient accuracy, using a trajectory which will do minimal damage [84, 89, 90].

2.3.1.1 Methods of electrode implantation

Munyon et al. [91] performed electrode implantation in conjunction with open craniotomy in order to implant subdural grids, using frame-based stereotactic surgery.

González-Martínez et al. [92] reported on robotic stereoelectroencephalography (SEEG) implantation procedures, using the ROSA robotic device and a Leksell frame as a fixation system; patients were registered to preoperative MRI using semiautomatic laser-based facial recognition. They reported a median entry point error of 1.2 mm and a median target point error of 1.7 mm.

Holloway et al. [93] investigated the use of bone fiducial markers for DBS electrode implantation, finding no statistically significant difference in accuracy between frameless and frame-based methods.

2.3.1.2 Use of neuromate®

Langsdorff, Paquis, and Fontaine [94] evaluated the *in vivo* and *in vitro* application accuracy of the neuromate®, finding that the mean *in vitro* application accuracy was 0.44±0.23 mm, with a maximal localisation error of 1.0 mm, and the mean *in vivo* application accuracy was 0.86±0.32 mm (Δx = 0.37±0.34 mm, Δy = 0.32±0.24 mm, Δz = 0.58±0.31 mm), with a maximal error of 1.55 mm.

Cardinale et al. [5] analysed the accuracy of a series of 500 consecutive SEEG procedures using the neuromate®, in which a total of 6,496 electrodes were implanted. They obtained a median entry point localisation error of 1.43 mm (interquartile range, 0.91-2.21 mm) using a traditional two-step surgical workflow of stereotactic angiography and electrode implantation. Using an updated one-step electrode implantation workflow, the error was 0.78 mm (interquartile range, 0.49-1.08 mm). The neuromate® robot was used as a toolholder, in conjunction with a Talairach stereotactic frame, to help fix guiding screws to the skull.

The neuromate® has also been adapted for use in DBS in Japan, where the patient is placed in a supine (face upwards) position in order to minimise cerebrospinal fluid (CSF) leakage; in order to allow use of the neuromate®, the patient's head position was shifted by raising the head end of the operating table to an angle of 25° [89]. Kajita et al. [89] examined neuromate® localisation accuracy using a phantom and found an RMS error of 0.12±0.10 mm, measuring only mechanical accuracy. In 19 DBS procedures performed by the same team, using MRI preoperative imaging and a Leksell G frame, the RMS error was 1.36±0.83 mm.

2.3.2 Biopsy

Brain biopsy is typically performed stereotactically using pre-operative MRI imaging, with MRI-compatible stereotactic frames or fiducial markers, except when patients cannot undergo MRI, in which case CT is used [95]. Other functional modalities including positron emission tomography (PET) and magnetic resonance (MR) spectroscopy can be used to target the most biologically active parts of tumours for biopsy [95]. Open or excisional biopsies, including a craniotomy, are now avoided, as a combination of stereotactic biopsy and current imaging techniques make the added risk unnecessary: the surgeon can use imaging to decide whether resectioning will be possible [95]. In 1991, Lee et al. [96] reported that CT-guided stereotactic biopsy had a lower mortality and morbidity rate and a higher diagnostic accuracy than freehand.

Dammers et al. [55] compared frame-based and frameless image-guided stereotactic intracranial biopsies over a ten year period, finding that the 'diagnostic yield, complication rates, and biopsy-related mortality did not differ between a frameless biopsy technique and the established frame-based technique.' Hall [97] examined the use of stereotactic biopsy using CT or MRI guidance, finding it to be 'an extremely safe and effective procedure for evaluating intracranial lesions', reporting morbidity and mortality of only one patient each in a sample of 122, and diagnostic yield of 96%, as compared to the 91% reported in a series of 7,417 biopsies. However, Khatab, Spliet, and Woerdeman [98] suggest that reported high diagnostic yield in studies of stereotactic biopsies can disguise lower diagnostic accuracy and that the lack of a standard definition of 'diagnostic yield' makes it difficult to compare between studies. This makes it hard to accurately assess the effectiveness of stereotactic biopsy. In the 235 procedures in their study, 21.7% were inconclusive and 5.5% were non-diagnostic, with an overall morbidity rate of 8.5%, including a mortality rate of 0.9%. The procedures were performed over an eight-year period at University Medical Center Utrecht.

Lefranc et al. [68] report on the use of the Meditech ROSA device in 100 frameless robotic biopsies, finding it to be a "safe and effective way of establishing a histological diagnosis". Similarly, Haegelen et al. [3] reported on 15 neuromate-guided brain stem lesion biopsies, in a preliminary study which concluded that neuromate® 'is an efficient and safe instrument for biopsies of brain stem lesions'.

2.3.3 Neuroendoscopy

Neuroendoscopy allows surgeons to access deep-seated parts of the brain under direct visual supervision, while doing minimal damage; it can be used for both inspection and surgery [99][100]. Stereotactic guidance is not necessary on all cases, but allows small or deep targets that would otherwise be inaccessible to neuroendoscopy to be reached under direct visual control [4].

Frameless stereotactic guidance can be used, enabling 'free-hand movement of the endoscope with real-time control of the endoscope tip position and approach trajectory', and keeping the surgical field more free than frame-based methods [101]. Schroeder et al. [101] find that for 'selected cystic lesions, frameless neuronavigation is mandatory to be both successful and truly minimally invasive.'

2.4 Conclusion

In this chapter, a range of registration methods and algorithms have been considered and point-based registration with a rigid transformation model has been chosen as the most suitable type for use in this project. Three algorithms, ICP, CPD and 3D-NDT, have been chosen for testing in later chapters according to these crtiteria. They will be tested using example point clouds in chapters 4, 5 and 6 respectively.

A range of stereotactic robots and neurosurgical procedures has been presented, with particular attention to the state-of-the-art registration methods for each robot, as far as they are known from the literature.

In the next chapter (3), two surface capture imaging devices are assessed for their accuracy and suitability for taking 3D images that can be registered to preoperative CT/MRI data: the in-house Birmingham Surface Capture System and the Microsoft Kinect v1.

Chapter 3

Surface Geometry Acquisition

In order to register the patient's head during surgery with preoperative images and the neurosurgical robot, the head's position must be determined once it is fixed in place. This can be done by taking a three dimensional image of the surface, in which the location of the surface is measured at multiple points to give a 'point cloud' representation of the surface, i.e. a set of coordinates at which the surface has been measured. As the location of the camera with respect to the robot can be known, this can be used to register the surface to the robot coordinate system, as well as to the preoperative data.

3.1 Imaging Methods

Three dimensional (3D) surface capture imaging can be performed using a variety of techniques to give a set of coordinates (known as a point cloud) at which a surface has been measured. Information on colour and texture may also be recorded. Although the algorithms developed as part of this project were designed to be device-independent, and robot manufacturers are likely to produce their own in-house device, a device was needed for experimental purposes. An in-house system using structured light (the Birmingham Surface Capture System, [102]) was tested and compared with the Microsoft Kinect for Windows v1.

3.1.1 Birmingham Surface Capture System

The Birmingham Surface Capture System is a 3D imaging technique developed by researchers at the University of Birmingham, which estimates distance using structured light [102]. The device comprises a projector and a webcam, mounted so that the camera can image patterns projected onto a surface by the projector (Fig. 3.1). A series of fringe patterns are projected onto the subject and the deformation in the projected pattern is analysed to reconstruct the 3D data. The data is output in the form of a point cloud (a set of coordinates at which the surface has been measured); the system also allows this to be converted to a surface or volume mesh using Meshlab software [103]. Mirrors can be used to extend the field of view; on imaging a mouse-shaped phantom with this technique, 96% of points were found to lie within 0.4 mm of the surface mesh provided by the manufacturers (the accuracy of the surface mesh is not given) [102]. The system can give both colour and texture information about an object.

3.1.2 Microsoft Kinect for Windows

The Microsoft Kinect v1 was developed as an imaging and motion sensing device for use in Xbox video game consoles and is available as a version for Windows with a software development kit (SDK).

The device has RGB and audio sensing capacity and is capable of estimating depth using an infrared (IR) projector and camera. The IR projector projects a fixed speckled pattern (Fig. 3.2), and by measuring the deformation of this pattern a 3D map of the scene is calculated [104]. For each pixel in an image a depth in millimetres in the range

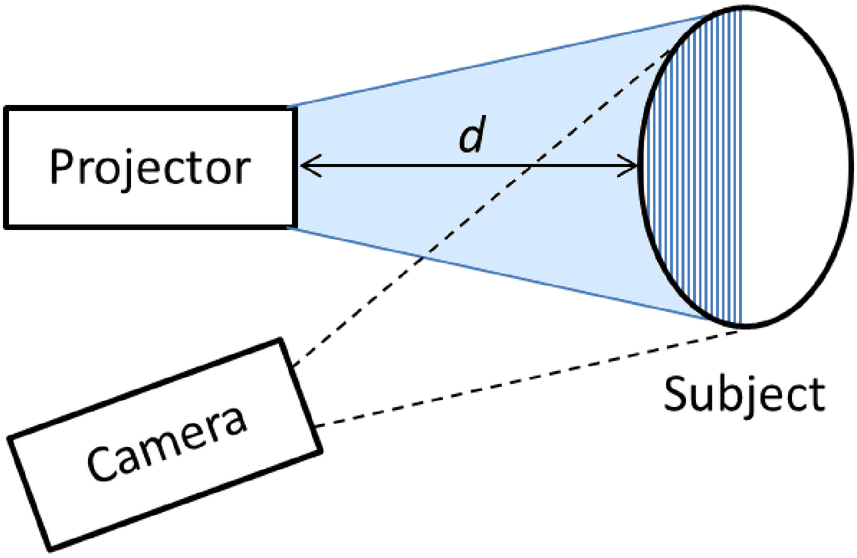

FIGURE 3.1: Schematic of Birmingham Surface Capture System: a series structured light patterns are projected on to the subject, the camera records the resulting images of the subject, and the distortion of the structured light is used to reconstruct a 3D image. The distance from the system to the subject is *d*. The device is as described in Basevi et al. [102], but no mirrors are used to extend the field of view to the reverse of the subject.

0.4-3.0 m is given to the nearest millimetre: if the Kinect records a depth outside this range, or is unable to calculate a depth, an answer of zero is given for that pixel. The depth given is the perpendicular distance to the point from a plane passing through the camera and perpendicular to its direction of gaze. This information, combined with the position of the pixel within the image, allows x, y, and z coordinates to be assigned to each pixel within the image; pixels with a depth value of zero must be omitted, since their depth is undefined. This point cloud is not raw data, since some processing is done to obtain depths from the IR pattern collected by the Kinect; the precise nature of the processing is not known, as it is proprietary information.

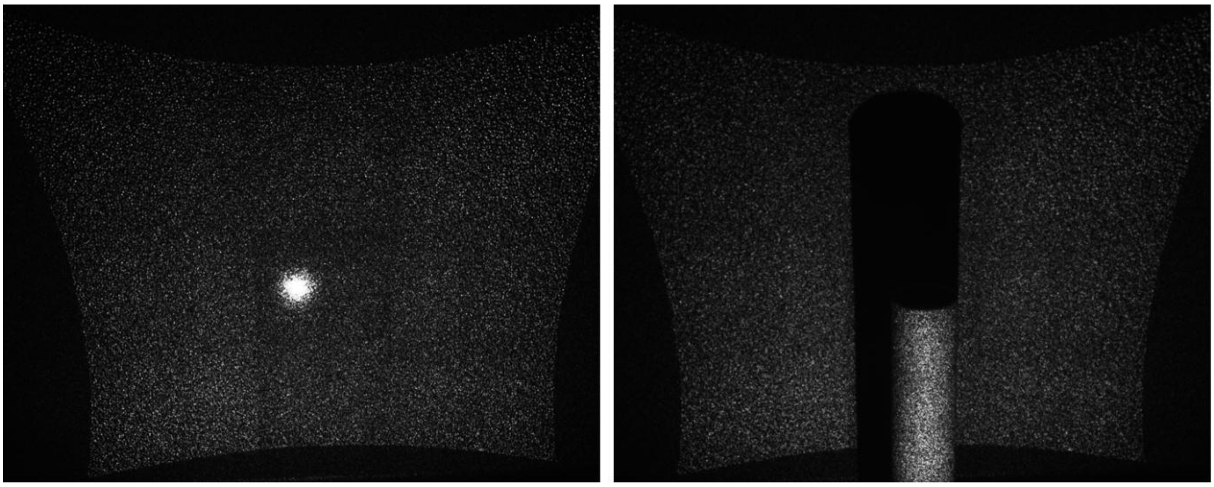

FIGURE 3.2: Kinect IR pattern (a) without and (b) with an obstacle in front of the whiteboard upon which it is projected, imaged with a CMOS camera with the IR filter removed.

The precision of the device is limited by the depth information to the nearest millimetre at best. The accuracy varies with distance from the device. Root mean square (RMS) errors for relative distances taken from 1-3 m away have been measured at up to 1.1 cm [105]. Software allows the tracking of human bodies and facial features. KinectFusion software is available, allowing the creation of a 3D model or mesh of a scene [106].

3.2 Device comparison

In order to compare the devices, images were taken of a mannequin and a phantom head. For the Birmingham system, the raw, unprocessed data was used; for the Kinect, coordinate data was used as described above.

3.2.1 Featured face

In order to make an initial comparison of the Birmingham surface capture system and Kinect v1, 3D images were taken of a mannequin head (Fig. 3.3) using both systems (Fig. 3.4). The images were taken from the front from distances between 40 cm and 90 cm, as 40 cm is the minimum distance possible for the Kinect v1; the Birmingham system can work at closer range. The Birmingham system records data only from the region of interest, whereas the Kinect records points from all surfaces within its field of view. Both systems included some outlying points which were manually cropped in Meshlab [103], but the Kinect included far more background objects which were not captured by the Birmingham system (Fig. 3.4).

Visually, the Birmingham system gives a closer approximation to the mannequin surface (Fig. 3.3), while the Kinect images are less smooth and more variable with distance, although no ground truth is available for numerical comparison. For this reason, a phantom was created with which to test the systems.

3.2.2 Phantom

A phantom (Fig. 3.5) was created using MRI data from a healthy adult subject. A mesh was extracted from the MRI data using Nirfast software [46] and 3D printed using

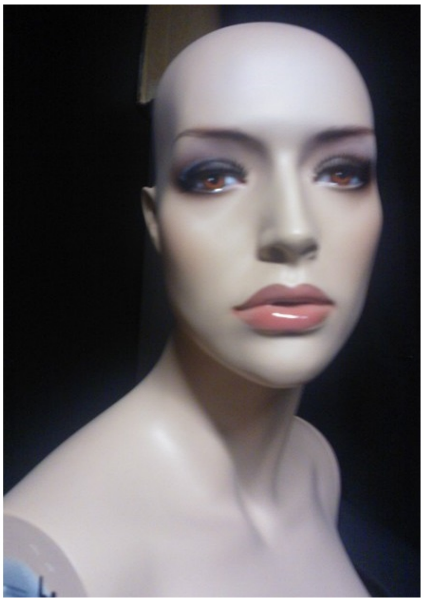

FIGURE 3.3: Mannequin used to test imaging systems.

glass filled nylon by Renishaw plc. The mesh used to create the phantom provides a ground truth which can be compared to 3D images of the phantom.

3.2.2.1 Comparing images to ground truth

Images were taken of the phantom head using both the Birmingham Surface Capture system and the Kinect v1. The resulting point clouds were registered to the mesh used to create the phantom, which acts as a 'ground truth' for the images, using the 'Align' filter in Meshlab, which makes use of the ICP algorithm [103][107] and requires a minimum of four matching features to be manually selected on each point cloud ('Point Based Glueing' [sic]). The 'Hausdorff Distance' sampling filter in Meshlab was used to calculate the distance to the nearest point in the registered surface image for each point in the original phantom mesh. (If the distances from each point in two sets (point clouds) to the nearest point in the other set are calculated, the Hausdorff distance

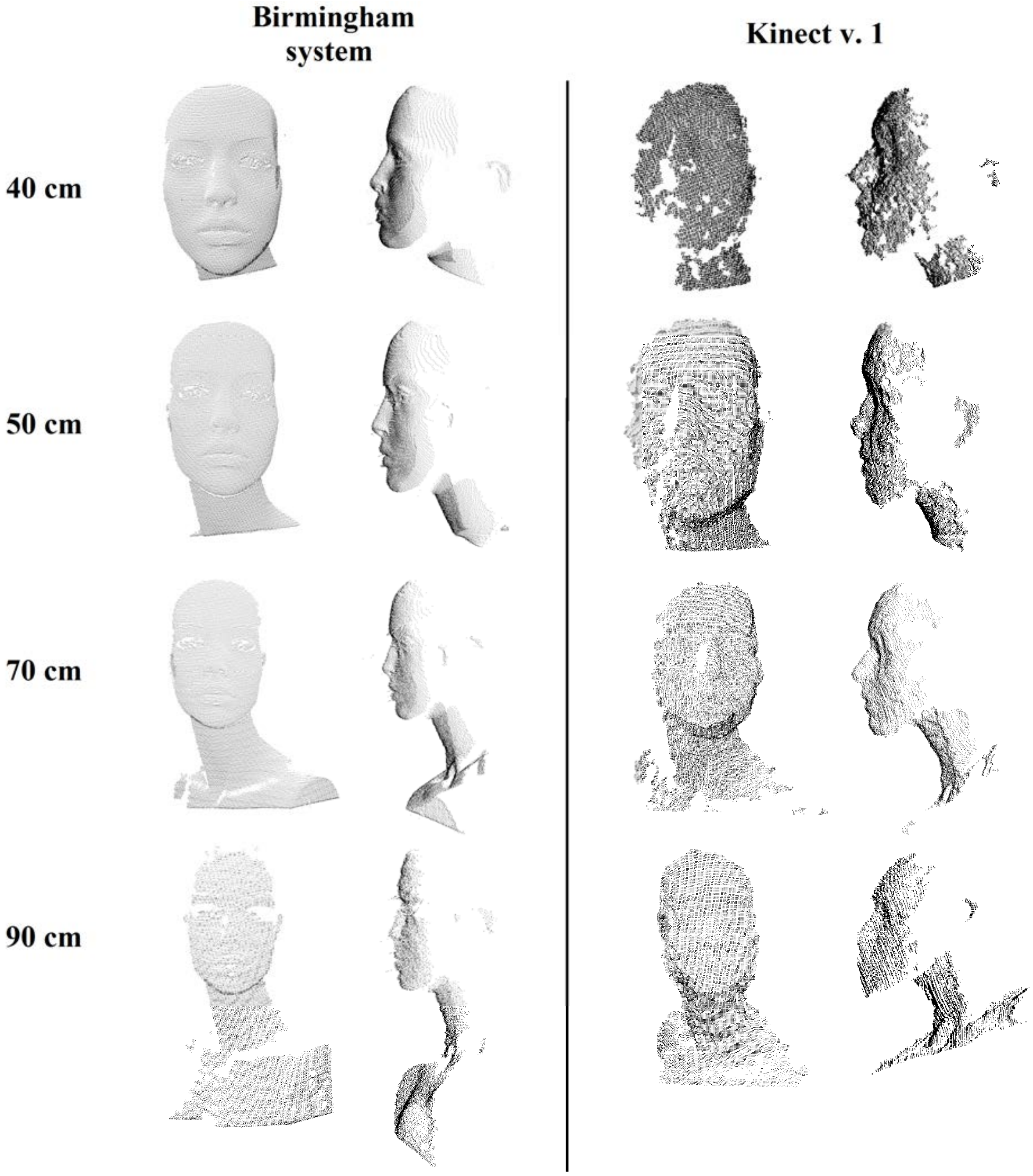

FIGURE 3.4: Images taken using (left) Birmingham system and (right) Kinect v1, from (top-bottom) 40, 50, 70, and 90 cm from the mannequin head. The images were taken from the front and the resulting point clouds show the full face and the profile. The Kinect point clouds had to be cropped to remove unwanted points.

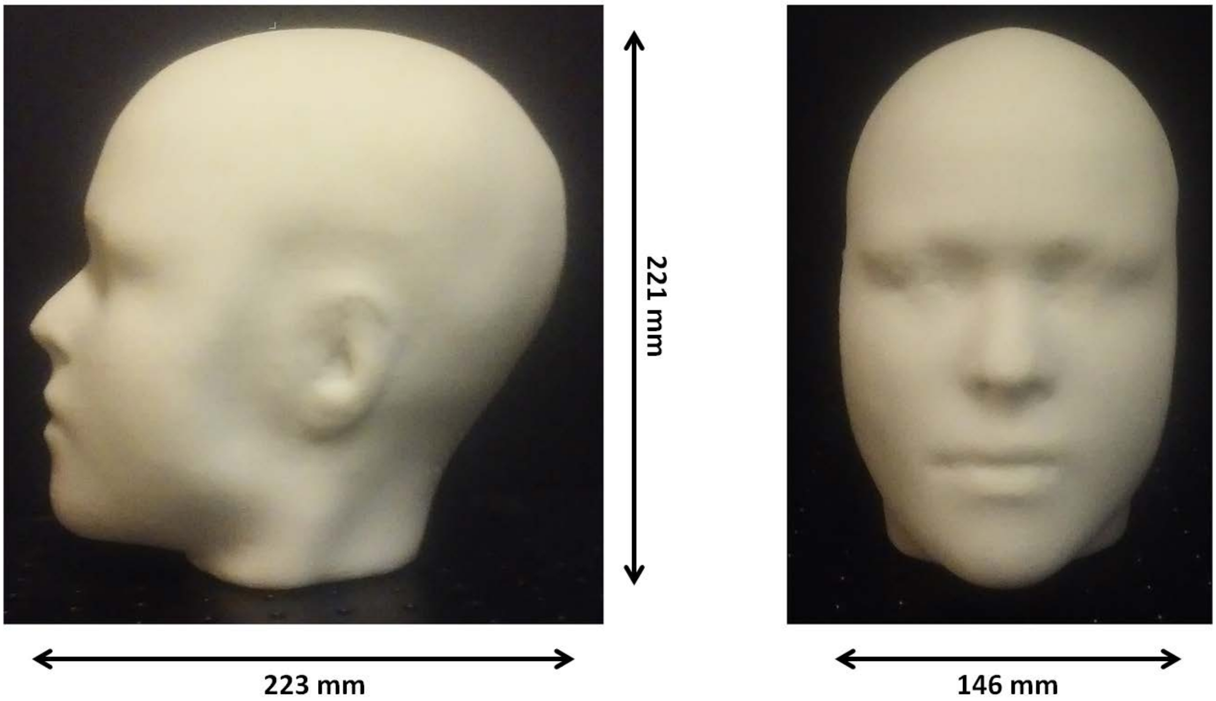

FIGURE 3.5: Phantom created from patient MRI data.

between the sets is the largest of these distances. The Meshlab filter can be used to give the distance of each point in one point cloud to its nearest neighbour in a second point cloud.) Each point was then given a colour based on the calculated distance.

Images were taken with the Birmingham Surface capture system from distances of 50-60 cm (Fig. 3.6), as the previous experiments had shown this to be the optimal distance. Distances greater than 1 mm are shown as dark blue to allow the smaller distances for the majority of points to be more easily visualised. Images were also taken with the Kinect v1 from 50-80 cm in front of the phantom (Fig. 3.7). In this case, the alignment is poorer and distances greater than 5 mm are shown in dark blue. The median distance from the ground truth of the points in the five Birmingham system images was 0.269 mm and the median for the six Kinect images was 1.80 mm (Fig. 3.8). The Birmingham system recorded a mean and standard deviation of $1.47 \times 10^5 \pm 2.07 \times 10^4$ points in the five clouds shown, while the Kinect recorded $6.16 \times 10^3 \pm 1.76 \times 10^3$ across for the four clouds shown here. This is after the clouds were cropped to contain the region of interest only, but reflects the higher point cloud density of the Birmingham system.

While imaging, all other objects were kept out of the field of view, except a box for the phantom to stand on, which could be easily manually cropped from the point cloud. This produced an interesting effect in the Kinect data: at the edges of the object, where no background was available, a large number of outlying points were present in front of or behind the main point cloud, suggesting the software struggles to cope with edges where no neighbouring data is available (Fig. 3.9).

Images were also taken of the top of the phantom head, using the Birmingham system. These proved difficult to register, due to their lack of surface features, which made it difficult to provide an initial global alignment. The similarity of the curves in different parts of the point cloud make it hard to find a unique alignment, especially where the point clouds are incomplete.

3.3 Registration of human subject surface capture image to MRI data

The subject from whose MRI data the phantom was originally created was also imaged using the Birmingham Surface Capture System and the resulting point clouds were registered to the phantom mesh. The Kinect v1 was not used, as previous results showed that Kinect images were a poorer match to the true surface (section 3.2.2.1). Images were taken of the subject's head and neck from a range of directions; as the subject's hair prevented images of the head itself being taken, registration was performed using the parts of the point cloud representing the face and ears. This allowed an assessment to made of whether facial features could be used to perform accurate registration.

The distances were again calculated from the image points to the nearest mesh points: in this case distances over 5 mm are shown in dark blue (Fig. 3.10). The median distance for the six point clouds is 2.23 mm (Fig. 3.8). Since several months elapsed between taking the MRI data and taking the surface capture data, it is possible that there may have been some slight changes in the subject's features. In addition, in the MRI scanner the subject would have been in a supine position, while the subject was sitting upright for the surface capture images. During neurosurgery the subject is likely to be in a prone position. It is possible that there was some distortion of features due to position and likely that changes in the expression of the face could have resulted in poor registration between the surface capture images of the subject and the MRI

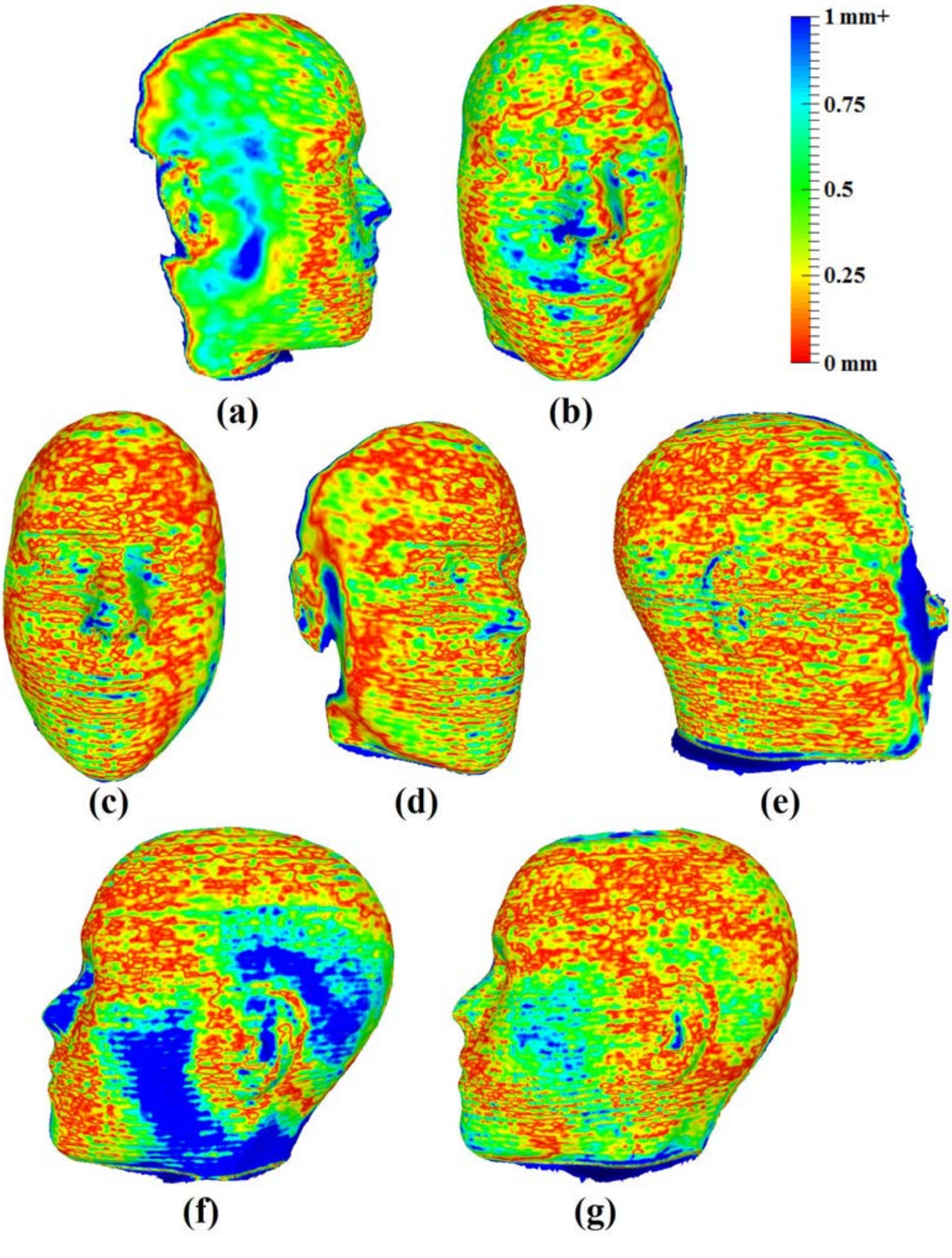

FIGURE 3.6: Surface capture images of phantom, registered to ground truth using ICP algorithm; colours show distance to ground truth: (a-b) two views of an image taken from the front right of the phantom, (c-d) another image taken from the front right, (e) image taken from the right side, (f-g) two images taken from the left side. All distances greater than 1 mm are shown in dark blue.

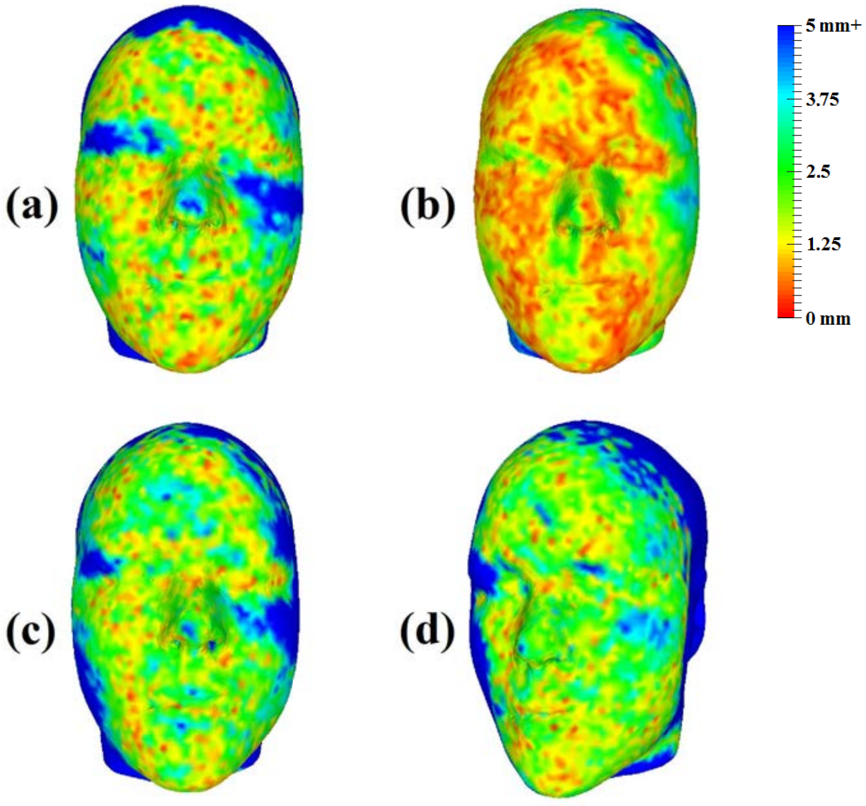

FIGURE 3.7: Phantom mesh registered to Kinect v1 images of phantom, using ICP algorithm; colours show distance to Kinect images, images taken from (a) 50 cm, (b) 60 cm, (c) 70 cm, and (d) 80 cm. All distances greater than 5 mm are shown in dark blue. The distances have been shown on the phantom as the point clouds are sparse.

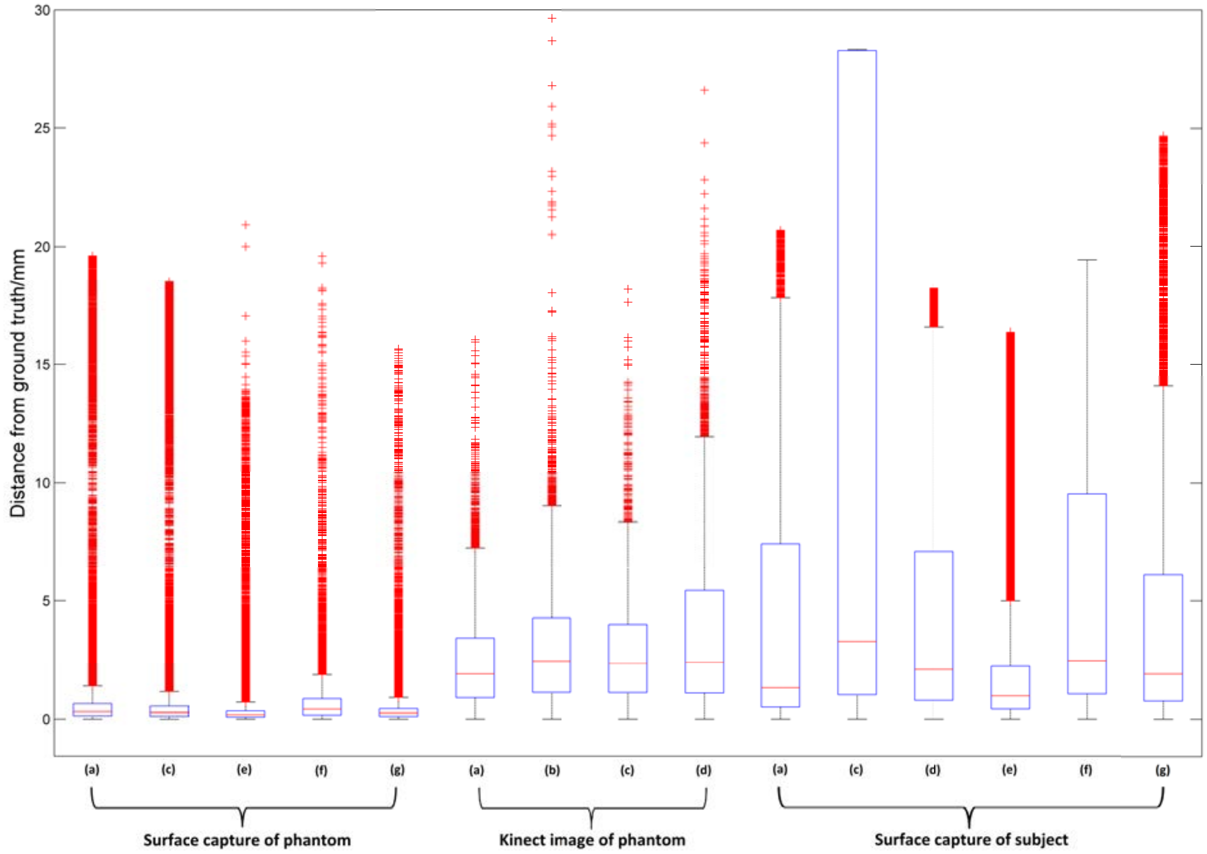

FIGURE 3.8: Distances from imaged point clouds to ground truth, after ICP registration, for (left-right) Birmingham system images of the phantom, Kinect images of the phantom, and Birmingham system images of the human subject, corresponding to Figs. 3.6, 3.7 and 3.10. The large number of outliers at higher distances is partly dependent on how closely the point clouds was manually cropped.

FIGURE 3.9: An unedited Kinect v1 phantom image, showing outlying points to the side of the head; shown from (left) the right side of the head and (right) the front.

surface point cloud. These results suggest that facial features may be unsuitable for performing registration.

3.4 Conclusion

Two imaging devices, Birmingham Surface Capture System and the Kinect v1, were investigated to see how well they could produce 3D images of a human head. Both devices were initially tested on a mannequin head and it was found that the Birmingham system produced point clouds which were more complete, smoother, and qualitatively more similar to the original surface. Both systems take a few seconds to perform imaging; the Birmingham system projects visible light patterns onto the subject, which may be more distracting in surgery.

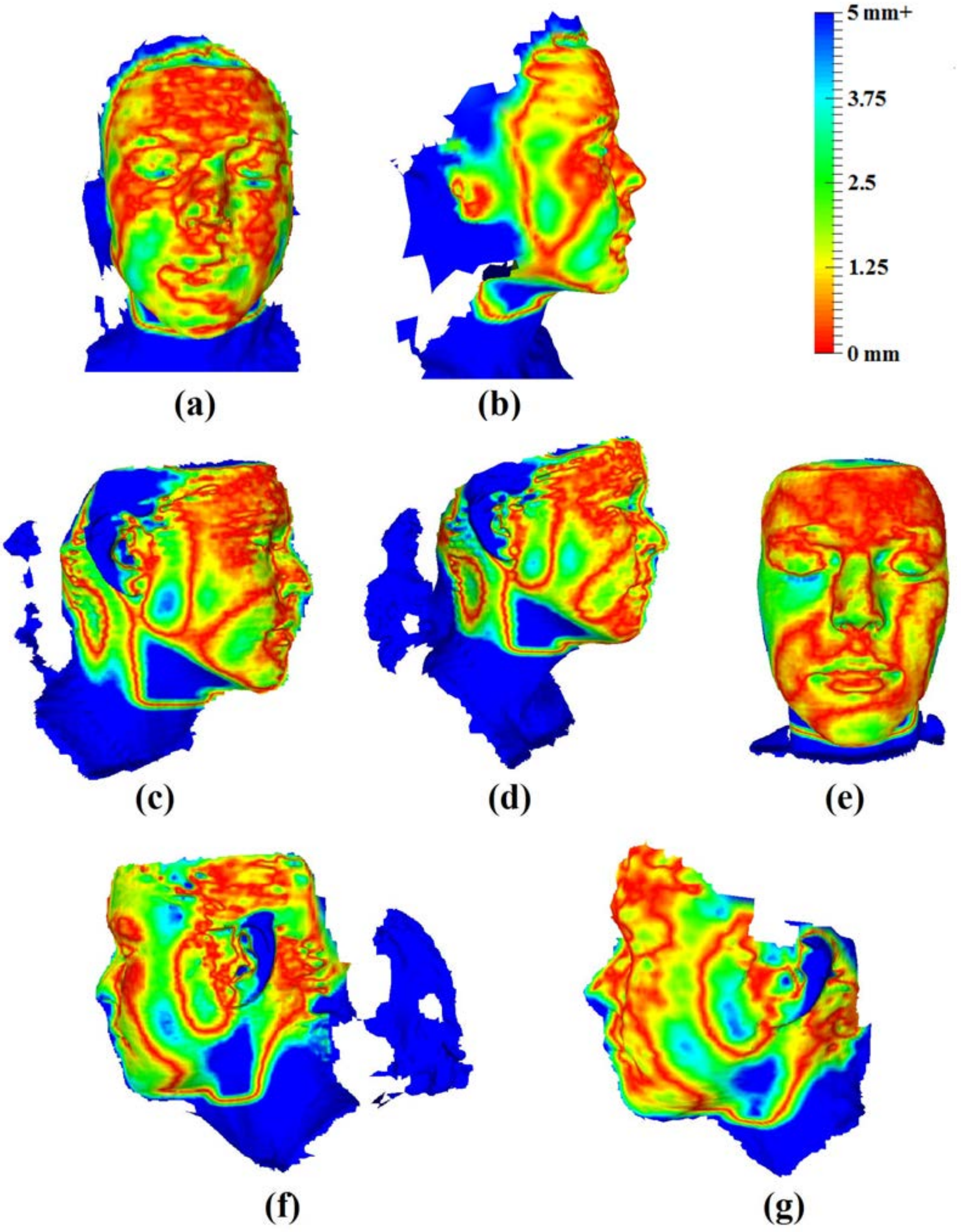

FIGURE 3.10: Surface capture images of human subject, registered to MRI 'ground truth' using ICP algorithm; colours show distance to ground truth: (a-b) two views of an image taken from the front, (c-d) two images taken from the right, (e) another image taken from the front, (f-g) two images taken from the left side. All distances greater than 5 mm are shown in dark blue.

The two systems were then used to image a phantom head, which had been produced using a surface extracted from an MRI image of a subject's head. The surface capture images were registered to the original surface mesh using ICP, as were surface capture images of the subject herself. The distance from each point in the surface capture data to the nearest point in the ground truth mesh was calculated and plotted as a colour. It was found that the Birmingham system data of the phantom was closer to the ground truth than the Kinect v1 data, with median distances from registered point clouds to ground truth of 0.269 mm and 1.80 mm, respectively. The point clouds produced by the Birmingham system were denser in the region of interest (facial features, as opposed to hair) than those from the Kinect.

The face and ears were used to perform registration of the subject, since the head surface was obscured by hair. It was found that the final alignments of the phantom images to the MRI point cloud were closer than those of the subject images. The data points from the four registered point clouds were a median 2.23 mm from the ground truth, suggesting that imaging facial features may not result in a sufficiently accurate registration for use in neurosurgery.

Surface capture images of the top and back of the phantom head, without facial features and ears, were taken. It proved to be difficult to register this data accurately with the ground truth, since it is a curved surface without distinctive landmarks. In addition, it may be impossible to image this type of surface in surgery, since it is likely to covered with drapes or hair. For this reason, in chapter 4, methods of partial registration are investigated. In order to separate the error which results from the registration method from that which originates in the imaging system, in the following chapters an idealised surface point clouds is used to investigate registration.

Chapter 4

Partial Registration Using the Iterative Closest Point Algorithm

4.1 Contributions to the work

MRI data was converted to a mesh by Xue Wu [108], all other work was done by the author.

4.2 Introduction

An essential part of stereotactic neurosurgery is accurate registration between the patient, preoperative images (CT/MRI) and the robot coordinate system, allowing accurate targeting within the brain. The Iterative Closest Point (ICP) algorithm is a simple and widely used registration algorithm for point clouds [109, 27]. In this chapter, the accuracy of ICP for registration between the patient, whose surface is to be recorded as a surface capture point cloud, and a second point cloud extracted from patient MRI data, is examined.

During surgery, it is likely that only a partial view of the head will be available. It may be possible to uncover some or all of the head in order to allow registration based on the maximum surface area available. The eyes, nose, and mouth may be covered or distorted by surgical equipment and are thus unavailable for registration purposes. For this reason, a region of interest (ROI) that excludes the face and ears is defined from the point clouds prior to testing the registration algorithm. Multiple views of the patient may be required in order to perform accurate registration; this could be done by attaching the imaging device to the robot arm. Full ROI surface registration using only parts of the ROI point clouds will be therefore examined in order to determine which parts of the head give the best registration accuracy; whether adding further ROI points taken from subsequent images will improve accuracy; and, if so, of which parts of the head they should be taken.

In this chapter, head surface point clouds extracted from MRI data are registered using ICP with re-meshed versions of themselves, in which the points are redistributed on the original surface; the latter represent idealised surface capture point clouds of the patient. This allows the algorithm to be tested without permitting the results to be affected by the accuracy of the imaging system. Registration accuracy is tested for a range of starting positions and using various proportions of randomly selected points from across the full point clouds. Partial registration is investigated by dividing the ROI point clouds into octants and testing the effects on accuracy of (i) registration using different parts of the head, and (ii) varying the total surface area used for registration. This is done by changing the number of octants used for registration, using multiple octants both simultaneously and sequentially. Registration is also performed using the centres of mass of the octants as landmarks, in order to investigate the accuracy achievable when using a small number of landmarks. It is hoped that octants are a sufficiently small region of the head that it will be possible to image one or more without obstruction.

4.3 ICP algorithm

The ICP registration algorithm determines the transformation necessary to move a 'source' point cloud, $\boldsymbol{Y} = (y_1, \ldots, y_M)^T$, into alignment with a 'reference' point cloud, $\boldsymbol{X} = (x_1, \ldots, x_N)^T$. This is done by iteratively estimating and improving the rotation and translation necessary to minimise the distance between point clouds. The distance or error function is calculated as the root mean square (RMS) distance between the points in the source point cloud and their nearest neighbours in the reference point cloud. At each iterative step of the algorithm, the following process is performed:

- Find the nearest reference point for each point in the source point cloud and calculate the RMS distance between the point clouds. The set of paired reference points is denoted by $\boldsymbol{X'}$.
- Estimate the transformation (translation, $\boldsymbol{t}$, and rotation, $\boldsymbol{R}$) that will most reduce the RMS distance, $T(\boldsymbol{Y}) = \boldsymbol{R}(\boldsymbol{Y}) + \boldsymbol{t}.\mathbf{1}$.
    - Translation is estimated by calculating the distance between the centres of mass of the point clouds.

$$t(\boldsymbol{Y}) = \boldsymbol{Y} - \boldsymbol{\mu_Y}.\mathbf{1} + \boldsymbol{\mu_{X'}}.\mathbf{1} \tag{4.1}$$

    where $\boldsymbol{\mu_Y}$ is the centre of mass (mean coordinate) of the points in $\boldsymbol{Y}$ and $\boldsymbol{\mu_{X'}}$ is the centre of mass of $\boldsymbol{X'}$.

- Rotation is estimated using the Kabsch algorithm [110][111], in which the optimal rotation matrix is calculated by singular value decomposition (SVD) of the covariance matrix of the two sets of point cloud coordinates.

  $$\boldsymbol{A} = (\boldsymbol{Y} - \boldsymbol{\mu_Y}.\mathbf{1})(\boldsymbol{X'} - \boldsymbol{\mu_{X'}}.\mathbf{1})^T \tag{4.2}$$

  Using the SVD of the covariance matrix

  $$\boldsymbol{A} = \boldsymbol{V}\boldsymbol{S}\boldsymbol{W}^T, \tag{4.3}$$

  The optimal rotation matrix, $\boldsymbol{R}$, is:

  $$\boldsymbol{R} = \boldsymbol{W}\begin{pmatrix} 1 & 0 & 0 \\ 0 & 1 & 0 \\ 0 & 0 & d \end{pmatrix}\boldsymbol{V}^T \tag{4.4}$$

  where $d = sign(\det(\boldsymbol{W}\boldsymbol{V}^T)).\mathbf{1}$.

- Transform the source points to their new location using the transformation calculated.

The process is repeated until the stopping conditions are met (Fig. 4.1). Stopping conditions can include a maximum number of iterations, a maximum RMS distance (absolute or relative to point cloud size), and a maximum change in RMS distance over a given number of iterations. The software used to perform ICP registration was adapted from Wilm [112].

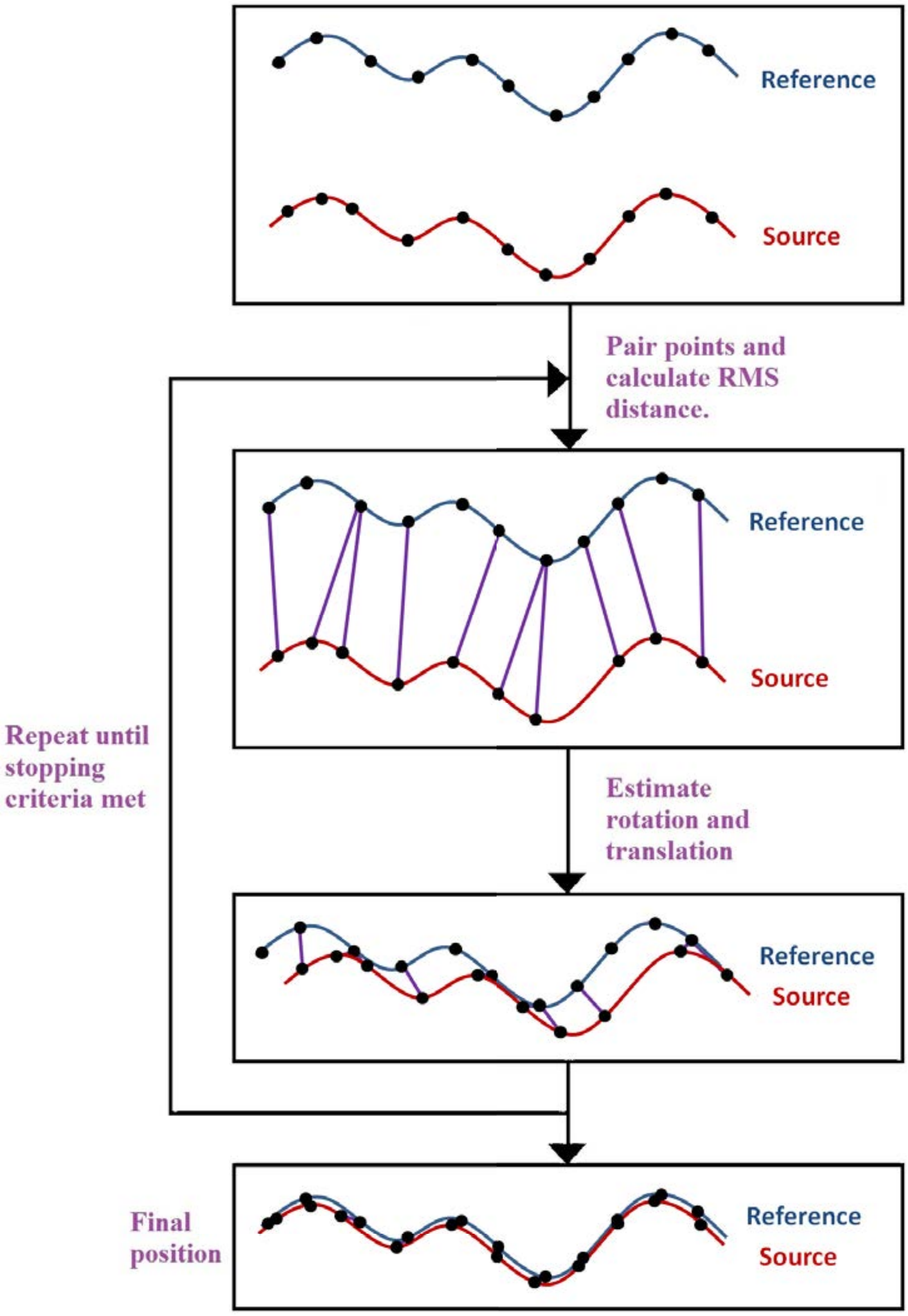

FIGURE 4.1: ICP algorithm: in each iteration each point in the source cloud (red) is matched to its nearest point in the reference cloud (blue). The transformation is then estimated that will bring the source cloud into best alignment with the reference cloud based on the 'point-to-point' RMS distance between pairs of points.

4.4 Methods

4.4.1 Point cloud creation and re-meshing

In order to investigate registration methods independent of imaging technique, surface point clouds were extracted from the MRI data of ten healthy adult subjects using NIRFAST software [46]. The data sets were obtained as part of research approved by the Human Research Protection Office at Washington University School of Medicine, informed consent was obtained.The MRI data was received in the form of a mesh (see section 4.1) representing the full volume of the MRI; surface points were isolated by taking the nodes which were attached to boundary faces. In order to select a region of interest that only contains the top of the head, excludes facial features and ears, and is consistent across all subject models, two fiducial points were selected and used: the inion and the nasion (Fig. 4.2e). These are defined as the external occipital protuberance of the occipital bone and the middle of the frontonasal suture, respectively. In order to create an idealised point cloud to register to the initial 'ground truth' point cloud, each ROI point cloud was re-meshed in MeshLab [103] by the following process: the outer-pointing normal was calculated for each surface point using its 100 nearest neighbours; a surface mesh for the ROI was created using the algebraic set surfaces variant of the marching cubes algorithm [113], with a grid resolution of 1,000; Poisson-disk sampling was performed to give a point cloud with approximately the same number of points as the initial point cloud (a difference of less than 0.5% in all cases).

Data on the point clouds extracted from the ten subjects is given in Table 4.1. The surface areas of the ROI point clouds were found using the 'Compute Geometric Properties' filter in MeshLab [103] on meshes created from the ROI point clouds by the method for re-meshing described above.

Head number	Number of nodes (full point cloud)	Number of nodes (ROI surface point cloud)	Number of nodes (re-meshed ROI surface point cloud)	Surface area $/cm^2$
1	426999	13907	13844	243.1
2	472286	15630	15604	256.0
3	350520	12712	12766	250.5
4	421930	14126	14149	266.3
5	415376	14060	14021	241.9
6	405793	14417	14430	250.4
7	405325	14220	14183	246.9
8	382631	13373	13370	238.1
9	429856	15294	15265	264.6
10	467484	14703	14737	257.8

TABLE 4.1: Properties of point clouds extracted from subject MRIs

4.4.2 Evaluation of registration accuracy

Registration accuracy was primarily evaluated using the RMS distance between the point clouds after registration: for each point in the less populated point cloud, the nearest point in the other point cloud was found; the RMS distance between the pairs of points was used as a measure of the distance between point clouds. Where noisy or smoothed point clouds were used, the transformation calculated by the registration algorithm was applied to the original point cloud without added noise/smoothing and the RMS distance calculated using this, in order that the error measured should not be affected by the level of noise added to the point cloud. The RMS distance will not give an absolute measure of registration accuracy, but can be used to compare images from different modalities, does not depend on accurately determining the location of anatomical features, and allows consistency throughout the analysis.

4.4.3 Transformations

On creation, the re-meshed point clouds were co-localised with the original point clouds. A head-top region of interest (ROI) was selected from each point cloud, in order to test the registration algorithm on the area most likely to be available for imaging during surgery. The face was excluded because facial features are likely to be obscured or distorted during surgery by surgical drapes and equipment. The ROI was defined as a region which contains all points above a line passing through the inion and a point 2 cm above the nasion, with the head in an upright position. The ROI point clouds were then transformed using principal component analysis (PCA) so that their principal components were aligned with the x-, y- and z-axes, which maintained approximate alignment between them (orientation was checked by visual inspection of point clouds). This process was performed using the MATLAB 'pca' function [114].

The initial or 'ground truth' point clouds represent preoperative MRI data, to which a surface capture image would be registered. In order to obtain an idealised approximation of the surface capture data, the initial ROI point clouds were re-meshed, giving a second version of the same surface. This was done in MeshLab [103] using the following process:

1. Outer-pointing normals were calculated for each surface point using its 100 nearest neighbours. This is done by fitting a plane to the 100 nearest neighbours of each point. The direction of the normal is chosen arbitrarily and propagated to surrounding points, resulting in all normals either pointing out or in: this direction was checked manually and flipped if necessary.

2. A surface mesh for the head-top was then calculated using the algebraic set surfaces variant of the marching cubes algorithm [113], with a grid resolution of

1,000.

3. Poisson-disk sampling was then performed, specifying that the number of samples be the same as the number of points in the initial ROI, to give a point cloud of approximately the same density as the original.
4. The re-meshed head-tops extended slightly below the originals; this overhang was removed by re-cropping as defined earlier, using the nasion and inion (Fig. 4.2).

The original ROI and re-meshed point clouds (extracted from the MRIs of ten subjects) contained a mean of 14,244±852 and 14,237±839 points respectively. In all cases the number of points in the re-meshed point cloud was within 0.5% of the number of points in the corresponding original point cloud.

Upon creation, the re-meshed point clouds were in alignment with the ground truth head-top point clouds that they were taken from; the RMS distance between each pair of point clouds provides a minimum error for the registration process. The RMS distance was calculated by matching every point in the ground truth point cloud to its nearest neighbour in the re-meshed point cloud and taking the RMS of the Euclidean distances between these point pairs (points in the re-meshed clouds may be paired multiple times or not at all). This gives a mean distance over the ten heads of 0.886±0.062 mm. As there is no point-to-point correspondence between point clouds, this provides an approximate best value for the RMS distance between registered point clouds.

In order to perform registration, one of the point clouds had to be transformed to a new location. Rigid transformations of translation plus rotation are assumed because the MRI and surface capture images used here give absolute values for the size of the

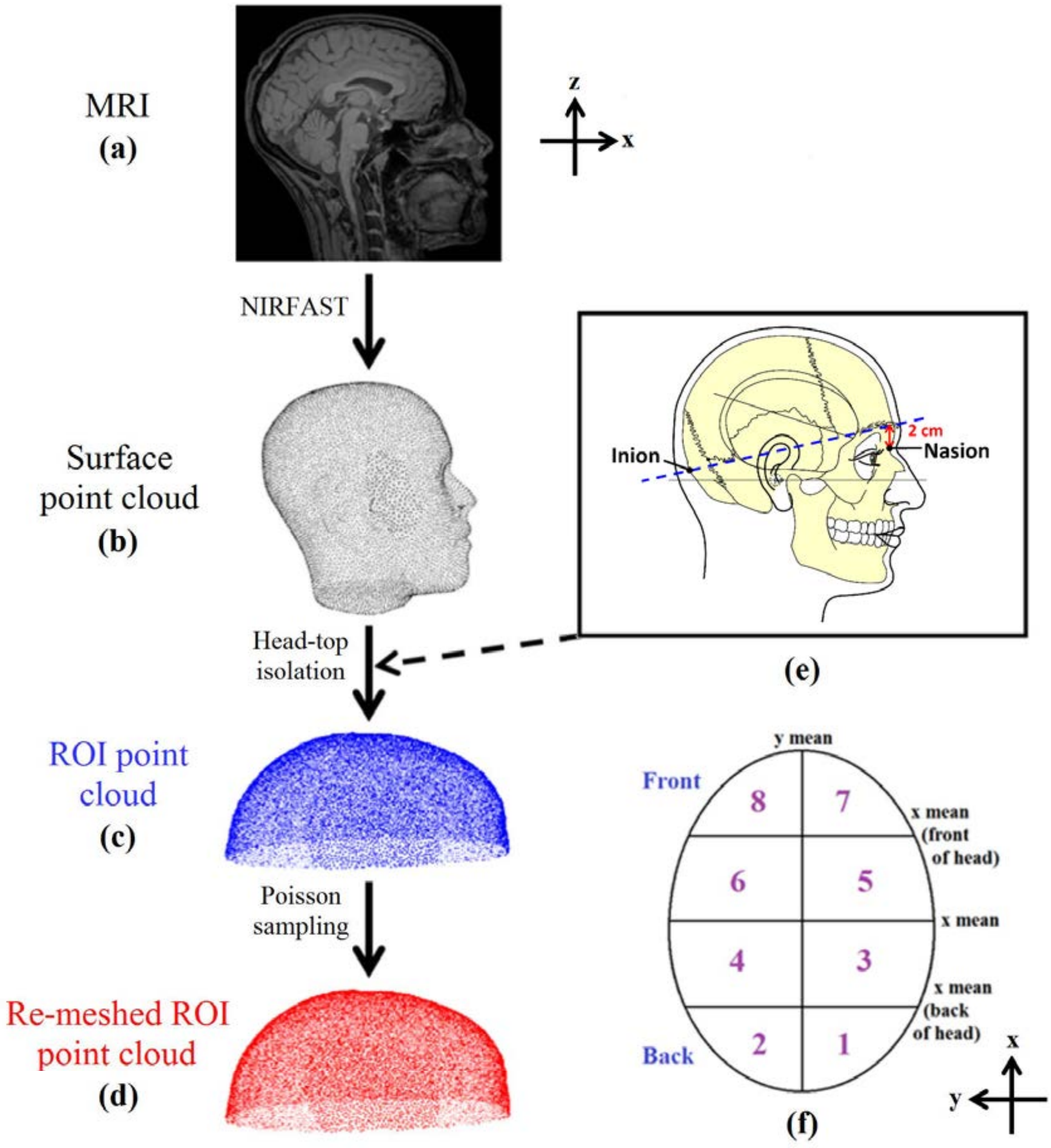

FIGURE 4.2: The process of creating test point clouds from MRI data (a). A surface point cloud (b) is extracted from the MRI data using NIRFAST [46] and the head-top (c) is isolated by removing points below a line from the inion to 2 cm above the nasion (looking along the y axis). The position of the inion and nasion on the skull can be seen in (e); only points above the blue line in this diagram are used. Poisson sampling is used to create a re-meshed head-top point cloud (d). To test the ability of the algorithm to register the whole head based on a small region, the head top point cloud is split into octants (f).

object imaged, so scaling is not required. Four transformations were used to evaluate the registration methods: rotations of $\pi/40$, $\pi/20$, $\pi/10$ and $\pi/5$ radians about the x-axis (the x-axis direction is from back to front of the head), followed by translations of 2, 5, 10 and 20 mm, respectively, in each of the x, y, and z directions. Rotation about the x-axis was chosen as an example rotation; the effects of rotation about the y- and z-axes are explored in chapter 7. Preliminary testing showed that if the ROI head top, as defined below, is initially transformed by $\pi/2$ or more, the ICP algorithm becomes stuck in a local minimum where the heads are inverted with respect to each other.

4.4.4 Surface registration

Registration was performed using the ICP algorithm as described in section 4.3. The error function for the algorithm was the RMS distance between the point clouds being aligned. Except where otherwise stated, the stopping criteria for the algorithm were that either (i) the maximum of 200 iterations were reached or (ii) the difference between the smallest and largest RMS distances for the last five iterations was less than 0.01% of the current RMS error. A maximum of 200 iterations was chosen as preliminary tests did not reach this limit.

4.4.5 Effect of proportion of points

The effect on registration accuracy of the proportion of points used in registration was examined. This will allow us to ensure that the detector used to perform imaging will provide a sufficiently dense point cloud. If a lower density cloud can be used without loss of registration accuracy, this could be used to speed up processing times. The comparison was done by performing registration using 10-100% of the original points, drawn randomly from the entire volume of each of the two point clouds. Four initial transformations of the re-meshed point cloud were used: rotations of $\frac{\pi}{40}$, $\frac{\pi}{20}$, $\frac{\pi}{10}$, and $\frac{\pi}{5}$ radians about the x axis, and corresponding translations of 2, 5, 10, and 20 mm in each of the x, y, and z directions (Fig. 4.3). Registration was performed five times for each transformation, for each of the 10 proportions used, randomly selecting the points from each point cloud each time.

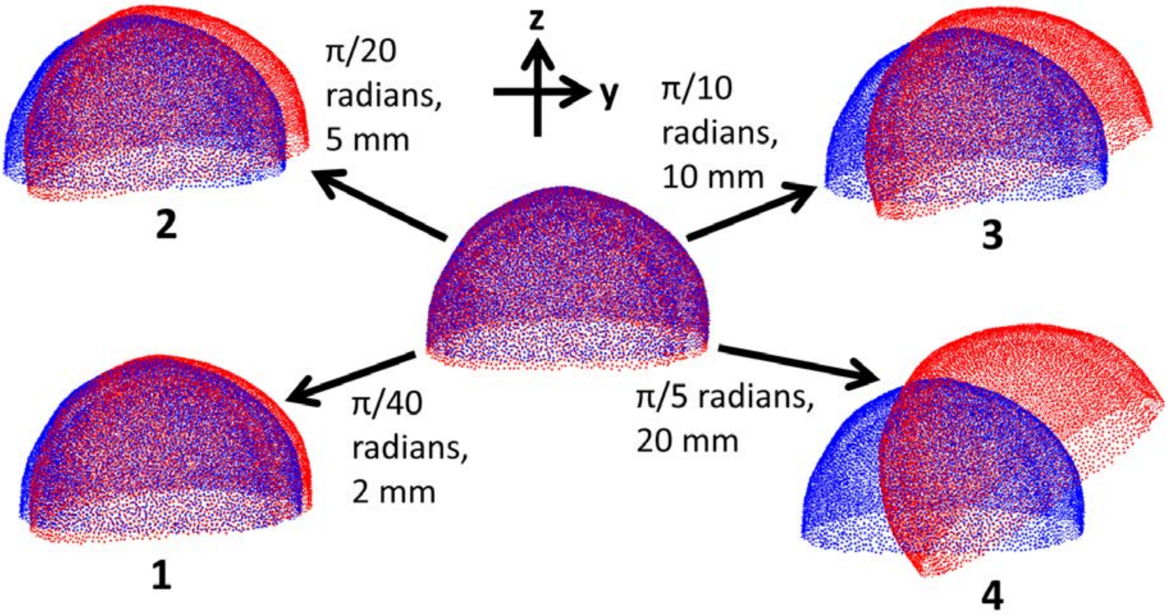

FIGURE 4.3: Four transformations (rotation and translation) of the re-meshed head-top point cloud (red), which is initially aligned with the original head-top point cloud (blue); rotations are about the x-axis.

An initial global alignment was performed by transforming the re-meshed point cloud (after application of the initial transformation) so that its principal components were aligned with the x-, y-, and z-axes (see section 4.4.3). Since the original ROI point cloud had already been transformed in the same fashion and the two surfaces are approximately the same, this brought the point clouds into approximate global alignment with each other.

The final transformation calculated by the ICP registration algorithm was then applied to the full re-meshed head-top and the RMS distance calculated between this and the full ground truth head-top, in order that the distance should be unaffected by point cloud density.

4.4.6 Registration by octants

It would be beneficial to spend as little time imaging as possible in surgery, to avoid disruption; in addition only a partial view of the head may be available. Therefore, once an image of the portion of the surface that is visible has been taken, it is useful to know where the robot/camera should move to take a subsequent image in order to most improve the registration error. In order to investigate this, both the initial and re-meshed head-top point clouds were divided into octants (Fig. 4.4) by dividing at the midpoint x and y coordinates, and additionally at the midpoint x coordinates of the front and back halves (Fig. 4.2).

In order to register the original and re-meshed head-tops, each octant, or combination of octants, was registered to the corresponding octant(s) in the other point cloud. Four initial transformations of the re-meshed head were used in each of the registration tests, as described in section 4.4.3. Larger rotations were not used as it was assumed that the approximate orientation of the patient's head would be known, so an initial global alignment step could be performed before registration.

4.4.7 Registration by octants' centres of mass

Registration can be performed more quickly if fewer landmarks are used. If the head is divided into octants, the minimum number of landmarks required to represent it is eight: one per octant. In order to incorporate all points within the octant, the centre

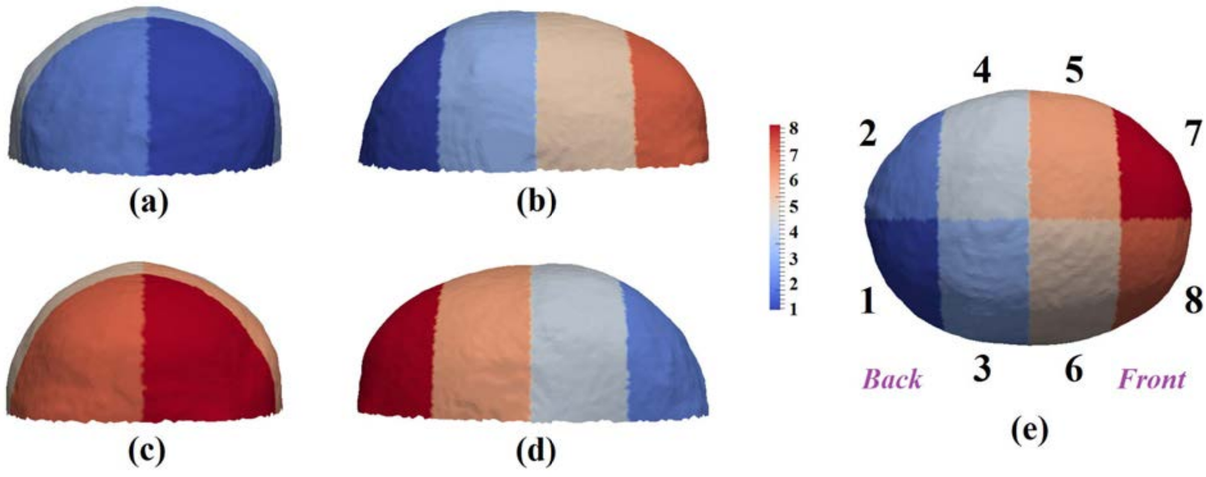

FIGURE 4.4: Head-top divided into octants, viewed along the (a) +x, (b) –x, (c) +y, (d) –y, and (e) -z axes. By splitting the point clouds into octants the effect on registration accuracy of the following can be examined: (i) using the octant centre of mass; (ii) using one or more octants; and (iii) adding octants to the registration process sequentially, repeating the registration process from the previous location each time an octant is added.

of mass can be used: this is a coordinate obtained by taking the mean coordinates of all the points in the octant. In this case initial rotations of between $\frac{\pi}{40}$ and $\frac{30\pi}{40}$ radians about the x-axis were used, in increments of $\frac{\pi}{40}$.

4.4.8 Registration by sequential octants

In order to determine which area of the head would provide the best registration accuracy, registration was performed with each source octant (from the re-meshed point cloud) individually, aligning it with the corresponding reference octant (from the initial point cloud). Initial transformations were as described in section 4.4.3. The mean RMS distance between the source and reference point clouds was then calculated using the whole ROI in the new position.

In order to determine whether the addition of a subsequent octant would improve registration accuracy, and which octant would give the best accuracy, registrations were performed using the initial octant and each possible second octant. In each case the points of the two octants to be used were combined to form a single point cloud, which began the registration process in the location determined by registration with the initial octant only. This allowed the best second octant, giving the best registration accuracy, to be determined. A maximum of 200 iterations was allowed for each octant added.

The process could then be continued to test which of the six remaining octants gave the best accuracy when combined with the first two and so on. This allows an optimal order for addition of the octants to be determined and the best possible improvement in registration accuracy at each stage to be calculated, allowing us to decide where to image initially to get the best registration, where to image subsequently to best improve registration accuracy, and how many areas it is worthwhile to image based on the improvement in registration accuracy. Where two octants were equally good the first numbered was chosen.

4.4.9 Registration using multiple octants simultaneously

In order to assess whether registration in the sequential fashion described above altered registration accuracy compared with registration using the same combination of octants simultaneously, registration was also performed using all possible combinations of between one and eight octants. In each case, the points from all source octants to be used were combined and then registered in a single step to the combined corresponding reference octants. A maximum of 2,000 iterations was set, in order to more fairly compare with sequential registration, where the maximum was 200 for each of up to eight stages.

4.4.10 Octant covariance

The shape and curvature of the octants may affect how useful they are in registration. In order to investigate this, the covariance matrix was calculated for each octant in each principle component aligned head-top, using the MATLAB built-in ‘cov’ function [114]. These were then compared with mean RMS error values for each octant, in order to determine whether the best octant to use for registration could be chosen based on its covariance.

4.5 Results

The effect on registration of the proportion of points used and the accuracy of registration by octants using the centre of mass, sequential, and simultaneous multiple-octant methods, described above, are evaluated. Results are given as [mean]±[standard deviation]. For each registration, both the iteration at which the process was stopped and the iteration with the lowest RMS distance were recorded. Where these were different, both values are given.

4.5.1 Effect of proportion of points used

The mean registration error (Fig. 4.5) decreases from 0.909±0.082 mm for 10% of points, to 0.817±0.025 mm for 40% of points, to 0.807±0.022 mm where all points are used. One-way ANOVA of mean RMS errors for the different proportions of point showed no statistically significant difference between the means for 40-100% of points, using Tukey-Kramer post hoc tests. This suggests that where computational time is a factor, a randomly selected set of 40% or more points from the original point clouds could be used with little loss of accuracy. However, this may depend on point cloud density. In the rest of this work, the full set of points has been used. The number of iterations used per registration was 48.8±23.4, with a maximum of 175.

4.5.2 Centre of mass registration

Centre of mass registration consistently achieves one of two possible positions (Fig. 4.6): a low error position, where the point clouds are approximately aligned, and a high error position, where the source point cloud is upside down (a local minimum). Where no initial alignment using PCA is performed, if the rotation is less than or equal to $\frac{17\pi}{40}$ radians, all head-tops tested achieve a relatively good registration with a mean RMS error over the head-top of 0.825±0.035. If the rotation is greater than or equal to $\frac{\pi}{2}$ radians, the mean RMS error is 26.9±0.60 mm. The total number of iterations used per registration was 6.45±0.99 and the best registration was at iteration 3.55±1.87. Where an initial alignment using PCA is performed, a rotation of $\frac{9\pi}{40}$ radians or less results in a mean RMS error of 0.825±0.035 mm, whereas an initial rotation of $\frac{11\pi}{40}$ radians or more results in 26.9±0.60 mm.

4.5.3 Division of point cloud into octants

The point clouds were divided into octants by the method described in section 4.4.6. The mean octant area produced was 2,974±125 mm^2; the mean number of points was 1,781±110 (original ROI point clouds). Octant area was determined by meshing octants using the ball-pivoting method (in MeshLab [103]) and summing the areas of all the

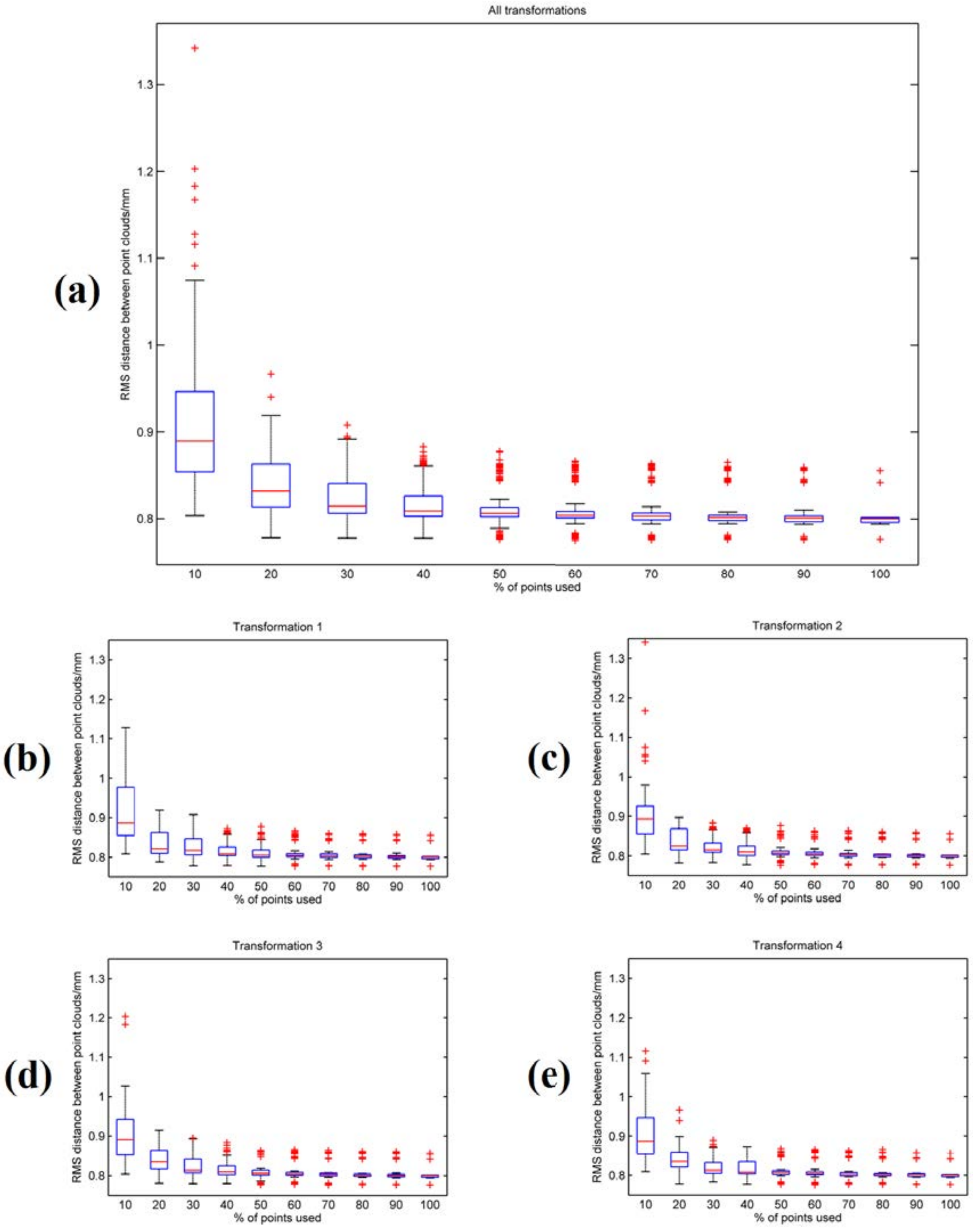

FIGURE 4.5: RMS distances between head-tops by proportion of points used, for (a) all transformations and (b-e) each transformation individually, where the rotations for transformations 1:4 are $\frac{\pi}{40}$, $\frac{\pi}{20}$, $\frac{\pi}{10}$, and $\frac{\pi}{5}$ radians and the translations are 2, 5, 10, and 20 mm along each axis.

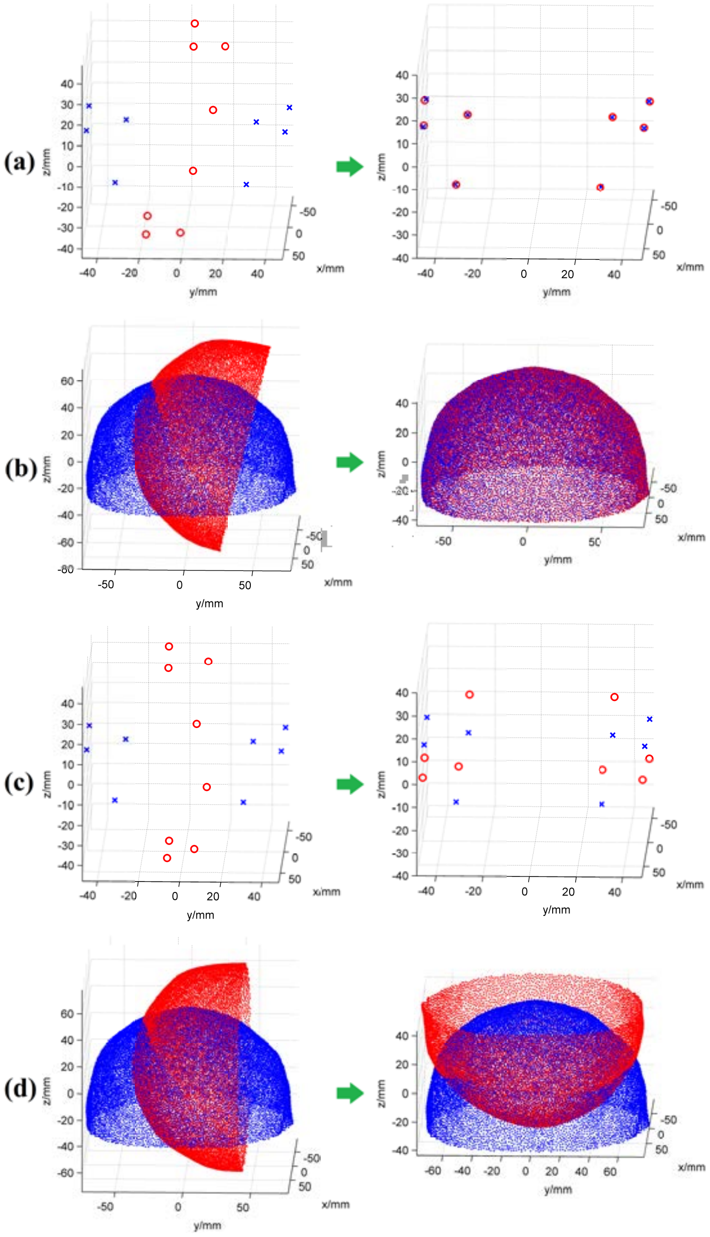

FIGURE 4.6: Centre of mass (COM) registration showing before (left) and after (right) registration positions of: (a) ground truth COM points (blue, crosses), re-meshed point cloud COM points (red, circles) rotated by $\frac{17\pi}{40}$ radians and (b) the corresponding full point clouds; (c) a) ground truth COM points, re-meshed point cloud COM points rotated by $\frac{\pi}{2}$ radians and (d) the corresponding full point clouds. The registered re-meshed point cloud in (b) has been aligned to approximately the original position, whereas in (d) it is upside-down.

faces in the resulting mesh. Kruskal–Wallis one-way ANOVA showed no significant difference between octants in octant area (p = 0.040) or number of points (p = 0.275).

4.5.4 Sequential octant registration of re-meshed head top to original head top

Sequential registration of re-meshed head-tops to the corresponding original head-tops was performed for all ten heads and four transformations, giving 40 test cases. The best overall octant order for each starting octant was determined at each stage by performing registration with each possible subsequent octant and choosing the octant that gave the lowest mean RMS distance between head-tops (Fig. 4.7).

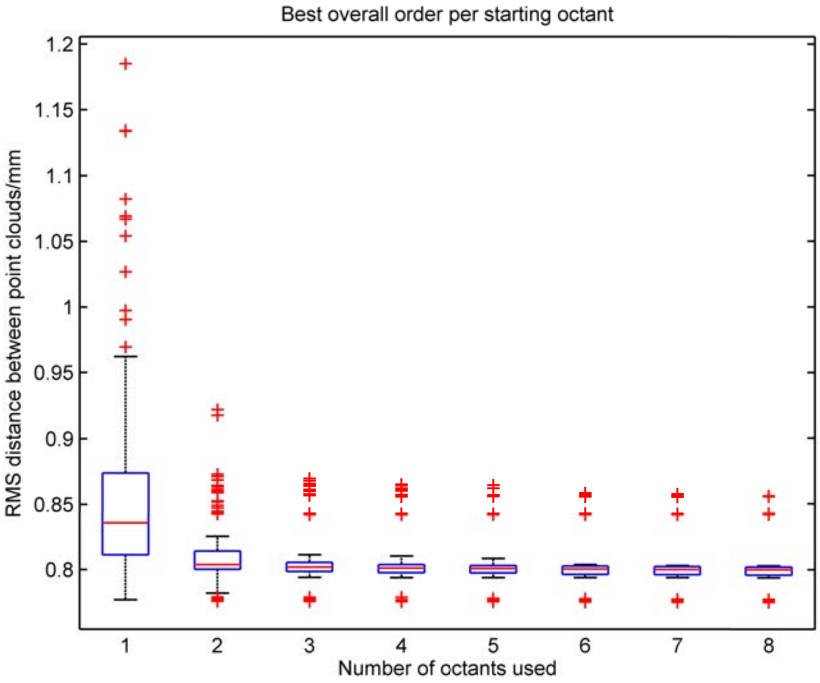

FIGURE 4.7: RMS distances between point clouds for sequential registration as subsequent octants were added, using an overall best order for each starting octant, across all subject heads and initial transformations.

One-way ANOVA was used for each starting octant to compare the change in RMS distance when using different numbers of octants. For starting octants 1, 2, 4, 5, 7, and 8, there was a statistically significant improvement in the mean RMS distance on adding the second octant (from 0.861±0.067 mm to 0.813±0.026 mm, using the mean values for all six starting octants), but not for subsequent octants. Where octant 3 is the starting octant, the RMS distance after adding the fourth octant is significantly different from after the first, but not the second and third octants (0.826±0.032 mm for the first octant, 0.808±0.023 mm for the fourth octant). Where octant 6 is the initial octant, there is no significant change on addition of any subsequent octant (RMS distance is 0.820±0.030 mm for the first octant). Octants 3 and 6 are in the centre of the head; it is possible that they provide a better initial registration, so the addition of subsequent octants makes less difference.

The mean number of iterations taken was 24.9±28.4, with a median of 12, and the maximum of 200 iterations was reached in 0.043% of cases (this is the number for one stage of the sequential process; when another octant is added, the iteration count is restarted).

Where the best order is chosen individually for each initial octant in each of the 40 trials, overall the mean RMS distance is only lower by a statistically significant amount when the 2nd octant is added and not for any subsequent octant (Fig. 4.8). This is true individually for starting octants 1, 2, 4, 5, 7, and 8, where the mean RMS distance after registration with the first octant is 0.861±0.067 mm and after the second octant is 0.809±0.023 mm. For starting octant 3, the improvement is statistically significant only for the third octant, with an RMS distance of 0.826±0.032 mm after the first octant is used and 0.807±0.023 mm after three octants have been used. For octant 6, no improvement is statistically significant.

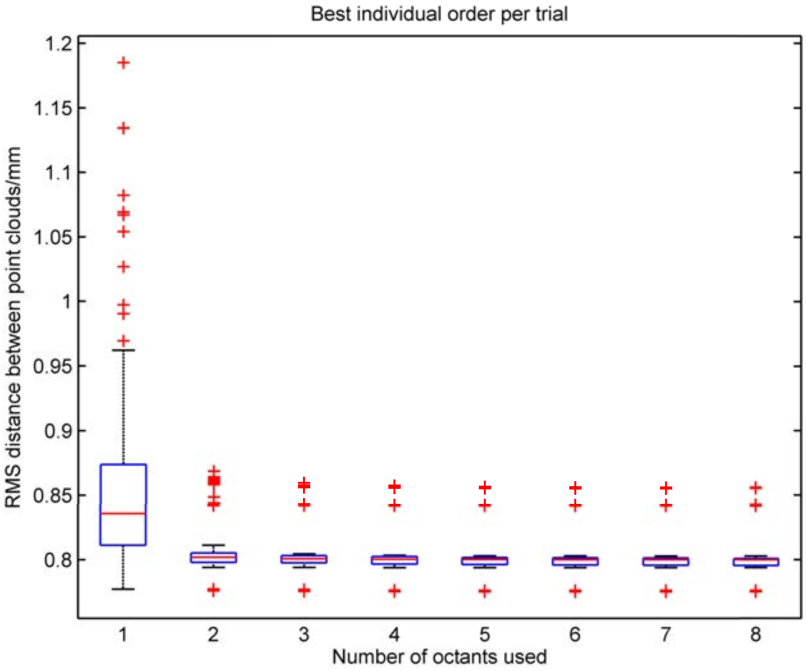

FIGURE 4.8: RMS distances between point clouds for sequential registration as subsequent octants were added. The best octant sequence was chosen for each head, transformation, and initial octant.

The mean RMS distance after one octant is 0.834±0.029 mm and decreases to 0.807±0.023 when all eight octants have been sequentially added. This suggests that in general only two octants are needed to obtain maximum registration accuracy. The mean number of iterations used was 21.9±28.0, with a median of 9, and the maximum of 200 iterations was reached 0.032% of the time.

4.5.5 'Inverse-crime': sequential octant registration of a head-top to itself

In order to determine whether the algorithm was capable of the best possible registration accuracy, the process from the previous section was repeated, but instead of using a re-meshed point cloud, each point cloud was transformed and then registered back to itself. The same four initial transformations were used for each subject as previously. If the registration algorithm is perfect the transformed head-top will be moved back to its exact original position, so the minimum error is zero. In addition to the previous criteria, the algorithm was set to stop if the error was less than 10^{-10} mm (preliminary testing suggested this value as suitable).

Using the sequential method, all initial octants obtained a lower mean RMS distance than when the re-meshed head-top was used (Fig. 4.9). However, the actual values were divided into cases where a very low RMS distance (less than 10^{-12} mm) was obtained and those where the RMS distance was 0.8 mm or higher. The latter value is similar to that found when performing sequential registration with re-meshed point clouds and implies the algorithm is getting stuck in local minima during registration.

For all initial octants, a very low RMS distance was obtained after the addition of a second octant, for at least some subjects and transformations. For initial octants 6 and 7, this value was obtained for all subjects and initial transformations after the third octant was added; for initial octant 1, it was obtained after the fourth octant was added. For other initial octants, for some subjects and transformations the RMS distance remained at approximately 0.8 mm, even when all octants had been added.

The mean number of iterations taken to converge was 14.1±19.2, with a median of 5, and the mean number to reach the best RMS distance was 12.6±19.9, with a median of 4 (again, this is for one stage in the sequential process). It is clear that for all these processes the distribution of number of iterations taken is skewed, with most trials requiring only a small number, but a very few reaching the maximum or close to the maximum. In this case, the maximum of 200 iterations was never reached; in all cases termination occurred when the error threshold was reached and the highest iteration number reached was 163.

4.5.6 Simultaneous registration of combinations of octants

All combinations of octants in the re-meshed heads were registered to the corresponding octants in the original heads for the four transformations given previously. The resulting mean RMS errors were similar to those for sequential registration (Figs. 4.10, 4.11). The mean number of iterations used was 136.9±42.2 and the maximum was 326. There was a statistically significant improvement on using two (0.820±0.034 mm) or three octants (0.812±0.025 mm) over one (0.852±0.062 mm). Using five or six octants was a statistically significant improvement over using three or fewer.

4.5.7 Length of time taken to perform registration

To compare the time taken to perform registration, both the simultaneous and sequential processes were run while the computer was not performing any other task (Fig. 4.12). The sequential process was run as in section 4.5.4 for the first two initial octants,

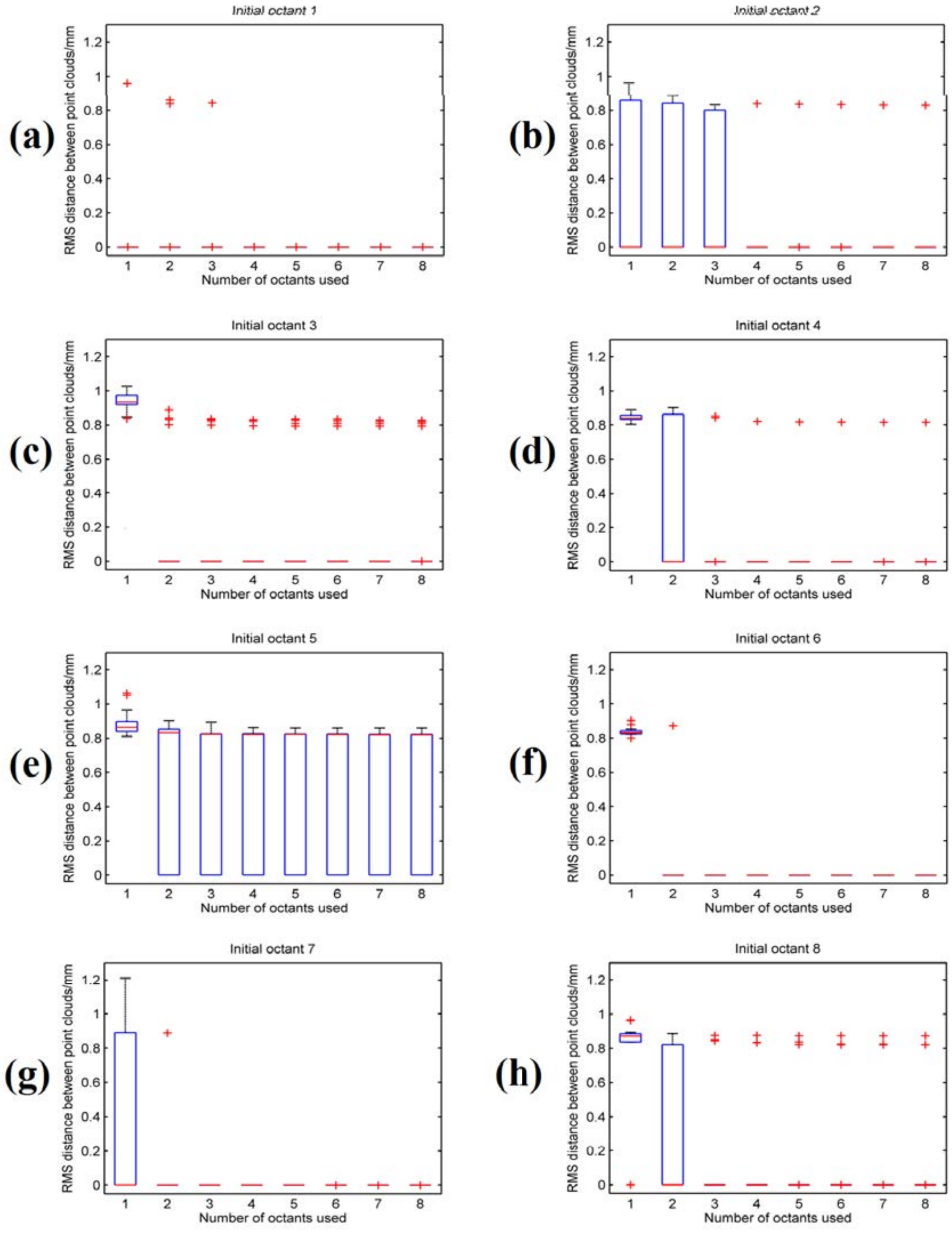

FIGURE 4.9: (a-h) RMS distances for starting octants 1 to 8, when registering head-tops back to themselves sequentially.

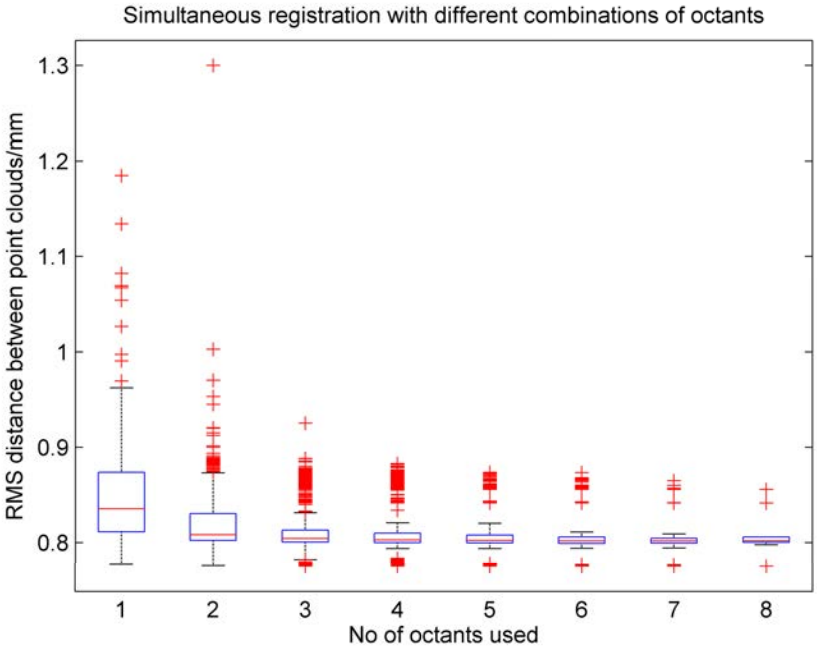

FIGURE 4.10: Mean RMS distances between head-tops for all combinations of octants used, by number of octants in combination.

using all ten subjects. The simultaneous process was run as in section 4.5.6, but for only two heads. The cumulative time taken by the sequential process for the best order is significantly less than the time taken by the simultaneous process for the same number of octants.

4.5.8 Effect of octant covariance on error

RMS registration error for each octant for each head-top was compared with octant covariance for all axes; Pearson's product moment correlation coefficient was calculated. None of the correlations are large, the largest being for the variance in the z direction ($r = -0.414$, $p = 1.05 \times 10^{-14}$).

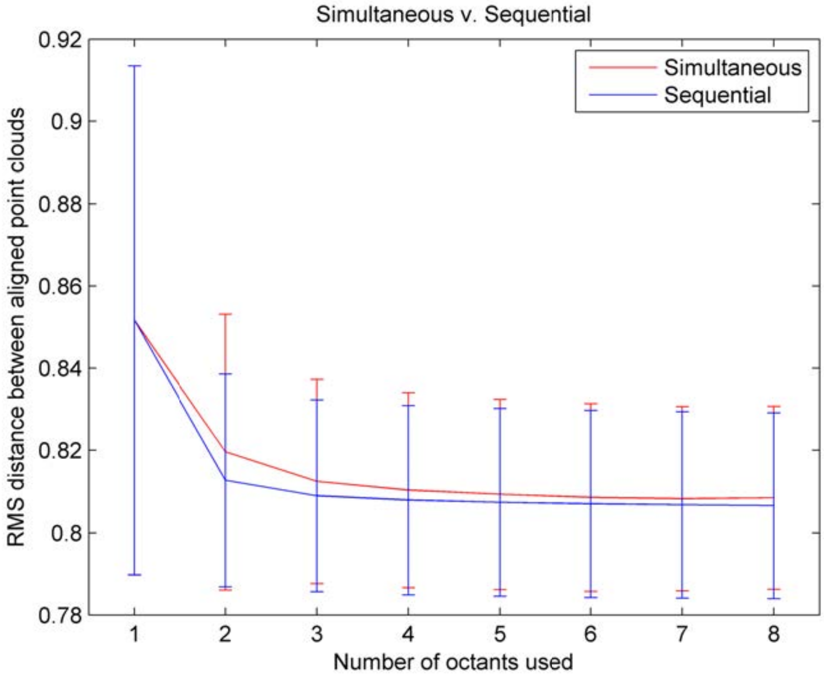

FIGURE 4.11: RMS error for sequential and simultaneous registration, error bars show standard deviation.

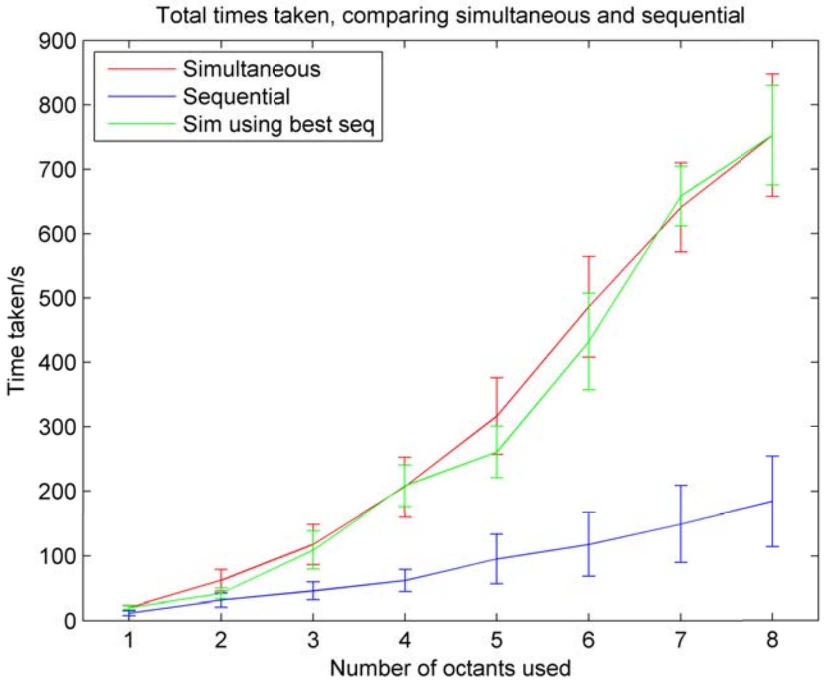

FIGURE 4.12: Time taken to perform sequential and simultaneous registration process. For the sequential process, the cumulative time taken is shown for the best overall sequence. The time taken for the simultaneous process using the same sequence is shown in green.

4.6 Discussion

4.6.1 Effect of proportion of points used

Testing with varying proportions of points, randomly selected from both the original and re-meshed point clouds showed that registration accuracy was not significantly affected where 40% or more points were used, suggesting that registration time could be reduced by this method, without compromising accuracy. This would however depend on the point cloud density obtained by the surface capture system.

4.6.2 Centre of mass registration

Centre of mass registration produced one of two results, a high and a low error situation. The low error mean RMS distance of 0.825 ± 0.035 mm is comparable to that produced by the sequential octant method, but the method is very reliant on both meshes being divided into corresponding octants, which would be difficult without having the point cloud for the whole head-top and without having accurate locations for the inion and nasion, in order to accurately define the octants on both meshes. In the high error situation, the point clouds are stuck in a local minimum where they are inverted with respect to each other, but this did not happen where the starting condition was a rotation of $\frac{17\pi}{40}$ radians or less; an initial alignment using all points could be performed to ensure this was the case. Initial alignment with principal components using only centre of mass points was not helpful, probably because there were too few points.

4.6.3 Sequential octant registration of re-meshed head top to original head top

In this instance, sequential registration between the re-meshed and original point clouds was performed. It was found that accuracy did not improve significantly after the first two octants were used, except when starting with octant 3, after which there was an improvement only on adding the third or fourth octant (depending on how the sequence is chosen, see section 4.5.4), or octant 6, after which there was no significant improvement on adding any octant. This suggests that registration could be performed using only part of the head surface, and that which part of the head is used is unimportant. However, the octants were defined using anatomical features on the head which might be unavailable or not accurately known, which would affect our ability to perform registration using this method.

4.6.4 'Inverse-crime': sequential octant registration of a head-top to itself

The ROI point clouds were registered back to themselves using the sequential octant method described in section 4.4.8. Since the point clouds are the same an RMS distance after alignment of zero is possible, but this was not reached in some cases, suggesting that the algorithm was stuck in local minima. Where the RMS distance was not close to zero, it was similar to the distance obtained using re-meshed point clouds.

4.6.5 Simultaneous registration of combinations of octants

Where all possible combinations of octants in the re-meshed point cloud were registered to the corresponding octants in the original point cloud, registration accuracy was not significantly different to when the same octants were used sequentially. However the time taken to register the same number of octants was significantly longer.

4.6.6 Effect of octant covariance on error

The effect of octant covariance on registration accuracy was examined to determine whether this could be used to determine which part of the head to image first. There was no strong correlation between octant covariance and RMS distance after registration of that octant.

4.7 Conclusion

Methods of registration between preoperative images and 3D surface capture images, for use in robotic neurosurgery, have been investigated. Head-top point clouds have been produced from ten different MRI scans and re-meshed; transformed versions of these have been used to test registration methods using the ICP algorithm. The head-tops have been divided into octants to simulate the partial views that may be available during surgery. Registration using a proportion of points, randomly selected, can still produce accurate results, but there is greater variation than when using the full point cloud and it would be important to retest this for the imaging system to be used, which might produce a different point cloud density than the surfaces used here. However, this method could be useful if it is necessary to speed up processing time.

Using the centres of mass of the octants as landmarks can enable reasonably good registration (a mean RMS distance between head-tops of 0.825 ± 0.035 mm), but is dependent on having a point cloud of the entire head-top in order to accurately define the octants which give the landmarks.

Registering by sequentially adding octants gave a mean RMS distance of 0.809±0.023 mm if two or more octants are used and the best order is chosen for each registration separately. This is the best value obtained by any of the tested methods; it is lower than the baseline value of 0.886±0.062 mm calculated from the initial position of the re-meshed head-tops before transformation. If the same sequence is applied to all heads and transformations, a mean RMS distance of 0.813±0.026 mm for the first two octants was obtained, suggesting that a predetermined sequence can be applied to the head-tops without loss of accuracy.

Registering by octants simultaneously gives similar results to sequential registration, the best mean RMS error obtained being 0.808±0.023 mm, for the octant combination: 1, 2, 3, and 6. This is equivalent to the accuracy of the sequential process, but the process takes considerably longer to perform. On comparing octant registration accuracy with covariance, very little correlation was found, suggesting this would not be an effective method of deciding which part of the head to image.

These results compare well with the application accuracies quoted in section 2.2.1 of 1.29 mm using fiducial markers [6] and 0.86±0.32 mm in a frame-based configuration [7]. However, idealised images have been used and any error due to the robot itself has not been included (Kajita et al. [89] found an RMS error of 0.12±0.10 mm when measuring neuromate® localisation accuracy). In addition the RMS error at the surface and not at the target point within the head has been found. Before the technique could be used in surgery, it would be necessary to test it using real surface capture images and corresponding MRI data. Initial rotation was about the x-axis only. It is not known what effect on accuracy other rotations might have. These could be tested with the same octant divisions. Other methods of dividing the ROI could be used and might affect registration accuracy differently.

ICP requires relatively good global registration of the point clouds in order not to get stuck in local minima. In the next chapter a probabilistic technique, coherent point drift (CPD), is examined and compared with ICP. Myronenko, Song, and Carreira-Perpinán [115] suggest that CPD performs better than ICP where the initial global alignment between point clouds is poor. CPD is also believed to be more robust to outliers and noise [47]. In chapter 5, ICP and CPD will be compared for whole ROI point clouds, using different levels of initial alignment, and for robustness to added noise and smoothed noise.

Chapter 5

Coherent Point Drift Algorithm

This chapter is based on work originally published in Cutter et al. [116].

5.1 Introduction

Coherent Point Drift (CPD) is a probabilistic point set registration algorithm, in which the only assumption is motion coherence [115] and registration is treated as a probability density estimation problem. Myronenko, Song, and Carreira-Perpinán [115] suggest that CPD reduces the need (as compared with ICP) to ensure that the point clouds are approximately globally aligned before starting the registration process; it can be used for both rigid and non-rigid transformations and is robust to noise and outliers [47]. The points of the source point cloud are represented as Gaussian mixture model (GMM) centroids (a mixture model probabilistically represents an overall population which contains subpopulations) and iteratively fitted to the reference point cloud by maximising the likelihood, i.e. finding the most probable alignment. The centroids are forced to move coherently (as a group) to preserve point cloud topological structure [47].

Myronenko and Song [47] tested CPD on example point clouds and showed it to be more accurate and robust to noise and outliers than ICP, using examples such as a rabbit, a fish and a face. These examples are not similar in shape to the head-top ROI point clouds used here, having more clearly defined features, and the effect on CPD accuracy of adding noise to them may differ to the effect of added noise on the ROI point clouds described in section 4.4.1.

In this chapter, CPD is utilised and evaluated in comparison with ICP for a pre-defined region of the head surface, examining the effect on registration accuracy of adding noise and smoothing the point cloud used to represent surface capture data. The effect on registration accuracy of different starting positions is also compared for the two algorithms, in order to determine whether initial global alignment makes a difference in this case.

CPD is suitable for both rigid and non-rigid registration. Here only the rigid version is used, as the imaging methods under consideration all produce rigid data; no scaling is required as the MRI and surface capture data used were of the same scale, providing distances in millimetres. As in the ICP algorithm, singular value decomposition (SVD) is used to find the optimal rotation matrix. In order to account for noise and outliers, a weighted uniform distribution is added to the Gaussian Mixture Model. The following description of the algorithm is based on those in Myronenko and Song [47] and Peng et al. [117].

5.2 Coherent Point Drift Algorithm

In the CPD algorithm, points from the source point cloud, $\boldsymbol{Y} = (\boldsymbol{y}_1, \ldots, \boldsymbol{y}_M)^T$, are treated as GMM centroids forming a probability density distribution (each point is treated as one centroid). This distribution is aligned to a second (reference) point cloud, $\boldsymbol{X} = (\boldsymbol{x}_1, \ldots, \boldsymbol{x}_N)^T$, which is treated as data drawn from the distribution generated from the first point cloud. The GMM centroids are reparameterised using a set of parameters, θ, and the algorithm seeks to determine a transformation $T(\boldsymbol{Y}, \theta)$, that will transform the points (or centroids) of $\boldsymbol{Y}$ into the closest possible alignment with $\boldsymbol{X}$. θ comprises rotation and translation terms.

The probability density function for the GMM centroids takes the form:

$$p(\boldsymbol{x}) = \sum_{m=1}^{M+1} P(m)p(\boldsymbol{x}|m) \tag{5.1}$$

where $p(\boldsymbol{x}|m) = \frac{1}{(2\pi\sigma^2)^{\frac{D}{2}}} \exp^{-\frac{||\boldsymbol{x}-\boldsymbol{y}_m||^2}{2\sigma^2}}$. D is the dimensionality of the point clouds, so $D = 3$ for the 3D point clouds used here. All GMM components are given the same isotropic covariance, σ^2, and equal membership probabilities, $P(m) = \frac{1}{M}$. In this notation, 'p' is used to denote the probability of a variable (in this case a point in the point cloud) and 'P' to denote the probabilty of an entire distribution.

An additional uniform distribution, $p(\boldsymbol{x}|M+1) = \frac{1}{N}$ is added to the mixture model to account for noise and outliers, with a weighting of ω, where $0 \leq \omega \leq 1$. The GMM centroids then take the weighting $1 - \omega$. The mixture model probability density function now takes the form:

$$p(\boldsymbol{x}) = \omega\frac{1}{N} + (1-\omega)\sum_{m=1}^{M}\frac{1}{M}p(\boldsymbol{x}|m) \tag{5.2}$$

The set of parameters, θ, used to reparameterise the GMM centroid locations are estimated by minimising the negative log-likelihood function:

$$E(\theta, \sigma^2) = -\sum_{n=1}^{N} \log \sum_{m=1}^{M+1} P(m) p(\boldsymbol{x}_n|m) \tag{5.3}$$

where the variables are assumed to be independent and identically distributed (i.i.d.).

Bayes theorem is used to give the posterior probability of a GMM centroid given a data point: $P(m|\boldsymbol{x}_n) = \frac{P(m)p(\boldsymbol{x}_n|m)}{p(\boldsymbol{x}_n|m)}$. This gives the 'correspondence probability' between any two points, $\boldsymbol{y}_m$ and $\boldsymbol{x}_n$.

An expectation-maximisation (EM) algorithm is used to iteratively find θ and σ^2. The parameter values are estimated as given below and used to compute $P^{\text{old}}(m|\boldsymbol{x}_n)$, the *a posteriori* probability distributions of the mixture components. This forms the expectation step of the algorithm. In the maximisation step, the new parameters are found by minimising the expectation of the complete negative log likelihood function, or objective function, with respect to the new parameters. Scaling terms are omitted in this work, because the point clouds are accurate in scale.

$$Q = -\sum_{n=1}^{N} \sum_{m=1}^{M+1} P^{\text{old}}(m|\boldsymbol{x}_n) \log(P^{\text{new}}(m) p^{\text{new}}(\boldsymbol{x}_n|m)) \tag{5.4}$$

In the rigid case, the objective function is given in terms of a rotation matrix, $\boldsymbol{R}$, a translation vector, $\boldsymbol{t}$, and σ^2:

$$Q(\boldsymbol{R}, \boldsymbol{t}, \sigma^2) = \frac{1}{2\sigma^2} \sum_{m,n=1}^{M,N} P^{\text{old}}(m|\boldsymbol{x}_n) ||\boldsymbol{x}_n - \boldsymbol{R}\boldsymbol{y}_m - \boldsymbol{t}||^2 + \frac{N_{\boldsymbol{P}} D}{2} \log(\sigma^2) \tag{5.5}$$

such that $\boldsymbol{R}^T\boldsymbol{R} = \boldsymbol{I}$, $\det(\boldsymbol{R}) = 1$. $N_{\boldsymbol{P}} = \sum_{n=1}^{N}\sum_{m=1}^{M} P^{\text{old}}(m|\boldsymbol{x}_n) \leq N$; $N = N_{\boldsymbol{P}}$ only if $\omega = 0$. P^{old} is calculated using the previous parameter values:

$$P^{\text{old}}(m|\boldsymbol{x}_n) = \frac{\exp^{-\frac{1}{2}||\frac{\boldsymbol{x}_n - T(\boldsymbol{y}_m,\theta^{\text{old}})}{\sigma^{\text{old}}}||^2}}{\sum_{k=1}^{M}\exp^{-\frac{1}{2}||\frac{\boldsymbol{x}_n - T(\boldsymbol{y}_k,\theta^{\text{old}})}{\sigma^{old}}||^2} + (2\pi\sigma^2)^{\frac{D}{2}}\frac{\omega}{1-\omega}\frac{M}{N}} \tag{5.6}$$

In order to apply SVD to the objective function, it must be rewritten:

$$Q = \frac{1}{2\sigma^2}[\text{tr}(\hat{\boldsymbol{X}}^T\text{d}(\boldsymbol{P}^T\boldsymbol{1})\hat{\boldsymbol{X}}) - 2\text{tr}(\hat{\boldsymbol{X}}^T\boldsymbol{P}^T\hat{\boldsymbol{Y}}\boldsymbol{R}^T) + \text{tr}(\hat{\boldsymbol{Y}}^T\text{d}(\boldsymbol{P}\boldsymbol{1})\hat{\boldsymbol{Y}})] + \frac{N_{\boldsymbol{P}}D}{2}\log(\sigma^2) \tag{5.7}$$

where $\hat{\boldsymbol{X}} = \boldsymbol{X} - \boldsymbol{1}\mu_{\boldsymbol{x}}^T, \mu_{\boldsymbol{x}} = \frac{1}{N}\boldsymbol{X}^T\boldsymbol{P}^T\boldsymbol{1}$, $\hat{\boldsymbol{Y}} = \boldsymbol{Y} - \boldsymbol{1}\mu_{\boldsymbol{y}}^T, \mu_{\boldsymbol{y}} = \frac{1}{N}\boldsymbol{Y}^T\boldsymbol{P}\boldsymbol{1}$ and the matrix $\boldsymbol{P}$ has elements $p_{nm} = P^{\text{old}}(m|\boldsymbol{x}_n)$. This is done by setting the partial derivative of $\boldsymbol{Q}$ with respect to $\boldsymbol{t}$ to zero, then substituting in the resulting expression for $\boldsymbol{t}$.

The optimal value of R is expressed as:

$$\boldsymbol{R} = \boldsymbol{U}\boldsymbol{C}\boldsymbol{V}^T \tag{5.8}$$

where $\boldsymbol{U}\boldsymbol{S}\boldsymbol{V}^T = \text{svd}(\hat{\boldsymbol{X}}^{\boldsymbol{T}}\boldsymbol{P}^{\boldsymbol{T}}\hat{\boldsymbol{Y}})$ and $\boldsymbol{C} = \text{d}(1, \ldots, 1, \det(\boldsymbol{U}\boldsymbol{V}^T))$.

The steps of the algorithm are as follows:

Initialisation $\boldsymbol{R} = \boldsymbol{I}, \boldsymbol{t} = 0, 0 \leq \omega \leq 1, \sigma^2 = \frac{1}{DNM}\sum_{n=1}^{N}\sum_{m=1}^{M}||\boldsymbol{x}_n - \boldsymbol{y}_m||^2$

E-step In the expectation step (E-step), for each centroid and point, the posterior probability/probability of correspondence, P, of the centroid given the data point is calculated:

$$p_{mn} = \frac{\exp^{-\frac{1}{2\sigma^2}||\boldsymbol{x}_n - (\boldsymbol{R}\boldsymbol{y}_m + \boldsymbol{t})||^2}}{\sum_{m=1}^{M} exp^{-\frac{1}{2\sigma^2}||\boldsymbol{x}_n - (\boldsymbol{R}\boldsymbol{y}_m + \boldsymbol{t})||^2} + (2\pi\sigma^2)^{\frac{D}{2}}\frac{w}{1-w}\frac{M}{N}} \tag{5.9}$$

M-step In the maximisation step (M-step), values of $\boldsymbol{R}$, $\boldsymbol{t}$ and σ^2 are found:

- $N_{\boldsymbol{P}} = \mathbf{1}^T \boldsymbol{P} \mathbf{1}$, $\mu_{\boldsymbol{x}} = \frac{1}{N_{\boldsymbol{P}}} \boldsymbol{X}^T \boldsymbol{P}^T \mathbf{1}$, $\mu_{\boldsymbol{y}} = \frac{1}{N_{\boldsymbol{P}}} \boldsymbol{Y}^T \boldsymbol{P} \mathbf{1}$
- $\boldsymbol{X} = \hat{\boldsymbol{X}} - \mathbf{1}\mu_{\boldsymbol{x}}^T$, $\boldsymbol{Y} = \hat{\boldsymbol{Y}} - \mathbf{1}\mu_{\boldsymbol{y}}^T$
- $\boldsymbol{A} = \hat{\boldsymbol{X}}^T \boldsymbol{P}^T \hat{\boldsymbol{Y}}$
- Use SVD to compute $\boldsymbol{A} = \boldsymbol{U}\boldsymbol{S}\boldsymbol{V}^T$
- $\boldsymbol{R} = \boldsymbol{U}\boldsymbol{C}\boldsymbol{V}^T$, where $\boldsymbol{C} = \mathrm{d}(1, \ldots, 1, \det(\boldsymbol{U}\boldsymbol{V}^T))$
- $\boldsymbol{t} = \mu_{\boldsymbol{x}} - \boldsymbol{R}\mu_{\boldsymbol{y}}$
- $\sigma^2 = \frac{1}{N_{\boldsymbol{P}} D}(\mathrm{tr}(\hat{\boldsymbol{X}}^T \mathrm{d}(\boldsymbol{P}^T \mathbf{1}))\hat{\boldsymbol{X}}) - \mathrm{tr}(\boldsymbol{A}^T \boldsymbol{R}))$

The E- and M-steps are repeated until convergence; the transformation determined by the algorithm is then $T(\boldsymbol{Y}) = \boldsymbol{Y}\boldsymbol{R}^T + 1\boldsymbol{t}^T$. Convergence is reached when one of the following occurs:

- The maximum number of iterations is reached.
- σ^2 is less than a chosen minimum value, which is set as ten times the floating point relative accuracy (2.204×10^{-15}).
- The tolerance is less than a chosen minimum value (default is 10^{-5}), where the tolerance at iteration i is defined as $|\frac{L_i - L_{i-1}}{L_i}|$, $L_0 = 0$ and

  $$L_i = -\sum_{n=1}^{N} \log(\sum_{m=1}^{M} exp^{-\frac{1}{2\sigma_i^2}||\boldsymbol{x}_n - (\boldsymbol{R}_i \boldsymbol{y}_m + \boldsymbol{t}_i)||^2} + (2\pi\sigma_i^2)^{\frac{D}{2}} \frac{w}{1-w}\frac{M}{N}) + \frac{DN \log \sigma_i^2}{2}. \quad (5.10)$$

  The tolerance is a measure of the convergence of Q (Eq. 5.5).

Optionally, the point clouds can be pre-normalised to zero mean and unit variance before the registration process is begun, and de-normalised to the initial size and (reference) position once registration is complete. Zero mean is achieved by subtracting the mean x, y, and z coordinates of the whole point cloud from the coordinates of each point in the cloud. Unit variance is achieved by dividing each point's x, y, and z coordinates by the RMS x, y, and z coordinates for whole the point cloud.

5.3 Methods

The ten original and re-meshed point clouds described in section 4.4.1 were used. The same four transformations were used: rotations of $\pi/40$, $\pi/20$, $\pi/10$ and $\pi/5$ radians about the x-axis, followed by additions of 2, 5, 10 and 20 mm, respectively, to all coordinates (x, y, and z). The four initial transformations are referred to as T1, T2, T3, and T4.

5.3.1 Adding noise and smoothing

In order to investigate the effect of noise on registration accuracy, noise was added to the re-meshed point cloud before registration, simulating the situation in which noisy data from a 3D imaging system is registered to a preoperative MRI image. The effect of smoothing the noisy point cloud was also examined. Registration was performed in both possible directions to determine the effect on accuracy, i.e. with the noisy or smoothed point cloud as source and the original (ground truth) as reference, and vice versa. Once registration is performed the calculated transformation can be reversed, to move the reference point cloud to the source, if this is more useful clinically.

In order to add noise, the standard deviation of the point cloud in the x, y, and z directions was calculated. Noise was then added to each coordinate of each point by adding a random number from a Gaussian distribution, of which the mean was zero and the standard deviation was a fixed percentage (1-10%) of the standard deviation of the point cloud in that direction (Fig. 5.1). Smoothing of the noisy point clouds was performed in MeshLab [103] using the 'Laplacian Smooth' filter, using three iterations: at each iteration, each point is moved to the average position of its adjoining vertices, calculated using cotangent weighting (nearer points are given greater weight) and the boundary is smoothed independently as a line.

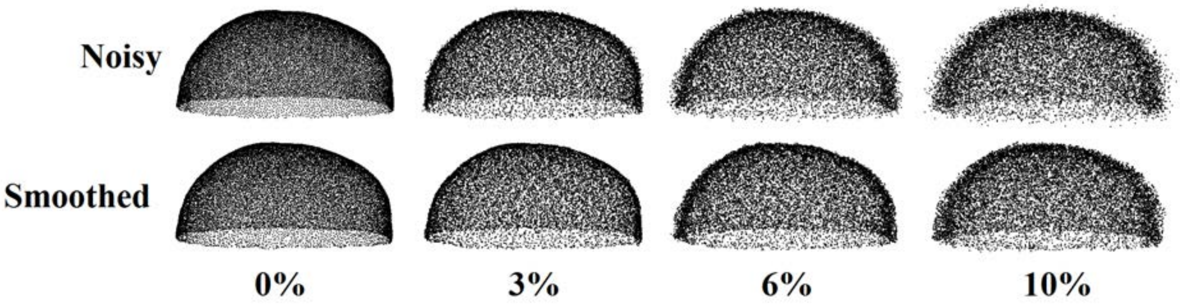

FIGURE 5.1: Point clouds with various amounts of added noise (top); (bottom) the same point clouds after smoothing.

5.3.2 The Iterative Closest Point (ICP) and Coherent Point Drift (CPD) registration algorithms

ICP registration was performed using singular value decomposition to estimate the required transformation at each step of the iteration (as described in section 4.3), with a maximum of 200 iterations. The maximum number of iterations was chosen as a result of preliminary testing showing that the 200th iteration was rarely reached; a maximum was needed in case the algorithm did not stop as expected due to an error. As an initial step, the source point cloud was translated such that its centre of mass was co-located with the centre of mass of the reference point cloud.

CPD registration was performed using the MATLAB toolbox described and built by Myronenko and Song [47]. The fast Gauss transform option was used to compute matrix-vector products, except in instances where this produced non-finite values, when a naïve approach (standard matrix multiplication) was used instead. A maximum of 200 iterations was again used. The CPD code has an option to normalise the data before registration, transforming it to zero mean and unit variance before registration and de-normalising it afterwards. Registration was tried both with and without this option.

In addition to the previously described stopping criteria, both methods used the condition of stopping when the difference between the smallest and largest RMS distances for the last five iterations was less than 0.01% of the current RMS error, as for ICP registration, described in section 4.4.4. This was because preliminary testing suggested that the CPD registration process did not always stop at the minimum RMS distance. Also, during the registration process, the transformation and RMS error at each iteration were recorded and, upon convergence, the iteration with the minimum RMS error was identified and the corresponding transformation parameters used for the final registration.

5.4 Experiments and Results

ICP and CPD were evaluated for registration using re-meshed, noisy and smoothed point clouds, in order to evaluate the accuracy achieved by each algorithm. Registration accuracy was again evaluated using the RMS distance between point clouds. The effects of prealignment using PCA were investigated, as described in section 4.4.3. Statistical testing was performed in R [118], using a significance level of $p \leq 0.01$; a low p-value is chosen to reduce the risk of false positives, particularly as the sample size is not large. A maximum of 200 iterations per registration was chosen based on prior results. The iteration number at which the algorithm converged was recorded as well as the time taken to reach convergence.

The following comparisons of registration methods were made:

a. Registration of the re-meshed ROI point cloud to the corresponding original ROI point cloud using each of (i) ICP, (ii) CPD without pre-normalisation (referred to as CPD1), and (iii) CPD with pre-normalisation (referred to as CPD2).

b. The same registrations as in (a) with differing levels of noise added to the re-meshed point cloud.

c. The same registrations as in (b), but with smoothing applied to the noise.

The number of iterations required is discussed in section 5.4.4 and the time taken in section 5.4.5. How well each algorithm works on differently shaped point clouds is also examined briefly in section 5.5.

5.4.1 Comparison of ICP and CPD for the whole ROI, with no added noise

For each of the ten subjects, the re-meshed ROI point cloud was put through each of the four transformations described in section 4.4.3 (T1-4) and registered to the 'ground truth' ROI point cloud for that head, both with and without initial alignment using PCA. Each registration was performed using (i) ICP, (ii) CPD without prenormalisation (CPD1), and (iii) CPD with prenormalisation (CPD2). The RMS distances between registered point clouds for each subject and transformation were found (Fig. 5.2), giving ten results for each combination of registration method, initial transformation and whether prealignment was used.

Each set of data was tested for normality using the Shapiro-Wilk test and in no case was found to vary significantly from the normal distribution ($p > 0.01$). On performing Bartlett's test for homogeneity of variance, a significant deviation from homogeneity was found ($p = 6.50 \times 10^{-3}$). For this reason, the Kruskal-Wallis test, a non-parametric method, was used for statistical comparison of results. Post hoc testing was performed using the Dunn test for multiple comparisons, with p-values adjusted using the Benjamini-Hochberg method [119]. The results for the different variables are given below.

5.4.1.1 Registration method

It was found that the registration method used had a significant effect on the post-registration RMS distance between point clouds ($p < 2.2 \times 10^{-16}$). When post hoc testing was performed, no significant difference in RMS distance was found between a registration performed using ICP and the equivalent registration (with the same initial transformation and use or not of PCA prealignment) using CPD1 ($p \geq 0.0789$). For ICP and CPD2, a significant difference was seen in all cases ($p \leq 5.69 \times 10^{-3}$), with ICP performing better than CPD2. Where the RMS distance was compared for CPD1 and CPD2 (CPD without and with prenormalisation, respectively), there was a significant difference ($p \leq 3.01 \times 10^{-3}$) in all cases, except for when T4 and prealignment with PCA were used; CPD1 performed better in each case.

The mean RMS distance between nearest points when using ICP was 0.884±0.048

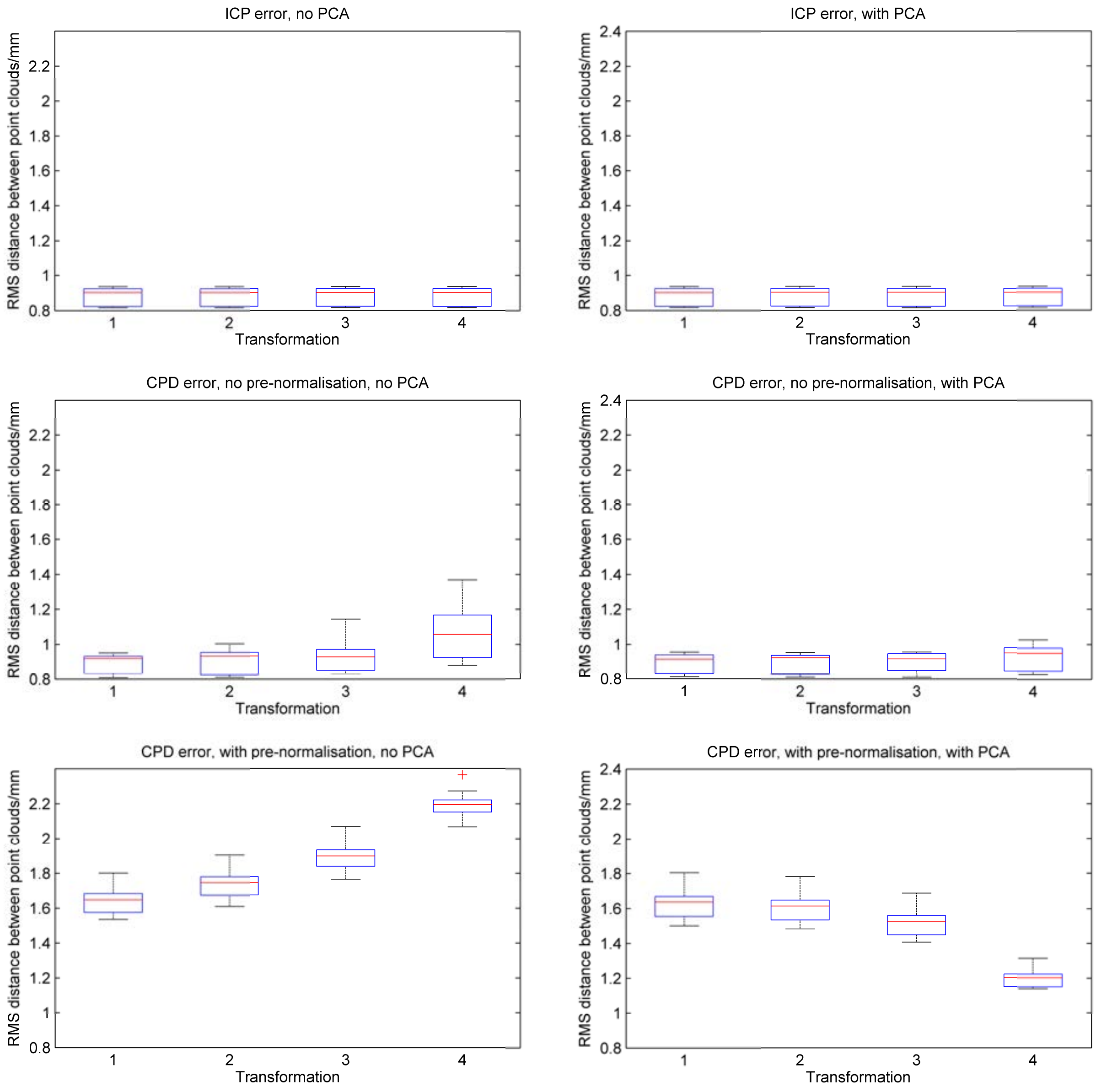

FIGURE 5.2: RMS error between point clouds after registration with (top-bottom) ICP, CPD without pre-normalisation (CPD1), and CPD with pre-normalisation (CPD2), for four different initial transformations, without (left side) and with (right side) initial alignment using PCA.

mm across all initial transformations and both prealignment options. Where prealignment was not used, the RMS distance for CPD1 varied between 0.892±0.056 mm for T1 and 1.06±0.161 mm for T4. Where prealignment with PCA was used, the mean RMS distance was 0.901±0.061 mm across all initial transformations. The mean RMS distance for CPD2 registration without prealignment varied from 1.65±0.08 mm for T1 to 2.20±0.08 mm for T4. Where prealignment with PCA was used, mean distance decreased from 1.63±0.09 mm for T1 to 1.20±0.05 mm for T4.

CPD1 therefore achieves similar RMS distances to ICP for small initial transformation, but its performance worsens for larger initial transformation where ICP's does not. CPD2 performs worse than ICP and CPD1 for all initial transformations. This implies that CPD2 is not finding the global minimum, perhaps suggesting that the steps it takes are not large enough to escape a local minimum. Normalising the point cloud to have unit variance in each of the x, y and z directions may distort the shape of the point cloud and affect registration performance, since making the length in the x direction (front to back) the same as that in the y direction (side to side) would increase the rotation symmetry of the point cloud, making the head shape almost circular.

5.4.1.2 Initial transformations

The initial transformation used had no significant effect on RMS distance after registration for any registration method, whether or not prealignment with PCA was used ($p = 0.773$, Kruskal-Wallis test). However, it is clear from Fig. 5.2 that for CPD1 there is some increase in RMS distance with larger initial transformation, whereas for ICP this is not evident. CPD2 shows an increase in RMS distance with greater initial transformation where no prealignment is used, but shows a decrease where prealignment with PCA is used.

That CPD performance is more affected by initial global alignment than ICP is contrary to the finding of Myronenko, Song, and Carreira-Perpinán [115]. This may occur because the ROI point clouds are relatively smooth and featureless, which may make it harder to isolate the precise global minimum; this effect may be heightened by use of a PDF to represent one point cloud. The effect of point cloud shape on registration accuracy is examined further in section 5.5.

5.4.1.3 Prealignment using PCA

Whether prealignment with PCA is performed does not make a significant difference to the RMS distance after registration, irrespective of registration method or initial transformation ($p = 0.0665$, Kruskal-Wallis test). There is a general, but not significant trend, for RMS distance to increase with initial transformation when CPD2 is used without prealignment, but to decrease with initial transformation when prealignment with PCA is used. Prealignment may improve accuracy by providing a better starting position.

5.4.2 Effect of noise on registration accuracy

In order to simulate the effect of noise on registration accuracy, for each re-meshed point cloud, ten noisy point clouds were produced with between 1% and 10% added noise, as described in section 5.3.1. Each noisy point cloud was put through the four transformations described in section 4.4.3, and registered to the ground truth (original ROI surface point cloud) using ICP, CPD1, and CPD2 (Fig. 5.3). Registration was also performed in the opposite direction, by transforming the ground truth, as above, and registering it to the noisy, re-meshed ROI point cloud (Fig. 5.4).

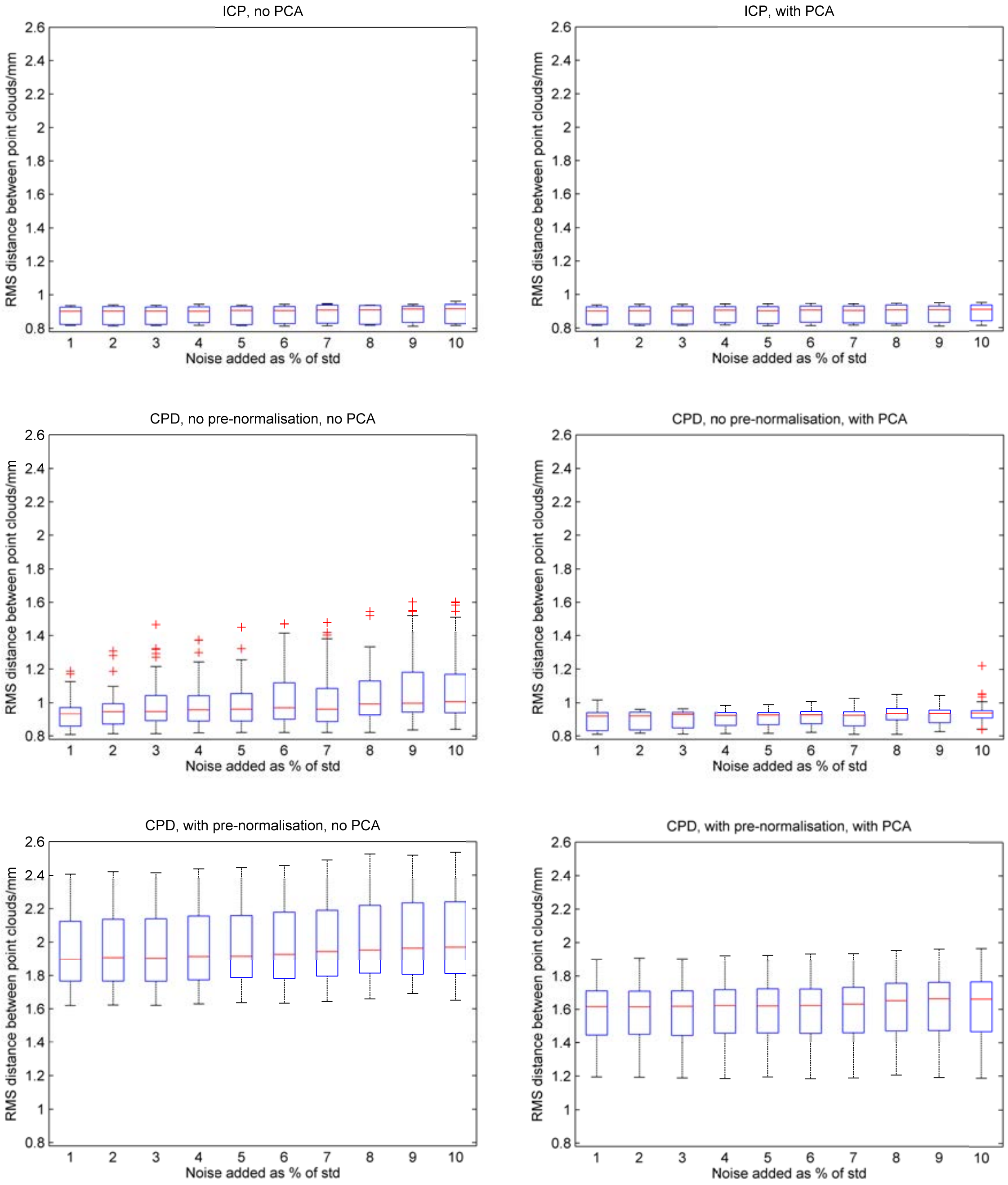

FIGURE 5.3: Variation of RMS error between point clouds with percentage of noise added after registration of noisy, re-meshed point clouds to ground truth. Registration methods used were (top-bottom) ICP, CPD1, and CPD2; without (left side) and with (right side) initial alignment using PCA.

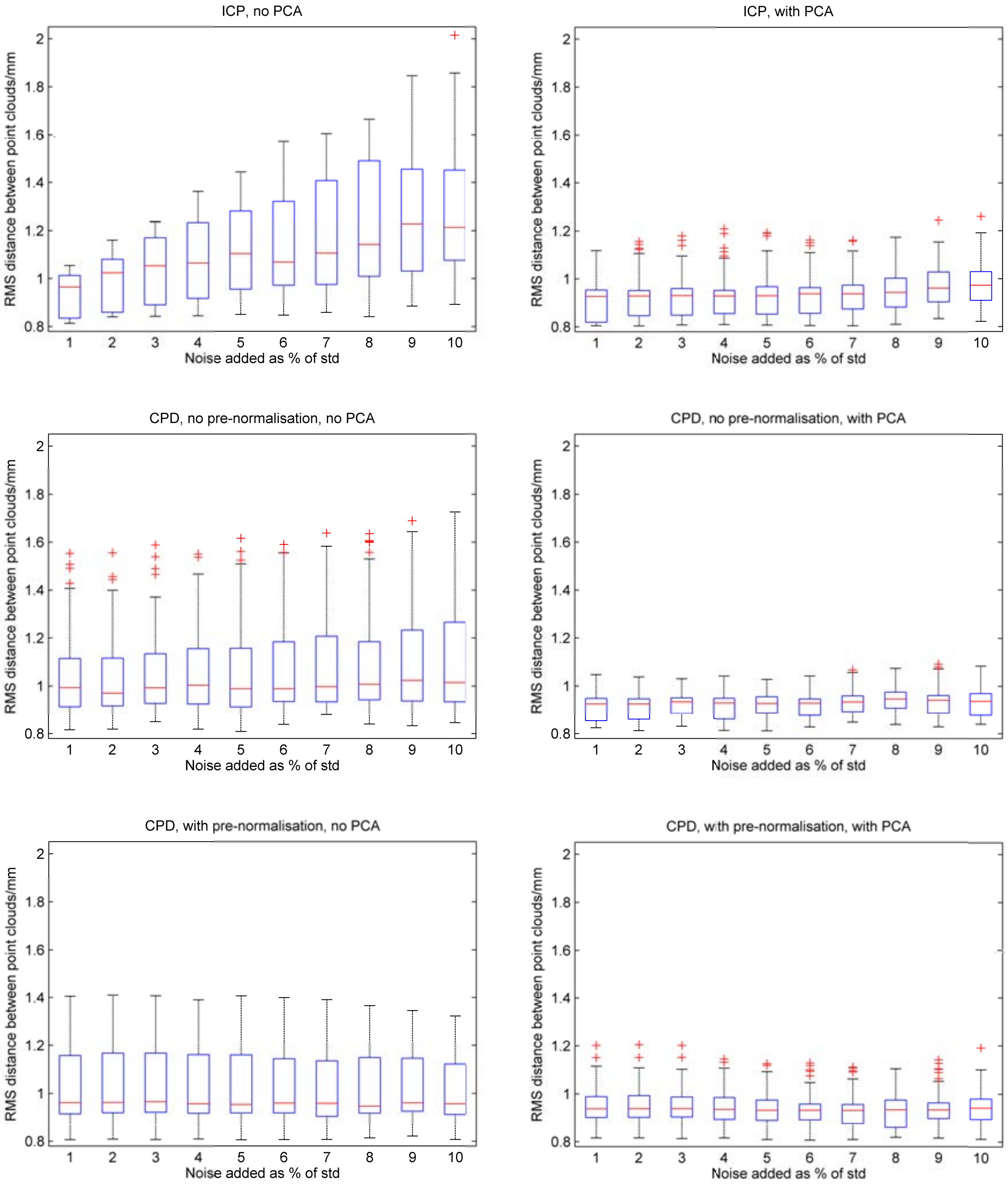

FIGURE 5.4: Variation of RMS error between point clouds with percentage of noise added after registration of transformed ground truth to noisy, re-meshed point clouds. Registration methods used were (top-bottom) ICP, CPD1, and CPD2; without (left side) and with (right side) initial alignment using PCA.

The resulting data was again tested for normality using the Shapiro-Wilk test in R. The data was found not to differ significantly from the normal distribution ($p \geq 0.01$) in the majority of cases. As Bartlett's test for homogeneity of variances rejected the assumption of homoscedasticity ($p < 2.2 \times 10^{-16}$), the non-parametric Kruskal-Wallis one-way analysis of variance was used.

Kruskal-Wallis tests showed significant effects on RMS distance after registration of (1) registration method ($p < 2.2 \times 10^{-16}$), (2) initial transformation ($p < 2.2 \times 10^{-16}$), (3) whether prealignment with PCA was used ($p < 2.2 \times 10^{-16}$), (4) amount of noise added ($p = 9.34 \times 10^{-7}$), and (5) which point cloud was used as the source ($p = 7.28 \times 10^{-10}$).

Post hoc testing was again performed using Dunn's test with the Benjamini-Hochberg adjustment to control the false discovery rate. Each possible value of the five variables listed above was compared with all possible combinations of values of the other four variables, with results as follows.

5.4.2.1 Registration methods

In all cases, significant differences between RMS distances when using different registration methods were seen only where the ground truth was used as the reference point cloud (Fig. 5.3) and never when it was the source (Fig. 5.4). This was largely due to the poorer performance of ICP and CPD1 in the latter case, in which CPD2 performed slightly better than in the former (see section 5.4.2.5 for discussion of the effect of registration direction).

ICP gave lower RMS values than CPD1 when prealignment was not used (0.889±0.049 mm across all noise levels and initial transformations for ICP, as compared with 0.948±0.120 mm for CPD1). The differences were largely not significant, other than for the largest initial transformation and higher levels of noise. When prealignment with PCA was used, no differences were significant (RMS distances were 0.889±0.049 mm for ICP and 0.913±0.058 mm for CPD1).

Where ICP was compared with CPD2, there were significant differences in RMS distance both with and without prealignment with PCA, for all initial transformations and for all noise levels. ICP always gave a lower value of RMS distance than CPD2, for which the mean RMS distances were 1.98±0.23 mm without prealignment and 1.58±0.21 mm with prealignment.

Where CPD1 and CPD2 were compared, there were significant differences in RMS distance in the majority of cases: the RMS distance was always lower for CPD1. The differences were greater for smaller initial transformation and noise level because these variables had more effect on CPD1 than on CPD2 or ICP. The poor results of CPD2 suggest that the algorithm is unable to escape any local minima it falls into. Possibly registration performance may by affected by the distortion of the point cloud due to pre-normalisation, as suggested in section 5.4.1.1.

5.4.2.2 Initial transformation

Initial transformation had no significant effect on RMS distance when ICP was used as the registration method. Where the ground truth was the source, there was a visible but not significant increase in RMS with greater initial transformation (Fig. 5.5).

Where CPD1 was used, significant differences in RMS distance were found between T1 and T4 for most noise levels, without prealignment, whether the ground truth was the source or the reference. RMS distance increased with larger initial transformation. The effect is reduced by prealignment, which leads to some reduction in RMS distance by providing a better starting position.

For CPD2, significant differences were seen only where the ground truth was the source, between T1 and T4 and between T2 and T4 for most noise levels, with and without prealignment using PCA. However, there was a difference in trend: where no prealignment was used, RMS distance increased with greater initial transformation, whereas where prealignment was used, the opposite was seen and RMS distance decreased with greater initial transformation. This reflects the results of section 5.4.1.2, again suggesting that ICP is less affected by initial transformation than CPD.

5.4.2.3 Prealignment with PCA

Although Kruskal-Wallis testing showed an effect of the use of prealignment on RMS distance ($p < 2.2 \times 10^{-16}$), post hoc testing showed no individual significant differences, as in section 5.4.1.3. In general, prealignment produces a lower RMS distance, except where ICP is used and the ground truth is the reference point cloud, where no difference is seen (0.889±0.049 mm without prealignment *v.* 0.888±0.049 mm with), perhaps because the best possible registration is achieved without the prealignment step.

5.4.2.4 Level of noise added

Although the level of noise added had some effect on the RMS distance after registration, a significant difference ($p = 4.01 \times 10^{-3}$) was only seen in a single case: between 1% and 10% noise when ICP was used without prealignment, for T4, with the ground truth as the source. Slight upwards trends in RMS distance with increased noise were seen in some cases: the most pronounced for ICP without prealignment, with the ground truth as the source (see section 5.4.2.5, below).

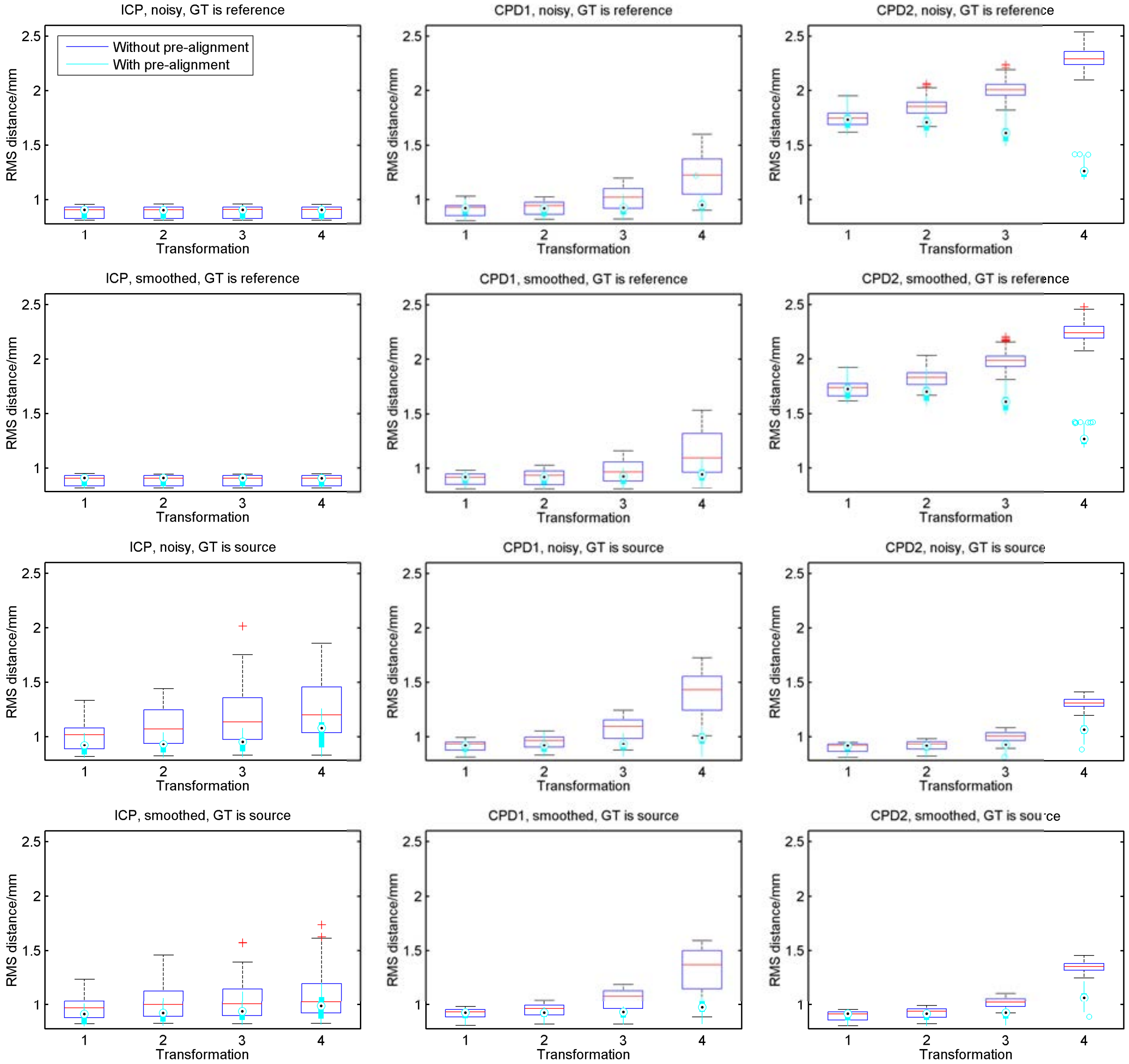

FIGURE 5.5: Effect of initial transformation for noisy and smoothed point clouds for (left-right) ICP, CPD1 and CPD2 registration and (top-bottom) noisy point cloud as source, smoothed point cloud as source, noisy point cloud as reference, smoothed point cloud as reference. The results without PCA are shown in blue and red; those with pre-alignment are shown in cyan.

5.4.2.5 Direction of registration

Which point cloud was used as the source had a significant effect in some cases. When ICP was used, without prealignment, a significant effect was seen for T2-4, at higher noise levels; the RMS distance was always lower when the noisy point cloud was the reference. When using prealignment with PCA, a significant difference was seen only for T4, 10% noise; again the RMS distance was lower with the noisy point cloud as the reference. No significant effects were seen when CPD1 was used. Where CPD2 was used without prealignment, differences were seen for: T1-2, all noise levels; T3, higher noise levels (7-8%, 10%). Where prealignment was used, differences were seen for T1-3, for all noise levels. Unlike ICP, CPD2 performed better when the noisy point cloud was the source.

The lower accuracy for ICP where the noisy point cloud is the reference may be due to the manner in which the alignment of the algorithm is assessed during the iterative stage of the registration algorithm; the RMS distance is found by matching each point in the source point cloud to the nearest point in the reference point cloud. If the reference point cloud is noisy, only the points from the edge nearest to the source will be used, unless a prealignment step moves the source into the noisy volume. The algorithm could be altered to include all points from both clouds in calculating the distance between them, or the noisy cloud could be always used as the source and the resulting transformation inverted where necessary.

5.4.3 Effect of smoothed noise on registration accuracy

A smoothing filter can be applied to noisy point clouds. In order to determine whether this would improve accuracy, the registration process described in section 3.2 was repeated with smoothed versions (as described in section 5.3.1) in place of the noisy point clouds (Figs. 5.6 and 5.7).

5.4.3.1 Registration methods

The results for smoothed heads are largely similar to those for noisy heads (section 5.4.2.1). Significant differences between RMS distances after ICP registration and those after CPD1 registration were seen in the cases where the ground truth was the reference point cloud, prealignment with PCA was not used and the noise level was 9% (for T3-4) or 10% (all initial transformations); in these cases the RMS distances were higher when using CPD1. Significant differences were not seen where the ground truth was the source, largely due to the poorer performance of ICP in this case than when the ground truth was the reference.

On comparing RMS distances after ICP registration with those after registration with CPD2, where the ground truth was the reference point cloud, ICP gave significantly lower distances for all initial transformations, noise levels, and both with and without prealignment with PCA. Where the ground truth was the source point cloud, ICP performed better only when prealignment was not used, for 8% noise, and for T3-4, in other cases the differences were not significant. When the ground truth was the source ICP performed worse at higher noise levels than when it was the reference; CPD2 performed better at all noise levels.

Differences were seen between RMS distances after CPD1 and CPD2 registration only when the ground truth was the reference point cloud. When the noisy point cloud was the reference, CPD1 performed worse and CPD2 better, reducing the differences between them. Where prealignment with PCA was not used, differences where seen for 1-7% and 8% noise (T1-2) and for 1-8% noise (T3-4). When prealignment was used,

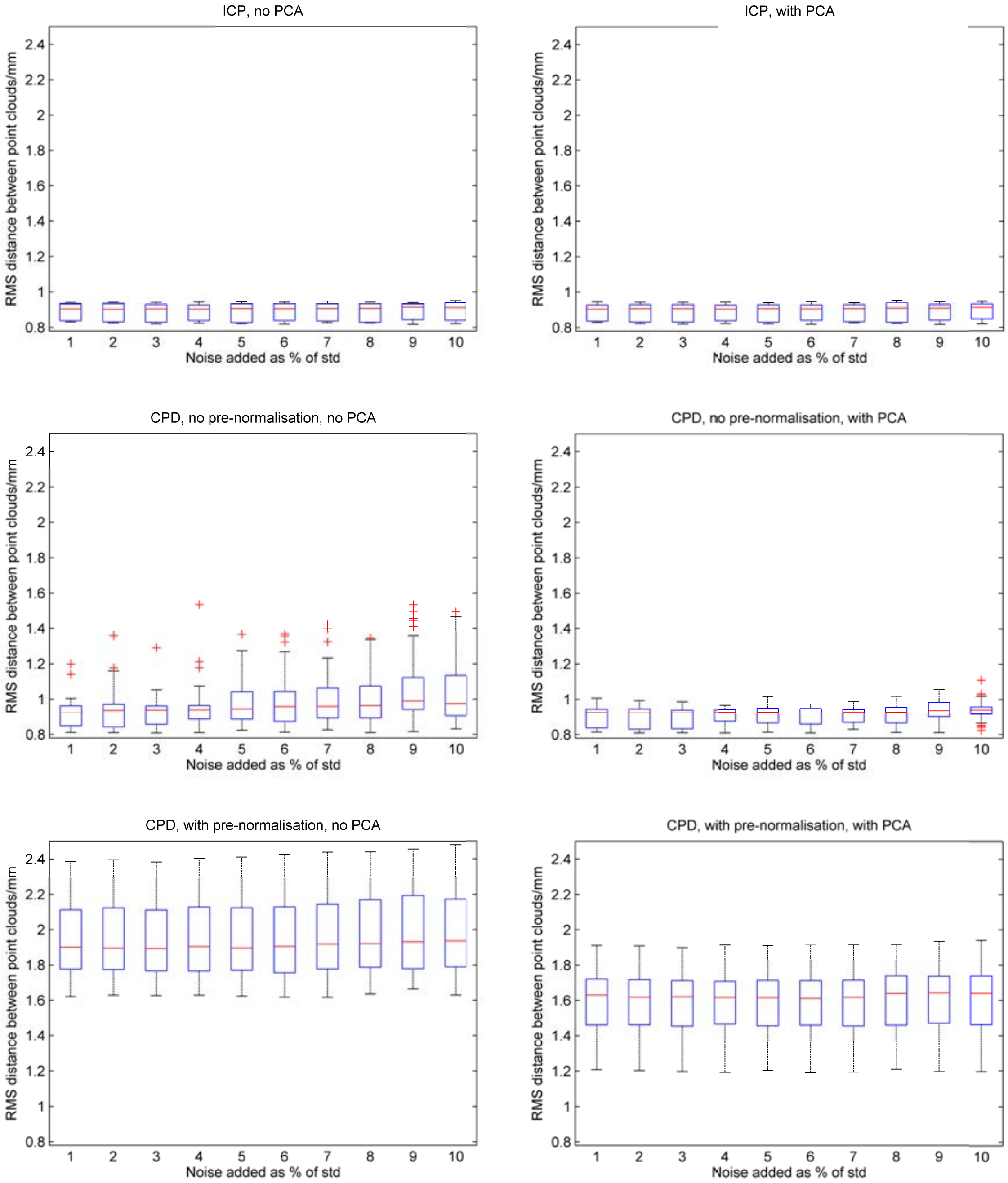

FIGURE 5.6: Variation of RMS error between point clouds with percentages of noise added and smoothed, after registration of smoothed remeshed point clouds to ground truth. Registration methods used were (top-bottom) ICP, CPD1, and CPD2; without (left side) and with (right side) initial alignment using PCA.

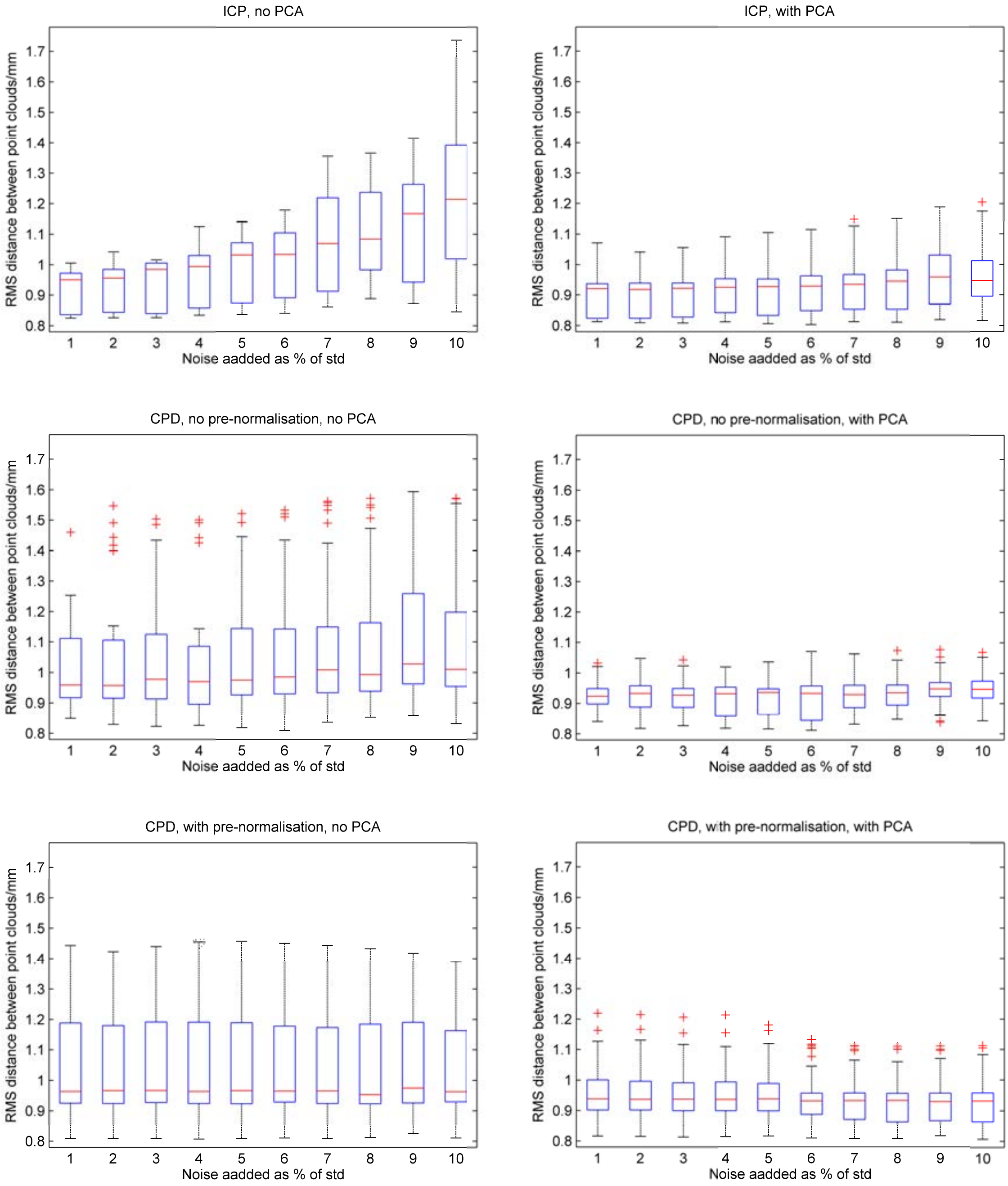

ICP, no PCA

ICP, with PCA

CPD, no pre-normalisation, no PCA

CPD, no pre-normalisation, with PCA

CPD, with pre-normalisation, no PCA

CPD, with pre-normalisation, with PCA

FIGURE 5.7: Variation of RMS error between point clouds with percentages of noise added and smoothed, after registration of transformed ground truth to smoothed re-meshed point clouds. Registration methods used were (top-bottom) ICP, CPD1, and CPD2; without (left side) and with (right side) initial alignment using PCA.

differences were seen for noise levels 1-9% (all transformations). In all cases where there was a difference, CPD2 gave the higher RMS distance.

5.4.3.2 Initial transformation

Initial transformation had a significant effect on RMS distance only where CPD2 was used, with PCA prealignment, the ground truth as the source point cloud and 8% noise (Fig. 5.5). In these cases T1-2 gave a significantly lower RMS distance than T3-4. The trends were very similar to those seen with noisy point clouds in section 5.4.2.2 and reflected those seen for the original point clouds in section 5.4.1.2.

5.4.3.3 Prealignment with PCA

As with noisy point clouds (section 5.4.2.3), prealignment with PCA had no significant effect on RMS distance, but the general trend was for it to improve registration accuracy.

5.4.3.4 Level of noise added

The level of noise added had a stronger effect on registration accuracy than when the noisy point clouds were not smoothed (section 5.4.2.4). Significant ($p < 0.01$) effects of noise level were only seen when the ground truth was used as the source and not when it was the reference (Fig. 5.8). In all cases where significant differences were seen, the higher noise level had the higher RMS distance. Where ICP was used, few comparisons between registrations using different noise levels showed significant differences. For CPD1 and CPD2, more comparisons showed significant differences, most commonly when one of the noise levels was in the region 8-10% and the other was lower.

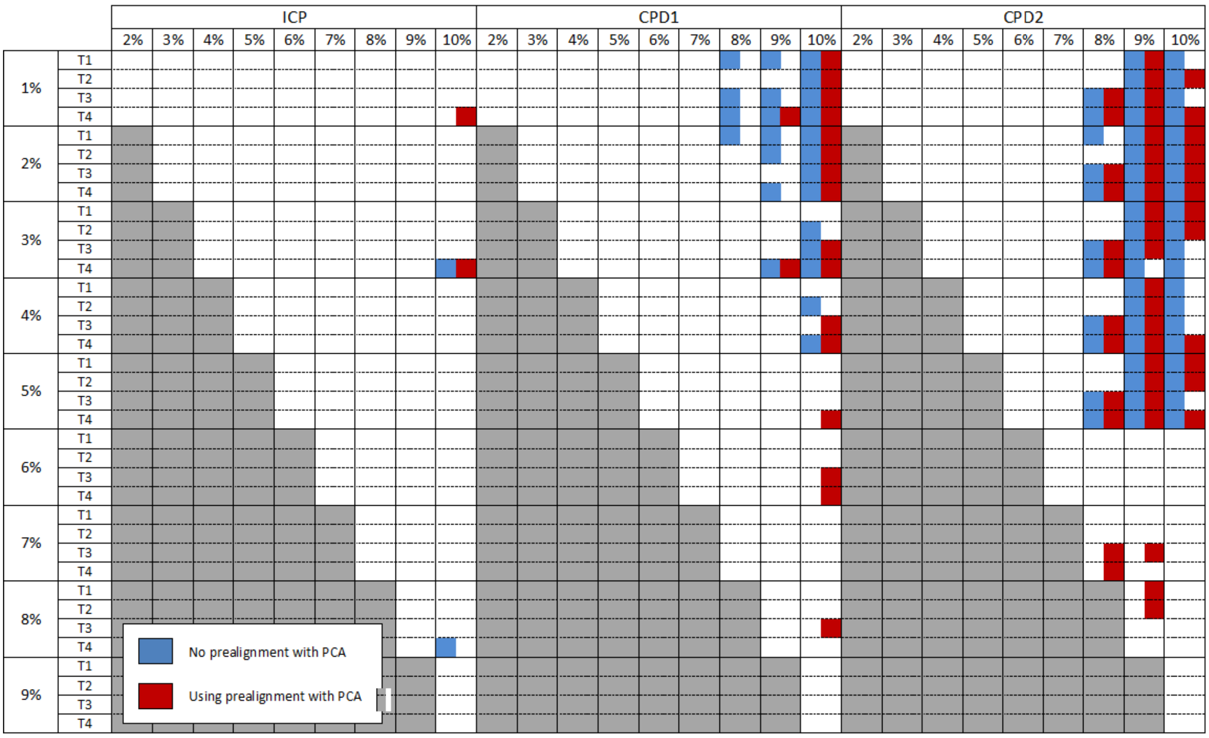

FIGURE 5.8: Significant differences between the RMS distances obtained for different noise levels, where other variables are kept constant, shown for each registration method (left-right: ICP, CPD1, CPD2). The blue and red squares show the comparisons that are significant and whether PCA prealignment was used; in each case the higher noise level was associated with with a higher RMS distance. The white squares show non-significant differences and the grey squares are not used. The ground truth is the source point cloud and the noisy point cloud is the reference (no significant differences were seen for the reverse). For each comparison, the lower noise level is shown along the left hand side and the higher along the top. The initial transformation is shown along the left hand side (T1-T4), and whether prealignment with PCA is used is shown by colour.

5.4.3.5 Direction of registration

When the effects of direction of registration (smoothed point cloud as source *v.* as reference) were investigated, similar effects were seen to the noisy case (section 5.4.2.5). When ICP registration was used, the direction of registration only made a significant difference when prealignment with PCA was not used. Significant differences between RMS distances after alignment in different directions were seen for: T2, 8% and 10% noise; T3, 10% noise; T4, 5%, 7% and 10% noise.

When CPD1 was used, no significant differences were seen on comparison of registrations in opposite directions. When CPD2 was used, far more significant differences were seen between registrations performed in opposite directions. When prealignment using PCA was not used, significant differences were seen for 1-5% noise, all initial transformations. When prealignment was used, differences were seen for 1-8% noise, T1-2, and for 1-7% noise for T3-4. In all cases, the RMS distance was higher when the ground truth was the reference than when it was the source.

5.4.4 Number of iterations required in registration process

For each registration performed, the ′final′ number of iterations at convergence and the ′best′ iteration with the best RMS distance were recorded. This was because in some cases the algorithm did not stop at the iteration with the lowest RMS distance. To ensure that the best transformation calculated by that algorithm was found, at each iteration the current RMS distance and transformation were saved. The transformation corresponding to the lowest (′best′) RMS distance was used to perform the final alignment.

5.4.4.1 Whole ROI registration

The ’best’ number of iterations at which the lowest RMS distance was obtained was recorded for each registration performed (Fig. 5.9), as well as the ’final’ iteration at which the algorithm stopped. When ICP or CPD2 were used, the best iteration number was always the number at which the algorithm stopped, so the best and final iteration number are identical, and the maximum number of iterations was never reached. When CPD1 was used, with or without prealignment, the maximum of 200 iterations was reached in 77 out of 80 trials, but in only three of these was it the best iteration, suggesting that the stopping criteria for this method were not sufficient.

Examination of the RMS distances at each iteration (Fig. 5.10) suggests that this occurs because the algorithm does not remain at the minimum RMS distance; in most cases the RMS distance increases after reaching a minimum. Where CPD2 is used, the RMS distance does not vary once a minimum is found and the algorithm stops more quickly.

Statistical tests were performed using the same methods as for the RMS distances (described in section 5.4.1). Significant effects ($p < 0.01$) of registration method on the best and final iteration number were seen ($p < 2.2 \times 10^{-16}$ for both), but not of initial transformation ($p = 0.0132$ for best, $p = 0.343$ for final) or whether prealignment was used ($p = 0.0107$ for best, $p = 0.153$ for final).

Post hoc testing showed significant differences in the best iteration number between ICP and CPD1 when T1 and T2 were used without PCA prealignment and when T4 was used with prealignment; in these cases ICP required more iterations than CPD1 (ICP showed a clear, though not significant, increase in best iteration number with larger initial transformation). In contrast, the final iteration reached was always more

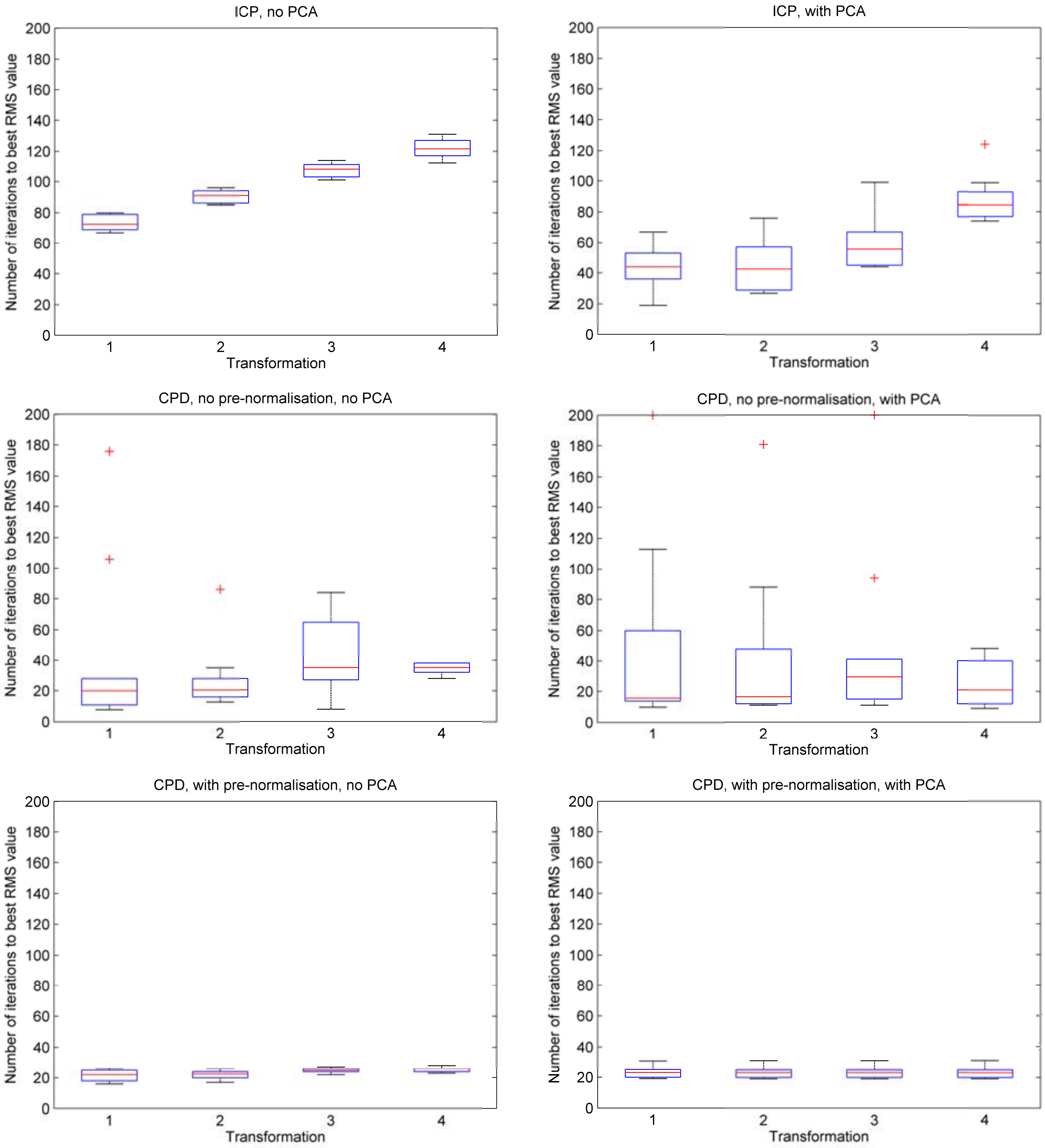

FIGURE 5.9: Iteration with best RMS error between point clouds after registration with (top-bottom) ICP, CPD1, and CPD2, for four different initial transformations, without (left side) and with (right side) initial alignment using PCA. Corresponds to Fig. 5.2.

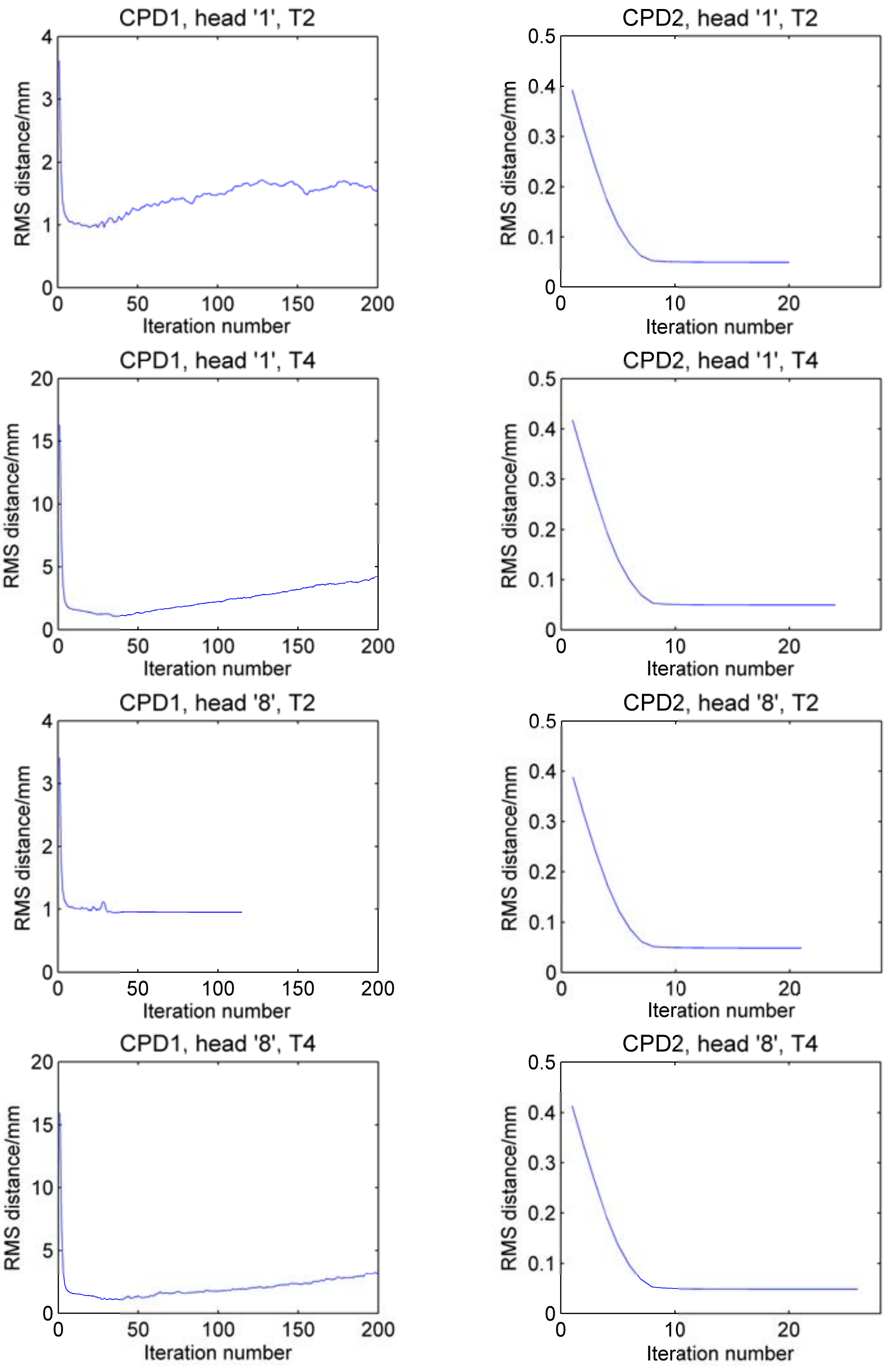

FIGURE 5.10: RMS distance at each iteration number for CPD1 (left) and CPD2 (right). Heads ’1’ and ’8’ are used, for initial transformations T2 and T4. Prealignment with PCA was not used. Head ’8’, T2, is one of the few cases where CPD1 stopped before reaching the maximum iteration number.

for CPD1, significantly so for T1-3, when prealignment was used. Significant differences were seen between best iteration numbers for ICP and CPD2 for all initial transformations where prealignment was not used and for T4 when it was used; ICP required more iterations. Similarly, the final iteration number for ICP was significantly greater than for CPD2, when no prealignment was used, T2-4 and when prealignment was used, T4 only. No significant differences were seen in best iteration number between CPD1 and CPD2, whereas the final iteration number was always significantly greater for CPD1.

The mean 'best' number of iterations used in ICP without prealignment increased from 73.2±4.8 for T1 to 122±7 for T4; where prealignment was used the increase was from 43.9±15.6 for T1 to 88.0±15.3 for T4. For CPD1 without prealignment, the minimum number was 27.7±21.5 for T2 and the maximum was 54.0±55.8 for T3; the maximum of 200 iterations was reached once (2.5% of the total number of trials). With prealignment, the lowest number of iterations used was 25.3±14.8 for T4 and the highest was 48.6±58.5 for T3. The maximum of 200 iterations was reached twice (5% of the total). Where CPD2 was used, the best RMS distance was at iteration 23.5±3.4 across all initial transformations and uses of prealignment; the maximum of 200 iterations was not reached.

5.4.4.2 Registration of smoothed and noisy point clouds

'Best' and 'final' iteration numbers were recorded for each registration performed on noisy and smoothed point clouds (Figs. 5.11 and 5.12), as described in sections 5.4.2 and 5.4.3. Registration method, initial transformation, whether pre-alignment was used, level of noise added and direction of registration all had significant ($p \leq 1.42 \times 10^{-10}$) effects on the number of best and final iterations used for noisy and smoothed registrations, except for the effect of noise level on final iteration number for the smoothed case ($p = 3.26 \times 10^{-2}$). Post hoc testing was not performed because of the small sample size.

Again, there was no difference between the best and final iteration number for ICP and CPD2. Where registration with CPD1 was performed, the final iteration number was the maximum of 200 in 1052 cases out of 1600, whereas the best iteration number was 200 in only 13 cases.

CPD2 required the fewest iterations (12.2±0.4 across both noisy and smoothed), irrespective of other factors. ICP shows trends of requiring fewer iterations where prealignment is used, a higher number of iterations used with larger initial transformation, and (where the ground truth was the reference) fewer iterations with increased noise level. Noisy and smoothed results are largely similar. CPD1 results for 'best' iteration numbers showed no clear trends; a larger sample size might provide a clearer picture.

5.4.5 Comparison of times taken to perform registration

In order to compare the times taken to do different types of registration, some of the registration processes were repeated at a time when no other program was running on the machine (PC specifications: Intel core i7-3770 CPU @ 3.4 GHz, 3401 Mhz, 4 cores, 8 logical processors, with 16 GB of RAM, NVIDIA GeForce GT 610, and a Windows 7 64-bit environment).

5.4.5.1 Whole ROI registration

The times taken to complete each registration were recorded (Fig. 5.13). Kruskal-Wallis testing showed that the registration method had a significant effect on the time taken

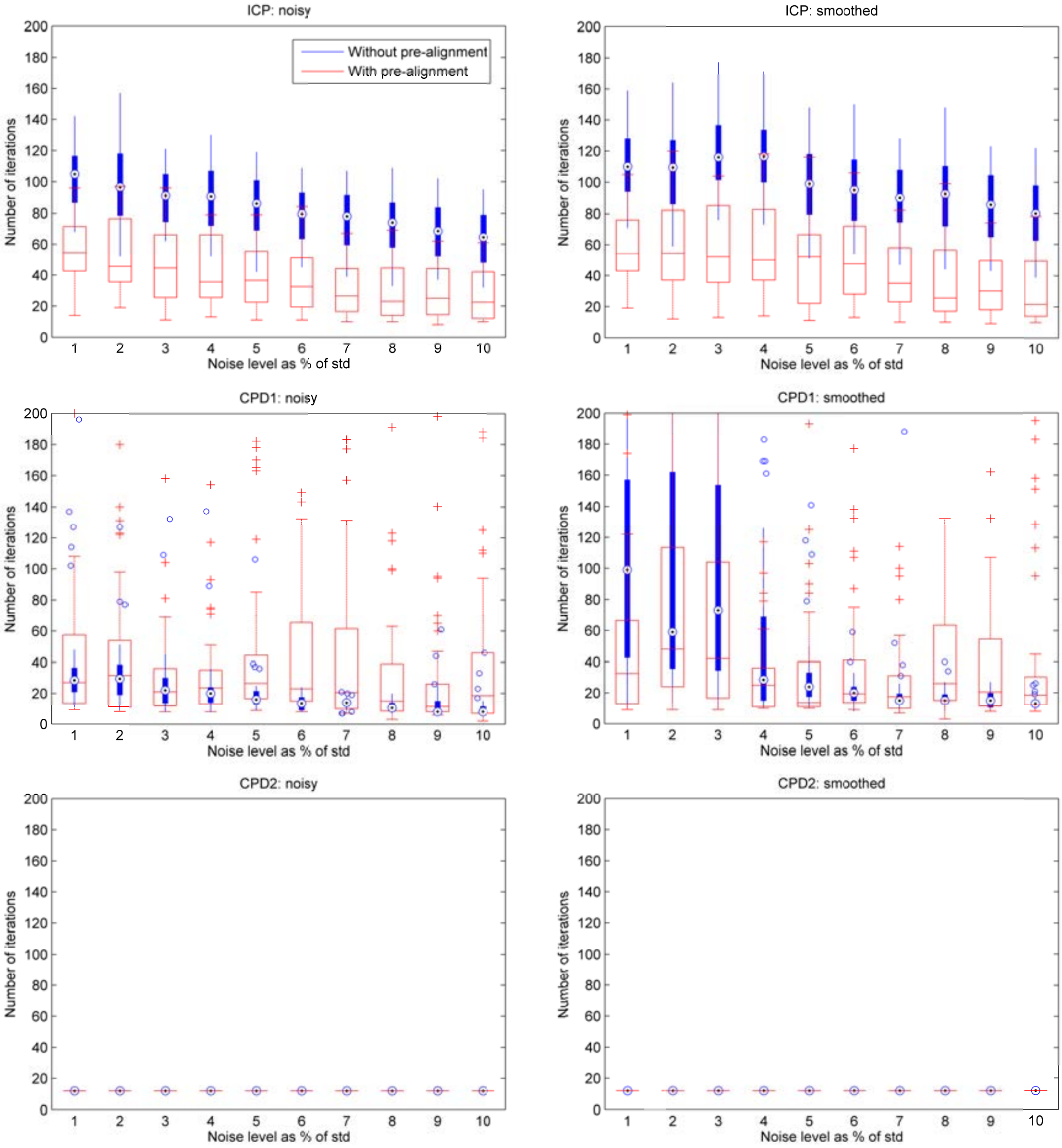

FIGURE 5.11: Number of iterations used in registration of (left) noisy and (right) smoothed point clouds, using the ground truth as the reference point cloud, without (blue) and with (red) prealignment using PCA. Registration techniques are (top) ICP, (middle) CPD1, and (bottom) CPD2.

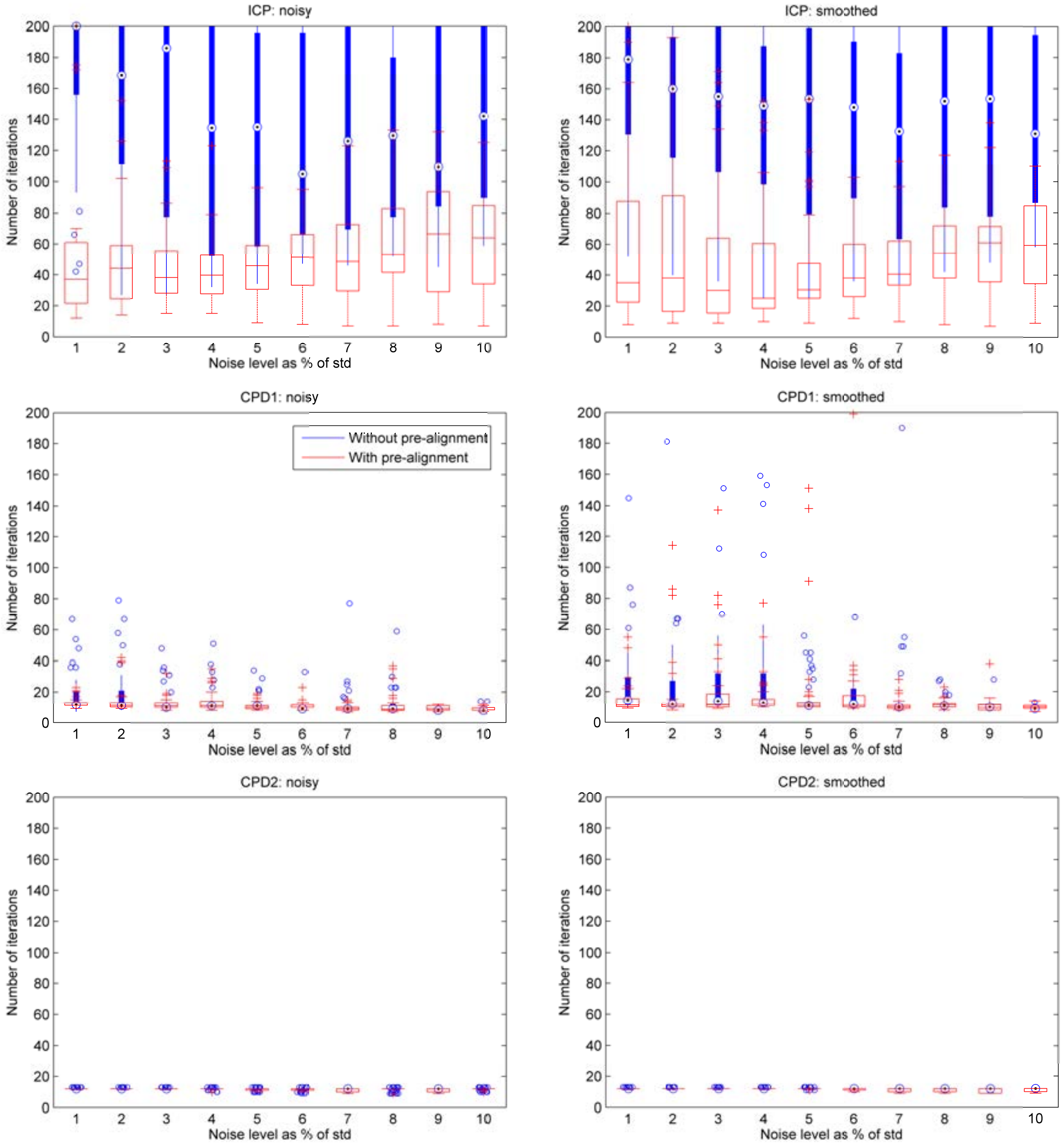

FIGURE 5.12: Number of iterations used in registration of (left) noisy and (right) smoothed point clouds, using the ground truth as the source point cloud, without (blue) and with (red) prealignment using PCA. Registration techniques are (top) ICP, (middle) CPD1, and (bottom) CPD2.

for the algorithm to run to completion ($p < 2.2 \times 10^{-16}$), but the initial transformation ($p = 0.588$) and whether prealignment was used ($p = 0.922$) did not.

Post hoc testing showed significant differences in times taken between the ICP and CPD1 methods when prealignment with PCA was used, for transformations T1-3. The mean time taken for ICP was 342±131 s and for CPD1 it was 1012±400 s. Where CPD2 was used the mean time taken was 94.1±16.8 s. Differences between ICP and CPD2 were seen where prealignment was not used for T2-4. The times taken for CPD1 were all significantly longer than the corresponding times for CPD2.

5.4.5.2 Noisy and smoothed registration

The processes for registration of noisy and smoothed heads described in sections 5.4.2 and 5.4.3 were repeated for a single head ('1') only. Registration was performed with the noisy head as the source and the reference; the same was done for the smoothed head (Fig. 5.14).

Kruskal-Wallis testing was performed as before to determine the overall effects of variance on time taken. For the noisy head, there were significant effects of registration method ($p < 2.2 \times 10^{-16}$), initial transformation ($p = 2.17 \times 10^{-3}$), whether prealignment was used ($p = 6.86 \times 10^{-4}$), and direction of registration ($p = 7.56 \times 10^{-6}$), but not of noise level ($p = 0.112$). For the smoothed head, there were significant effects of registration method ($p < 2.2 \times 10^{-16}$), initial transformation ($p = 4.52 \times 10^{-3}$), and direction of registration ($p = 2.41 \times 10^{-4}$), but not of whether pre-alignment was used ($p = 2.82 \times 10^{-2}$) or noise level ($p = 0.966$). Too few comparisons were available for post hoc testing to be meaningful. There was little difference in time taken between the noisy and smoothed cases.

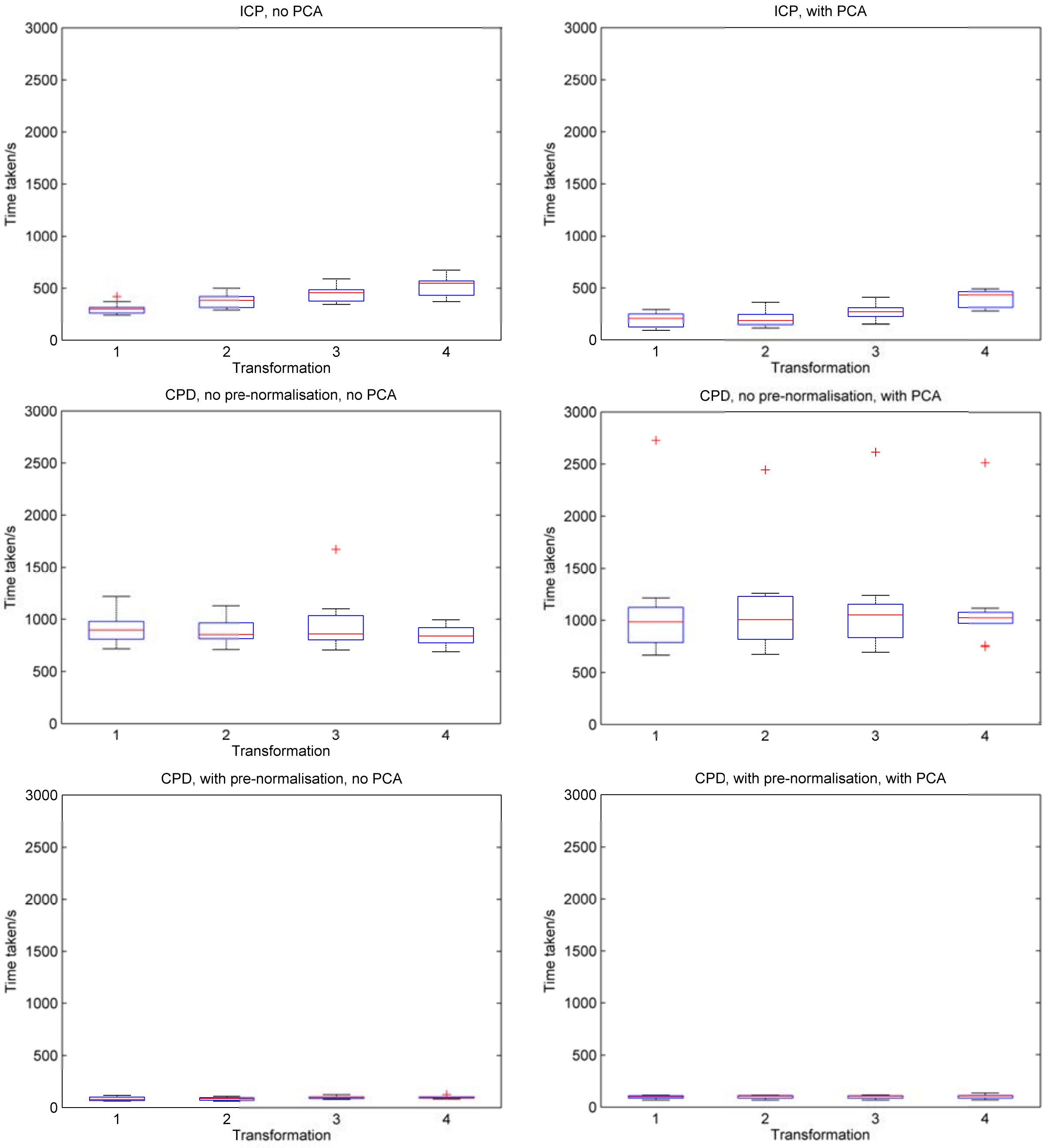

FIGURE 5.13: Times taken to complete registration with (top-bottom) ICP, CPD1, and CPD2, for four different initial transformations, without (left side) and with (right side) initial alignment using PCA. Corresponds to Figs. 5.2 and 5.9.

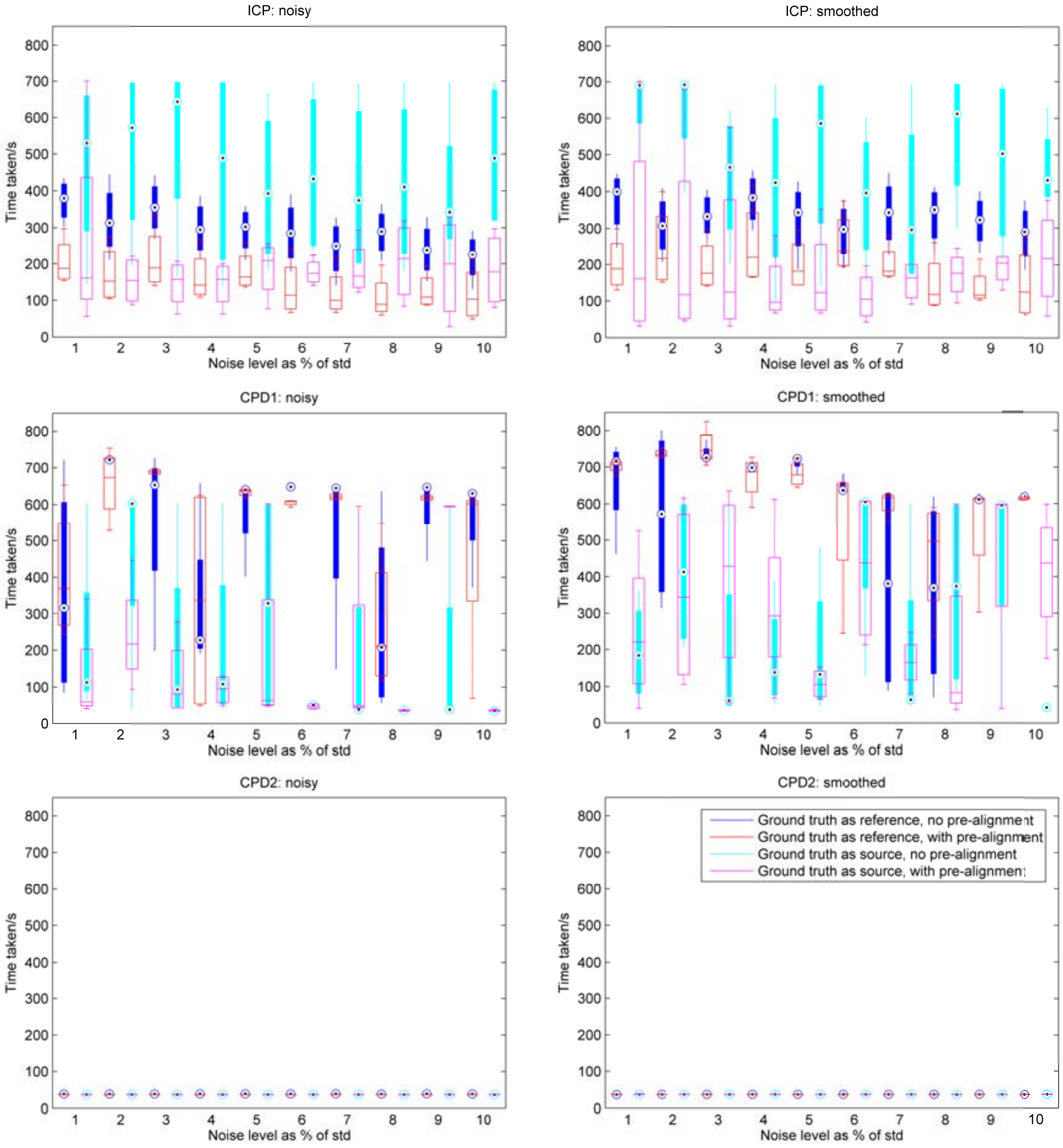

FIGURE 5.14: Times taken to complete noisy/smoothed (left/right) registration with (top-bottom) ICP, CPD1, and CPD2, without and with initial alignment using PCA, for different levels of noise/smoothed noise.

In all cases the registration process was quickest using CPD2, corresponding to it requiring the fewest iterations (see section 5.4.4.2). The mean time taken was 37.8±1.28 s across the noisy and smoothed cases, as compared to 286±181 s for ICP and 402±270 s for CPD1. The algorithms were timed to the stopping point, so CPD1 times were affected by the failure of the algorithm to stop at the best RMS distance. Where initial transformation made a difference, the general trend was for greater initial transformation to lead to greater registration time. Where prealignment with PCA made a difference, it reduced the time taken (primarily for ICP). For ICP, without prealignment, the time taken was generally less when the ground truth was the reference than when it was the source. CPD1, the time taken was generally less when the ground truth was the source, irrespective of other differences.

CPD2 is consistently a much faster registration method for these point clouds than ICP or CPD1, however it is also less accurate. ICP performs more quickly where PCA prealignment is used. CPD1 performs more quickly when the noisy or smoothed point is used as the reference rather than the source, although this trend is less clear. In both cases, improvements in speed would be beneficial for use in a clinical setting.

5.5 Registration of other point clouds

The results given here are not consistent with those described in Myronenko and Song [47], in that CPD does not outperform ICP for noisy point clouds. This may be due to the shape of the point clouds used. In Myronenko and Song [47], several different point clouds are used to test the registration algorithms and are provided with the software. The units of length for the point cloud coordinates are unknown, so they are referred to here as ’units’. In order to investigate whether point cloud shape has an effect, three point clouds from Myronenko and Song [47] are tested with the same initial transformations and added noise as the ROI surface point clouds.

5.5.1 Rabbit

This point cloud consists of 35,947 points (Fig. 5.15). When the four transformations previously described (see section 4.4.3) were applied to the point cloud, and it was registered back to itself, CPD1 (mean RMS distance of 0.0043±0.0063 units) performed better than ICP (0.0143±0.0105 units). CPD2 performed much worse and was more affected by the size of the initial transformation (0.798±1.090 units).

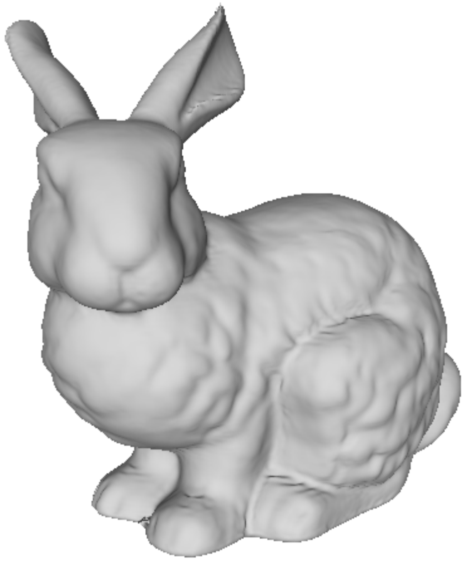

FIGURE 5.15: Rabbit point cloud, meshed.

Where noise was added to the rabbit point cloud, as described in section 5.3.1, the mean RMS distance (Fig. 5.16) between point clouds after registration with ICP was 0.0097±0.0019 units and there was no significant difference in RMS with noise level ($p = 0.0709$). Where CPD1 was used, there was again no significant difference between

RMS distances at different noise levels ($p = 0.0181$) and the mean distance between registered point clouds was 0.0085±0.0188 units. The RMS distance for CPD1 was significantly better than for ICP, whereas for CPD2 the mean RMS distance was significantly greater than for both ICP and CPD1 (13.5±10.6 units, $p = 2.51 \times 10^{-19}$).

Where prealignment with PCA was used (Fig. 5.16), ICP gave a mean RMS distance between point clouds of 0.0138±0.0011 units; there was no significant difference with noise level ($p = 0.0187$). This is significantly higher than where prealignment was not used ($p = 3.03 \times 10^{-12}$). Where CPD1 was used, there was again no difference between the RMS distances at different noise levels ($p = 0.142$), with a mean distance of 0.0170±0.0067 units. This was again significantly higher than without using PCA prealignment ($p = 1.43 \times 10^{-9}$). Where CPD2 was used the mean distance was 5.65±6.06 units, with no significant difference between noise levels ($p = 0.965$). In this case the mean distance was significantly lower than without prealignment ($p = 7.36 \times 10^{-5}$). The RMS distance for CPD1 was significantly higher than for the other two methods ($p = 3.19 \times 10^{-18}$).

5.5.2 Face

The face point cloud has 392 points (Fig. 5.17). For the face point cloud, there were significant differences between the RMS distances (Fig. 5.16) at different noise levels for both ICP ($p = 1.34 \times 10^{-5}$) and CPD ($p = 6.07 \times 10^{-5}$). ICP produced a minimum RMS error of 0.204±0.001 units at 1% noise and a maximum of 0.664±0.001 units at 7% noise. CPD1 produced a minimum RMS error of 0.153±0.003 units at 1% noise and a maximum of 2.66±2.19 units at 8% noise. Where CPD2 was used there was no significantly difference between noise levels ($p = 0.956$); the mean RMS distance was

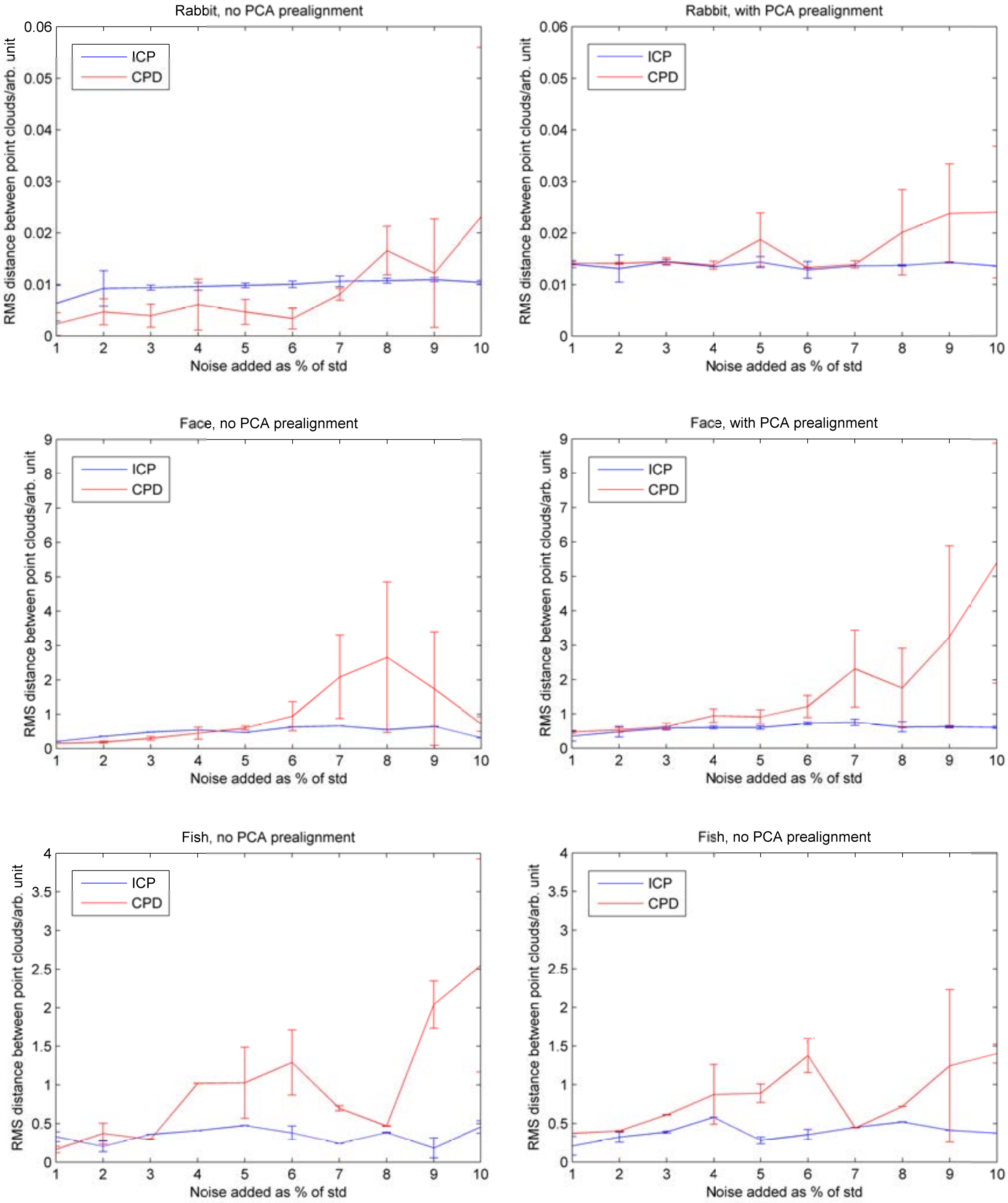

FIGURE 5.16: Comparison of RMS distances after registering (top-bottom) rabbit, face and fish noisy point clouds from four transformations, using ICP (blue) and CPD1 (red), without (left) and with (right) prealignment with PCA.

12.3±10.2 units, which is significantly higher ($p = 2.66 \times 10^{-17}$) than the values for ICP and CPD1.

Where prealignment with PCA was used there was some variation in RMS distance (Fig. 5.16) with noise level ($p = 0.00345$). The lowest RMS distance was 0.354±0.145 units, which is significantly lower than the RMS distances for 7% (0.755±0.085 units) and 6% noise. This is significantly higher ($p = 1.14 \times 10^{-3}$) than the RMS distance without prealignment. Where CPD1 was used, mean RMS distance tended to increase with noise level, with the RMS distance at 1% (0.0473±0.042 units) significantly less than at 10% ($p = 8.29 \times 10^{-4}$, 5.39±3.49 units). Where CPD2 was used, the mean RMS distance was 4.20±5.18 units, with no significant variation with noise level ($p = 0.960$). This is significantly lower than where prealignment was not used ($p = 4.23 \times 10^{-6}$), but significantly higher than the values for ICP and CPD1 ($p = 1.12 \times 10^{-5}$).

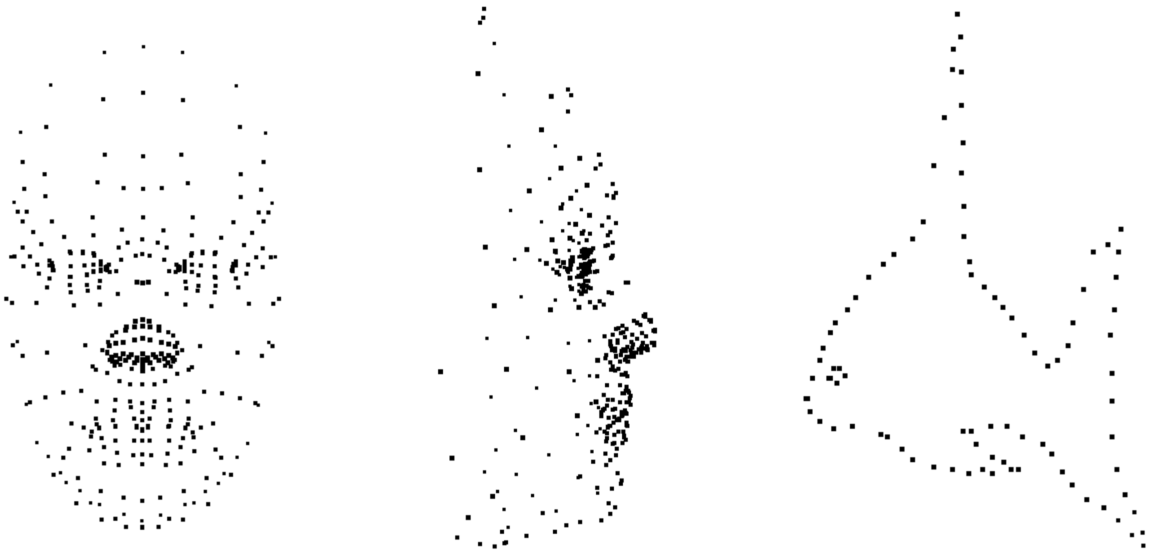

FIGURE 5.17: (Left-right) Face point cloud from front and in profile, fish point cloud (2D).

5.5.3 Fish

The fish point cloud has 91 points and is 2D; it is treated here as a 3D point cloud where all the points have $z = 0$ (Fig. 5.17). For the fish point cloud, there were again significant differences between the RMS distances (Fig. 5.16) at different noise levels for both ICP ($p = 8.28 \times 10^{-4}$) and CPD1 ($p = 7.30 \times 10^{-5}$). ICP produced a minimum RMS error of 0.183±0.129 units at 9% noise and a maximum of 0.475±0.000 units at 5% noise. CPD1 produced a minimum RMS error of 0.164±0.003 units at 1% noise and a maximum of 2.55±1.38 units at 10% noise. Where CPD2 was used there was no variation in RMS distance with level of noise ($p = 0.937$), with a mean RMS distance of 11.8±9.8 units. This is significantly higher than for CPD1 and both are significantly higher than ICP ($p = 6.91 \times 10^{-19}$).

Where prealignment with PCA was used, there were again significant differences between the RMS distances (Fig. 5.16) at different noise levels for both ICP ($p = 1.88 \times 10^{-4}$) and CPD ($p = 8.63 \times 10^{-4}$). For ICP, the RMS distances for 1% (0.209±0.122 units) and 5% were significantly lower than for 4% (0.579±0.000 units) and 8%. For CPD1, the RMS distance for 1% (0.371±0.000 units) was significantly less than for 6% and 10%. The distance for 10% (1.40±0.124 units) was also significantly more than for 2%. The distances are not significantly different to those where prealignment was not used ($p = 0.0690$ for ICP; $p = 0.946$ for CPD1). Where CPD2 was used there was no significant difference with the level of noise ($p = 0.965$), with a mean RMS distance of 4.88±5.94 units. This is significantly higher than when prealignment was not used ($p = 6.51 \times 10^{-5}$). Again, the result for CPD2 with prealignment is significantly higher than for CPD1 and both are significantly higher than ICP ($p = 2.07 \times 10^{-12}$).

5.5.4 Comparison

CPD2 produces significantly higher RMS distances than ICP and CPD1 in all cases. Overall there is more variation in RMS error with noise level for CPD1 than for ICP. CPD1 is more likely to do better than ICP at lower noise levels than at higher (Fig. 5.16). For the rabbit point cloud, CPD1 performed better than ICP at lower noise levels where prealignment was not used. This may be because the rabbit point cloud was denser and had more features than the other point clouds, although it is not clear why prealignment with PCA should have lead to poorer CPD1 performance. Prealignment with PCA did not improve overall registration accuracy. These results suggest that the poorer performance of CPD1 for noisy point clouds, as compared with ICP, was not solely due to the lack of features in the ROI point clouds taken from MRI data. These results may differ from Myronenko and Song [47] because a different form of ICP (Levenberg-Marquardt ICP [120]) is used in their work.

5.6 Discussion

ICP accuracy was unaffected by initial transformation (of up to $\frac{\pi}{5}$ radians rotation). Where the noisy or smoothed point cloud was the source, accuracy was also unaffected by noise level: an RMS distance of 0.889±0.049 mm all noise levels was achieved. When the noisy or smoothed point cloud is used as the reference point cloud, the RMS distance between aligned point clouds increases with the level of noise added. This may occur because the RMS distance between point clouds is calculated from the source points to their nearest neighbours in the reference cloud, which would align the source with the nearest edge of the reference. The algorithm may perform well with higher levels of noise because the noise is evenly distributed about the surface.

RMS distances for CPD1 were similar to or higher than those for ICP; the differences were only significant at higher initial transformations and noise levels. RMS distances increased with greater initial transformation, suggesting that CPD is more affected by initial global alignment than ICP. Although no significant differences were seen, use of PCA to some extent decreased RMS distances, higher noise levels increased RMS distances and CPD1 performed better when the noisy point cloud was the source.

CPD2 achieved significantly higher RMS distances than ICP in all registrations, with and without added noise and smoothed noise. RMS distance were affected by initial transformation, although not always significantly; RMS distances increased with larger initial transformation, except where the ground truth was the reference and prealignment with PCA was used, when RMS distance decreased with larger initial transformation. The level of noise added made no significant difference. Prealignment reduced RMS distance, although not significantly, and lower RMS distances were achieved when the ground truth was the source. The poor performance of CPD2 may suggest that the algorithm does not move far enough at each iteration of the registration process to escape local minima and so does not find the global minimum. The process of reducing the point cloud to unit variance in each of the x, y, and z directions may affect registration accuracy by distorting the point cloud shape; the original head shape is longer along the x-axis (front to back) than the y-axis (side to side). Normalisation would make these lengths similar, increasing rotational symmetry, and thus make it harder to find the correct alignment.

In most instances CPD has performed more poorly than ICP, the reverse of the results shown in Myronenko and Song [47]. Although this may be related to the smooth shape of the point cloud, when the algorithms were tried with other point clouds, CPD did not outperform ICP, particularly at higher noise levels. The results may be related to the use of a different variant of ICP. Other measures from Myronenko and Song [47], such as adding outliers or deleting part of the point cloud, have not been tried.

5.7 Conclusion

In this chapter, ICP has been shown to be generally more accurate than CPD for the purposes of registering the ROI point clouds, giving a best RMS distance of 0.884 ± 0.050 mm between point clouds after alignment. ICP was more effective when the original point cloud was used as the reference and the re-meshed/noisy/smoothed point cloud as the source, but it should be possible to modify the algorithm to work equally well in both directions. ICP performance was not affected by adding Gaussian noise with a standard deviation of up to 10% of the standard deviation of the point cloud. However, the noise was distributed evenly about the surface; outliers could have a stronger effect on accuracy. Smoothing the noise using a Laplacian filter did not improve ICP registration accuracy, but did have some effect on CPD accuracy. ICP accuracy was not affected by initial rotation of up to $\frac{\pi}{5}$, whereas CPD accuracy was, suggesting that having a good initial global alignment may be less important for ICP than CPD.

As CPD performed less well than expected, in chapter 6 another probabilistic registration method, 3D Normal Distribution Transform, is investigated. So far registration accuracy has only been measured in terms of the RMS distance between point clouds, but in surgery the error at the target point within the head will be the important factor. In Chapter 7 the error at the target point based surface registration will be evaluated.

Chapter 6

3D Normal Distribution Transform Registration Algorithm

6.1 Introduction

A further registration method in which one point cloud is represented as a probability density function (PDF) is the 3D Normal Distribution Transform (3D-NDT) registration algorithm. Magnusson [37], and Ulaş and Temeltaş [121] suggest that the method may have advantages over ICP in terms of efficiency of data representation and the range of initial poses from which it can converge to a minimum, i.e. initial global registration is not so important as for ICP. The points of the second point cloud are treated as having been generated by the probability distribution of the first point cloud.

The method differs from Coherent Point Drift, both in the method of generation of a probability density function from a point cloud, and in the type of registration algorithm used. CPD is an expectation-maximisation algorithm, whereas 3D-NDT directly calculates updates to the pose (rotation and translation) of the source point cloud from the first and second derivatives (the gradient and the Hessian) of the score with respect to the components of the pose. In addition, the PDF is generated from the reference point cloud here, whereas it is generated from the source point cloud in CPD registration.

6.2 Normal distribution transform surface representation

Normal distribution transforms can be used to compactly represent a surface, by dividing it into cells and representing the contents of each cell as a local probability distribution. This allows the surface data to be stored as the parameters of the probability distribution within each cell. A normal distribution can be used, in which case the mean and variance are stored. This can also be combined with a uniform distribution, in which case coefficients are needed to give the relative amounts of normal and uniform distributions. Both 2D [122] [123] and 3D [37] surfaces can be represented in this fashion.

6.2.1 Division of point cloud into cells

A number of different strategies exist for dividing the point cloud space up into cells. The size of the cell is very important. Too large a cell will obscure local details and fail to fully represent the surface, while if the cells are small the points of the source point cloud are less likely to fall within their region of influence, unless the point clouds are initially closely aligned [37]. Small cells are likely to exclude more reference points from the probability density function and may not represent some parts of the scan, as a minimum of five points per cell are required for a local PDF, in order to reduce the likelihood of a singular covariance matrix.

If a fixed lattice of cells is used, the user must choose a suitable cell size for the shape and density of the reference point cloud. However, the method has the advantage of being computationally inexpensive.

A fixed lattice can be adapted to be more flexible by the use of an octree structure. The point cloud is initially divided in a fixed lattice structure and a maximum number of points per cell is chosen. Each cell with more than the maximum number of points is then divided into eight equal cells by halving the volume along each of the x, y, and z directions; the resulting cells are similarly subdivided into eight if they contain more than the maximum number of points and the process is repeated until no cell exists which contains more than the maximum number of points. This allows smaller cells to be used in denser areas of the point cloud, better representing detailed structure, and larger cells to be used in less dense areas.

Magnusson [37] chooses to use a "linked cells" method. Instead of discarding source points which do not fall within a cell of the reference NDT, they can form part of the PDF of the closest occupied cell. Their contribution to the PDF will be weak, due to their distance from the centre of mass. The occupied cells of the NDT are stored in a kD tree search structure, which can be queried for the nearest cell when a source point falls outside the occupied cells.

Other options are iterative discretisation, in which runs are performed with successively finer cell resolution, and adaptive clustering, in which a clustering algorithm (e.g. k-means) is used to group the reference points as clusters, each of which is then used as a cell. Trilinear interpolation can be used to reduce discontinuities in the PDF at cell boundaries, either by using overlapping cells, or by using weighted contributions from neighbouring cells. This is more computationally expensive than using discrete cells. [37, 124, 122]

6.3 Registration algorithm

In the 3D-NDT algorithm, the reference point cloud, $\boldsymbol{Y} = (\boldsymbol{y}_1, \ldots, \boldsymbol{y}_M)^T$, is divided into cells and represented as a probability density function comprised of the PDFs of the individual cells. The PDFs of each cell are a combination of a normal distribution and a uniform distribution, as described in equation 6.4. The source point cloud, $\boldsymbol{X} = (\boldsymbol{x}_1, \ldots, \boldsymbol{x}_N)^T$, is treated as data drawn from the distribution. The following algorithm summary is based on Magnusson [37].

The pose is expressed as the parameter vector, $\boldsymbol{p} = [t_x, t_y, t_z, \phi_x, \phi_y, \phi_z]^T$, where the first three numbers express the translation and the second three express the angles of rotation about the three axes. The overall transformation of a point is then

$$T(\boldsymbol{p}, \boldsymbol{x}_n) = \boldsymbol{R}_x \boldsymbol{R}_y \boldsymbol{R}_z \boldsymbol{x}_n + \boldsymbol{t}, \tag{6.1}$$

where $\boldsymbol{R}_x(\phi_x) = \begin{pmatrix} 1 & 0 & 0 \\ 0 & \cos\phi_x & -\sin\phi_x \\ 0 & \sin\phi_x & \cos\phi_x \end{pmatrix}$, $\boldsymbol{R}_y(\phi_y) = \begin{pmatrix} \cos\phi_y & 0 & \sin\phi_y \\ 0 & 1 & 0 \\ -\sin\phi_y & 0 & \cos\phi_y \end{pmatrix}$,

$\boldsymbol{R}_z(\phi_z) = \begin{pmatrix} \cos\phi_z & -\sin\phi_z & 0 \\ \sin\phi_z & \cos\phi_z & 0 \\ 0 & 0 & 1 \end{pmatrix}$ and $\boldsymbol{t} = [t_x, t_y, t_z]^T$.

The complete transformation is therefore

$$T(\boldsymbol{p}, \boldsymbol{x}_n) = \begin{pmatrix} c_y c_z & -c_y s_z & s_y \\ c_x s_z + s_x s_y c_z & c_x c_z - s_x s_y s_z & -s_x c_y \\ s_x s_z - c_x s_y c_z & c_x s_y s_z + s_x c_z & c_x c_y \end{pmatrix} \boldsymbol{x}_n + \begin{pmatrix} t_x \\ t_y \\ t_z \end{pmatrix}, \tag{6.2}$$

where $c_i = \cos\phi_i$ and $s_i = \sin\phi_i$.

The algorithm works as follows:

Initialisation

- The space occupied by $\boldsymbol{Y}$ is split into a cell structure, $\boldsymbol{B}$. Each point $\boldsymbol{y}_m \in \boldsymbol{Y}$ is allocated to a cell, b_k.
- For each cell, b_k, the mean $\boldsymbol{\mu}_k$, and covariance matrix, $\boldsymbol{\Sigma}_k$, of the points in that cell are calculated. Since the inverse of the covariance matrix is required, a singular, or nearly singular, $\boldsymbol{\Sigma}$ would be problematic; as a precaution, if either of the two smaller eigenvalues, λ_1 and λ_2, is less than one hundredth of the largest eigenvalue, λ_3, it is increased to $\lambda_3/100$ and the new eigenvalue is denoted as λ_1' or λ_2'. The matrix $\boldsymbol{\Sigma}' = \mathrm{V}\boldsymbol{\Lambda}'\mathrm{V}$ replaces $\boldsymbol{\Sigma}$, where V contains the eigenvectors of $\boldsymbol{\Sigma}$ and

$$\boldsymbol{\Lambda}' = \begin{pmatrix} \lambda_1' & 0 & 0 \\ 0 & \lambda_2' & 0 \\ 0 & 0 & \lambda_3 \end{pmatrix}. \tag{6.3}$$

- The pose, $\boldsymbol{p}$, can be initialised as an initial guess, or a zero vector.

Registration (repeat until convergence)

- Set score, $\boldsymbol{s} = 0$; gradient, $\boldsymbol{g} = 0$ and Hessian, $\boldsymbol{H} = 0$.
- For each point $\boldsymbol{x}_n \in \boldsymbol{X}$:
  - Using the current pose, find the cell, b_k containing the point $T(\boldsymbol{p}, \boldsymbol{x}_n)$.
  - Update the score, s:

$$s = s - d_1 \exp\left(-\frac{d_2}{2}(\boldsymbol{x}_n - \boldsymbol{\mu}_k)^T \boldsymbol{\Sigma}_k^{-1}(\boldsymbol{x}_n - \boldsymbol{\mu}_k)\right), \tag{6.4}$$

where $d_3 = -log(c_2)$, $d_1 = -log(c_1 + c_2) - d_3$ and $d_2 = -2\log((-\log(c_1\exp(-\frac{1}{2}) + c_2) - d_3)/d_1)$. Constants c_1 and c_2 are chosen to weight the uniform and normal parts of the probability density function, such that the probability mass of the PDF equals one within the volume of a cell.

- Update the gradient, $\boldsymbol{g}$, for each entry, p_i, in the pose vector, $\boldsymbol{p}$:

$$g_i = \frac{\delta s}{\delta p_i} = \sum_{n=1}^{N} d_1 d_2 {\boldsymbol{x}'_n}^T {\boldsymbol{\Sigma}_k}^{-1} \frac{\delta \boldsymbol{x}'_n}{\delta p_i} \exp\left(\frac{-d_2}{2} {\boldsymbol{x}'_n}^T {\boldsymbol{\Sigma}_k}^{-1} \boldsymbol{x}'_n\right), \tag{6.5}$$

where $\boldsymbol{x}'_n \equiv T(\boldsymbol{p}, \boldsymbol{x}_n) - \boldsymbol{\mu_k}$.

- Update the Hessian matrix, $\boldsymbol{H}$, the entries H_{ij} of which are

$$H_{ij} = \frac{\delta^2 s}{\delta p_i \delta p_j} = \sum_{n=1}^{N} d_1 d_2 \exp\left(\frac{-d_2}{2} {\boldsymbol{x}'_n}^T {\boldsymbol{\Sigma}_k}^{-1} \boldsymbol{x}'_n\right)\left(-d_2\left({\boldsymbol{x}'_n}^T {\boldsymbol{\Sigma}_k}^{-1} \frac{\delta \boldsymbol{x}'_n}{\delta p_i}\right)\left({\boldsymbol{x}'_n}^T {\boldsymbol{\Sigma}_k}^{-1} \frac{\delta {\boldsymbol{x}'_n}^T}{\delta p_j}\right) + {\boldsymbol{x}'_n}^T {\boldsymbol{\Sigma}_k}^{-1} \frac{\delta^2 \boldsymbol{x}'_n}{\delta p_i \delta p_j} + \frac{\delta {\boldsymbol{x}'_n}^T}{\delta p_j} {\boldsymbol{\Sigma}_k}^{-1} \frac{\delta \boldsymbol{x}'_n}{\delta p_i}\right). \tag{6.6}$$

- Solve the equation

$$\boldsymbol{H}\Delta\boldsymbol{p} = -\boldsymbol{g}. \tag{6.7}$$

$\Delta\boldsymbol{p}$ is used to provide the update to the pose, $\boldsymbol{p}$. For the 2D case, the pose is calculated as $\boldsymbol{p} = \boldsymbol{p} + \Delta\boldsymbol{p}$, but the 3D algorithm requires additional constraints on the rotation axis. To control the step size for the update, the Moré-Thuente line search algorithm is used [125]. The algorithm converges when the maximum number of iterations is reached or the magnitude of $\Delta\boldsymbol{p}$ is less than the maximum transformation distance, ϵ. This can be chosen based on the geometry of the point clouds (a larger value would be reasonable for a larger point cloud); trial and error may be used to determine a suitable value.

The first-order derivative $\frac{\delta}{\delta p_i} T(\boldsymbol{p}, \boldsymbol{x}_n)$ of the transformation function corresponds to the i$^{\text{th}}$ column of the Jacobian matrix,

$$\boldsymbol{J}_E = \begin{pmatrix} 1 & 0 & 0 & 0 & c & f \\ 0 & 1 & 0 & a & d & g \\ 0 & 0 & 1 & b & e & h \end{pmatrix}, \tag{6.8}$$

where

$$\begin{aligned}
a &= x_1(-s_x s_z + c_x s_y c_z) + x_2(-s_x c_z - c_x s_y s_z) + x_3(-c_x c_y), \\
b &= x_1(c_x s_z + s_x s + y c_z) + x_2(-s_x s_y s_z + c_x c_z) + x_3(-s_x c_y), \\
c &= x_1(-s_y c_z) + x_2(-s_x s_y s_z + x_3(c_y), \\
d &= x_1(s_x c_y c_z) x_2(-s_x c_y s_z) + x_3(s_x s_y), \\
e &= x_1(-c_x c_y c_z) + x_2(c_x c_y s_z) + x_3(-c_x s_y), \\
f &= x_1(-c_y s_z) + x_2(-c_y c_z), \\
g &= x_1(c_x c_z - s_x s_y s_z) + x_2(-c_x s_z - s_x s_y c_z), \\
h &= x_1(s_x c_z + c_x s_y s_z) + x_2(c_x s_y c_z - s_x s_z).
\end{aligned}$$

The second order derivative $\frac{\delta^2}{\delta p_i \delta p_j} T(\boldsymbol{p}, \boldsymbol{x}_n)$ corresponds to element $\boldsymbol{H}_{ij}$ of the matrix

$$\boldsymbol{H}_E = \begin{pmatrix} \mathbf{0} & \mathbf{0} & \mathbf{0} & \mathbf{0} & \mathbf{0} & \mathbf{0} \\ \mathbf{0} & \mathbf{0} & \mathbf{0} & \mathbf{0} & \mathbf{0} & \mathbf{0} \\ \mathbf{0} & \mathbf{0} & \mathbf{0} & \mathbf{0} & \mathbf{0} & \mathbf{0} \\ \mathbf{0} & \mathbf{0} & \mathbf{0} & \boldsymbol{a} & \boldsymbol{b} & \boldsymbol{c} \\ \mathbf{0} & \mathbf{0} & \mathbf{0} & \boldsymbol{b} & \boldsymbol{d} & \boldsymbol{e} \\ \mathbf{0} & \mathbf{0} & \mathbf{0} & \boldsymbol{c} & \boldsymbol{e} & \boldsymbol{f} \end{pmatrix}, \tag{6.9}$$

where

$$\boldsymbol{a} = \begin{pmatrix} 0 \\ x_1(-c_x s_z - s_x s_y c_z) + x_2(-c_x c_z + s_x s_y s_z) + x_3(s_x c_y) \\ x_1(-s_x s_z + c_x s_y c_z) + x_2(-x_x s_y s_z - s_x c_z) + x_3(-c_x c_y) \end{pmatrix},$$

$$\boldsymbol{b} = \begin{pmatrix} 0 \\ x_1(c_x c_y c_z) + x_2(-c_x c_y s_z) + x_3(c_x s_y) \\ x_1(s_x c_y c_z) + x_2(-s_x c_y s_z) + x_3(s_x s_y) \end{pmatrix},$$

$$\boldsymbol{c} = \begin{pmatrix} 0 \\ x_1(-s_x c_z - c_x s_y s_z) + x_2(-s_x s_z - c_x s_y c_z) \\ x_1(c_x c_z - s_x s_y s_z) + x_2(-s_x s_y c_z - c_x s_z) \end{pmatrix},$$

$$\boldsymbol{d} = \begin{pmatrix} x_1(-c_y c_z) + x_2(c_y s_z) + x_3(-s_y) \\ x_1(-s_x s_y c_z) + x_2(s_x s_y s_z) + x_3(s_x c_y) \\ x_1(c_x s_y c_z) + x_2(-c_x s_y s_z) + x_3(-c_x c_y) \end{pmatrix},$$

$$\boldsymbol{e} = \begin{pmatrix} x_1(s_y s_z) + x_2(s_y c_z) \\ x_1(-s_x c_y s_z) + x_2(-s_x c_y c_z) \\ x_1(c_x c_y s_z) + x_2(c_x c_y c_z) \end{pmatrix},$$

$$\boldsymbol{f} = \begin{pmatrix} x_1(-c_y c_z) + x_2(c_y s_z) \\ x_1(-c_x s_z - s_x s_y c_z) + x_2(-c_x c_z + s_x s_y s_z) \\ x_1(-s_x s_z + c_x s_y c_z) + x_2(-c_x s_y s_z - s_x c_z) \end{pmatrix}.$$

In this implementation, if the absolute size of the angle ϕ_i is less than 1×10^{-4} radians then these trigonometric approximations are used: $\sin\phi_i = 0$, $\cos\phi_i = 1$.

6.4 Comparing 3D-NDT to ICP and CPD

The 3D-NDT registration algorithm was tested to compare the accuracy with that attained by ICP and CPD; an implementation in Point Cloud Library (PCL) software was used [126]. The linked cells method described above was used, with Newton's method for optimisation using Moré-Thuente line search to control the step size [125].

In the PCL implementation, the variables c_1 and c_2, which are used to calculate the score in equation 6.4, are defined as $c_1 = 10p_0$ and $c_2 = p_0/r^3$, where p_0 is the expected ratio of outliers and r is the resolution or voxel side length. Parameter values were chosen based on preliminary testing. The default value of $p_0 = 0.55$ was used and a resolution of $r = 9.0$ for the NDT grid structure (the default resolution is 1.0). A maximum step size for Moré-Thuente line search of 1, a maximum transformation difference of $\epsilon = 0.03$ for termination (default is 0.01) and a maximum of 100 iterations were used.

6.4.1 Whole head, four transformations

The experiment from section 5.4.1 was repeated using the 3D-NDT algorithm: each of the 10 re-meshed ROI point clouds was put through four transformations and registered to the corresponding initial ROI point cloud. Preliminary testing suggested that, as with ICP, an initial rotation of $\frac{\pi}{2}$ or more leads to a local minimum where one point cloud is upside down with respect to the other.

The 3D-NDT registration algorithm gave a mean RMS distance between aligned ROI point clouds of 0.882±0.052 mm over all heads and transformations, as compared with 0.884±0.048 mm for ICP (Fig. 6.1).

The data was compared with the equivalent data from chapter 5 for ICP, CPD1 and CPD2 registration. Kruskal-Wallis testing was used again as the data failed Barlett's test; a significance level of $p = 0.01$ was again used. A significant effect of registration method was seen ($p < 2.2 \times 10^{-16}$), but not of initial transformation ($p = 0.130$). Post hoc testing was done using Dunn's test, using Benjamini-Hochberg adjustments. CPD2 performed significantly worse than ICP and 3D-NDT for all initial transformations. CPD1 also performed worse than ICP and 3D-NDT for all initial transformations, but the difference was only significant for T4. Like ICP, 3D-NDT was not affected by the initial transformation.

6.4.2 Effect of noise on registration accuracy

The results of section 6.4.1 suggest that the 3D-NDT method produces similar registration accuracy to ICP. In order to determine whether the algorithm performs well on noisy point clouds, the process from section 5.3.1 was repeated to add noise to the re-meshed ROI point cloud. Noise was added for all re-meshed point clouds and for 10 different levels of noise, the point clouds were put through the same four transformations and registered.

Statistical testing was performed as above (section 6.4.1) to compare these results with the corresponding results (without prealignment) for ICP, CPD1, and CPD2. No significant effects were found of either initial transformation or whether the noisy point cloud was the source or the reference.

It was found that, where the noisy cloud was the source, the RMS distance for 3D-NDT increased from a mean of 0.883±0.052 mm for 1% noise, to 1.04±0.10 mm for 10% noise (Fig. 6.2). No significant difference was found in accuracy between 3D-NDT and ICP registration. 3D-NDT performed better than CPD1 for initial transformation

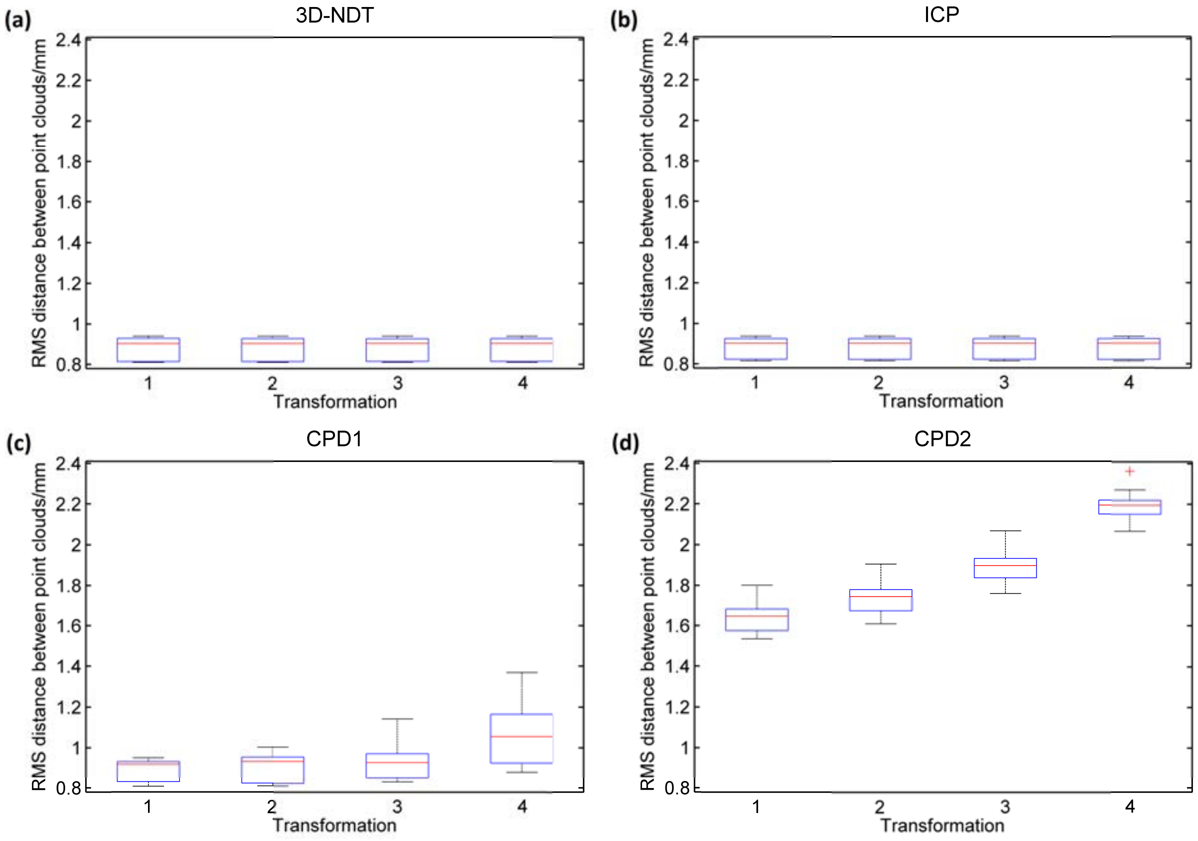

FIGURE 6.1: Comparison of RMS distances for (a-d) 3D-NDT, ICP, CPD1, and CPD2 algorithms, for four different initial transformations.

T4, noise levels 2-7% and better than CPD2 for T3, 1-9% noise and T4, 1-10% noise. The level of noise added had a significant effect on RMS accuracy for 3D-NDT for the following cases: T1, between 10% and 1-3% noise; T2 and T3, between 10% and 1-4% noise; and T4, between 1-2% and 9-10% noise. In each case the RMS distance was lower for lower noise levels.

Where the noisy point cloud was the reference (Fig. 6.3), the RMS distance for 3D-NDT was 0.899±0.066 mm for 1% noise, increasing to 1.04±0.19 mm for 10% noise. 3D-NDT achieved a lower RMS distance than ICP for initial transformation T3, 6-7% noise and for T4, 6-8% noise. It achieved a lower RMS distance than both CPD1 and CPD2 for T4, 1-8% noise. In this case, noise had no significant effect on RMS distance.

The results suggest that 3D-NDT performance decreases slightly with noise level. This leads to 3D-NDT performing slightly worse than ICP at higher noise levels when the noisy cloud is the source, but slightly better than ICP when the noisy cloud is the reference.

6.5 Conclusion

3D-NDT was found to achieve similar registration accuracy to ICP for the point clouds tested. Registration accuracy was not affected by the initial transformation of the source point cloud, although an initial rotation of $\frac{\pi}{2}$ or more can lead to a local minimum where the point clouds are opposite ways up. Where noisy point clouds were used, registration accuracy decreased slightly with increased noise level. This meant that performance was slightly worse than ICP at higher noise levels where the noisy point clouds were the source and slightly better where the noisy point clouds were the

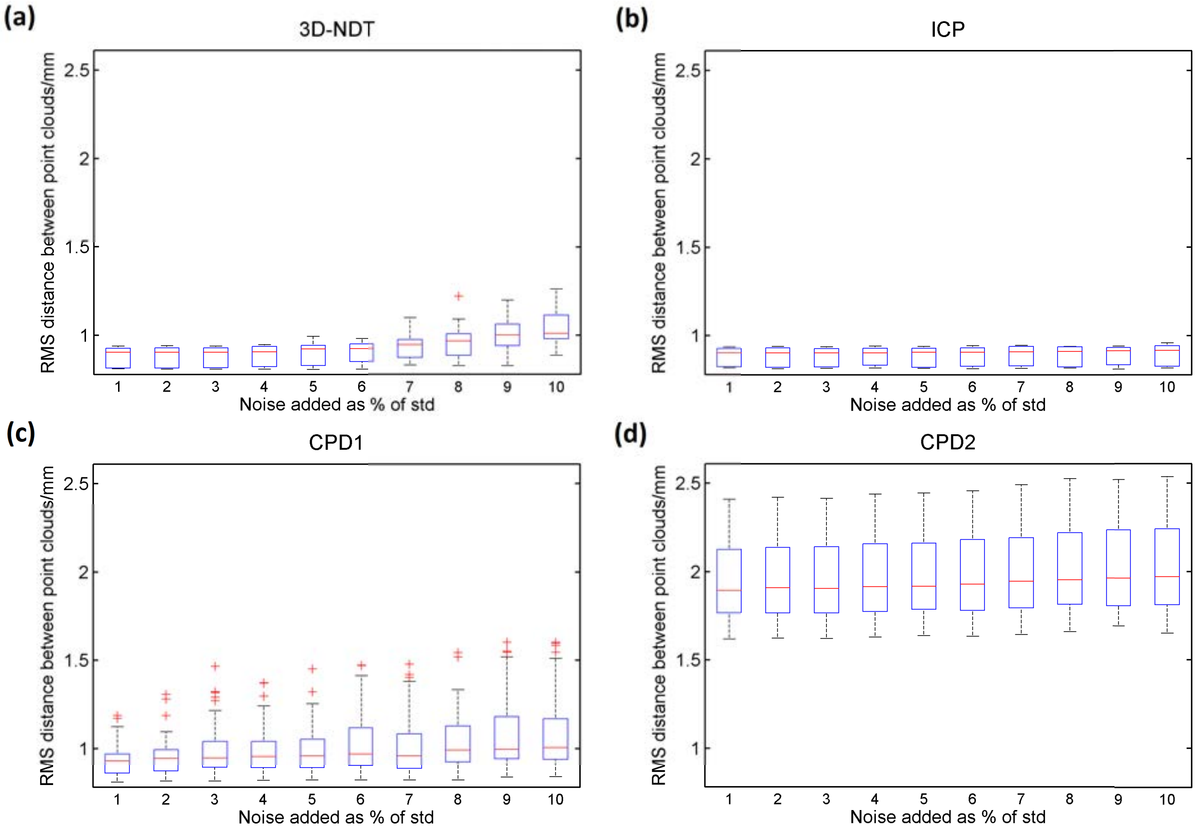

FIGURE 6.2: RMS distances for registration of noisy point clouds using (a-d) 3D-NDT, ICP, CPD1, and CPD2, with the noisy point cloud as the source.

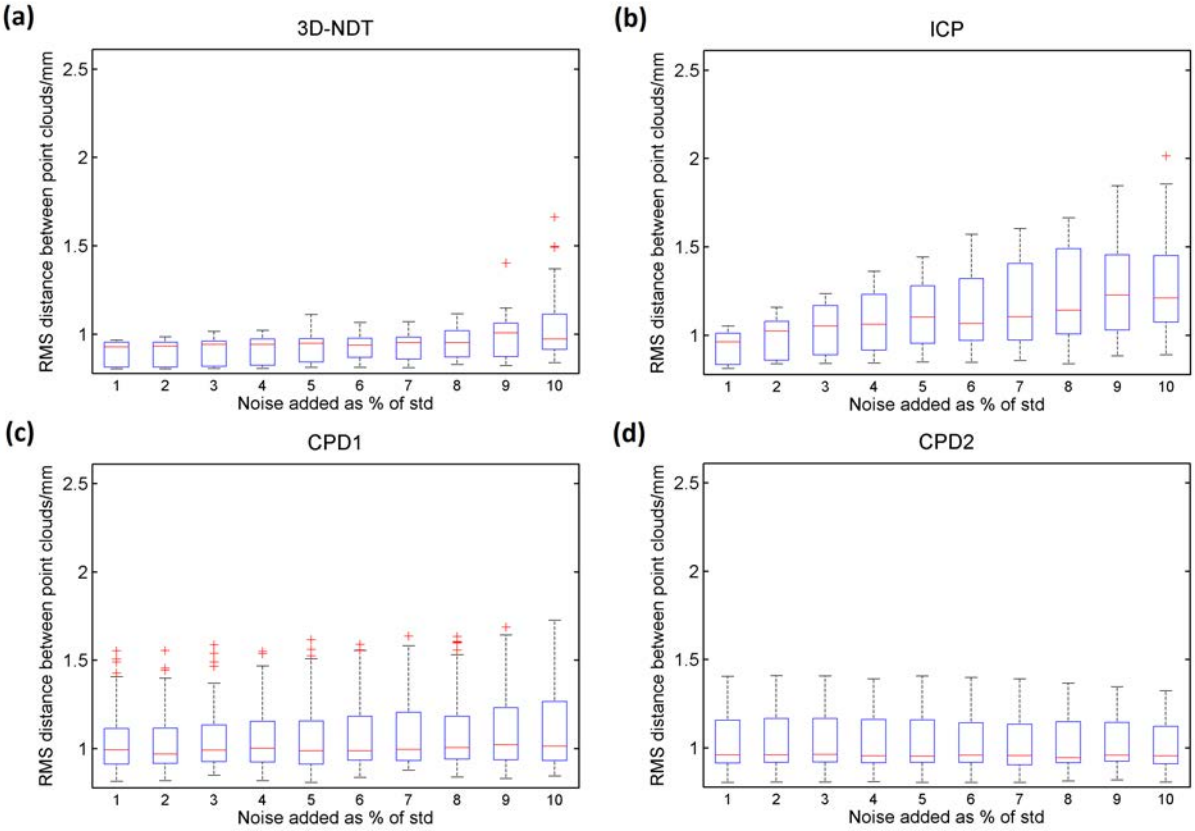

FIGURE 6.3: RMS distances for registration of noisy point clouds using (a-d) 3D-NDT, ICP, CPD1, and CPD2, with the noisy point cloud as the reference.

reference, because ICP performed worse where the noisy point clouds were the reference (as discussion in section 5.4.2.5). However, the registration could be performed in either direction and the inverse transformation used, so ICP may be a better choice where noise is present. It is not clear why 3D-NDT performed more poorly than ICP for higher noise levels. The implementation was designed for scans on the scale of a room, so possibly further optimisation is needed to improve performance on this scale. 3D-NDT performed better than CPD for greater initial transformations and for higher noise levels.

Again, registration accuracy has been considered only in terms of surface accuracy, as measured by the RMS distance between aligned point clouds after registration. In surgery, it will be important to ensure that the full planned trajectory to the target point within the head is followed accurately, so in the next chapter the effect on accuracy at points throughout the head is examined.

Chapter 7

Registration Accuracy at Target Point

7.1 Contributions to the work

MRI data was converted to meshes and segmented into regions by Xue Wu [108], all other work was done by the author.

7.2 Introduction

Previous chapters have dealt with surface registration and described registration accuracy in terms of the RMS distance between surface points, however it is the accuracy with which the planned route is followed and the target point in the brain reached that determines whether the method can be used in surgery. Therefore, a method is needed which will determine the accuracy of the registration algorithm at points *within* the head.

Surface capture data only contains information about the head surface as recorded in surgery, but the preoperative CT/MRI data to which it is to be registered contains information about the whole volume of the head. This means that a point cloud can be created using points extracted from the entire volume of the CT/MRI data. The internal points cannot be used in the registration process as there are no corresponding points in the surface capture data, but they can be used to measure registration accuracy within the head: by applying the initial transformation to place the points in the starting position for the registration process, followed by the transformation obtained by the algorithm, the final distance of each point from its starting position can be determined.

The MRI data is segmented into five regions: skin, skull, cerebrospinal fluid (CSF), grey matter and white matter. The data is made up of points (or nodes) which are each assigned to one of these regions. This allows the error to be examined within each region of the head, so that the effect on the brain can be assessed. The required application accuracy depends on the type of procedure being performed: submillimetre accuracy is needed in the treatment of Parkinson's disease, while for tumour biopsy or therapy, an accuracy of 2-3 mm is sufficient [56].

7.3 Comparing registration error between heads

As described in section 4.4.1, region of interest (ROI) surface point clouds were isolated from full volume point clouds, which were extracted from preoperative MRI data; re-meshed surface point clouds were produced from the initial ROI surface point clouds. In order to examine errors propagated within the head, registration was performed using the surface point clouds, and the resulting transformations were applied to the full volume point cloud. Across the ten subjects, the mean number of points in the full volume point clouds was 417,820±36,138; there were 14,244±852 points in the ROI surface point clouds and 14,237±839 in the re-meshed ROI surface point clouds (Table 4.1).

In order to compare internal errors between subjects, the re-meshed ROI surface point clouds were each put through a rotation of $\pi/5$ radians about the x-axis and a translation of 20 mm in each of the x, y and z directions. The transformed point clouds were then registered to the original ROI surface point clouds using the ICP registration algorithm. The nodes of the 3D segmented MRI data were put through the same transformations as the corresponding re-meshed point clouds (an initial transformation to the starting point of the registration algorithm, followed by the transformation determined by the algorithm; Fig. 7.1). The Euclidean distance between each node in the transformed and registered full MRI data and the same point in the initial data was calculated and plotted as a colour (Figs. 7.2 and 7.3). In order to show the error inside the head, slices are taken through the origin of the coordinate system (approximately the centre of the point clouds), normal to each axis.

The slices show that the registration error tends to be higher on the right side of the head and, in some cases, towards the back. The initial position of the source point cloud was a $\frac{\pi}{5}$ radian rotation about the x-axis, towards the right side of the head, plus a 20 mm translation in each of the x, y and z directions. This implies that the algorithm tends to get stuck in a local minimum when the source cloud is closest to the reference cloud on the opposite side of the head to the direction of initial rotation.

The segmentation of the MRI data allows the RMS error at the surface of different regions of the brain resulting from surface registration to be visualised (Fig. 7.4), showing the same trend.

For all heads and regions, all distances between corresponding points are submillimetre, with a [median]±[standard deviation] distance of 0.328±0.155 mm (Fig. 7.5). The distance data was found to lack homogeneity of variance ($p < 2.2 \times 10^{-16}$) using Barlett's test in R [118]. A Kruskal-Wallis test was performed and significant effects of

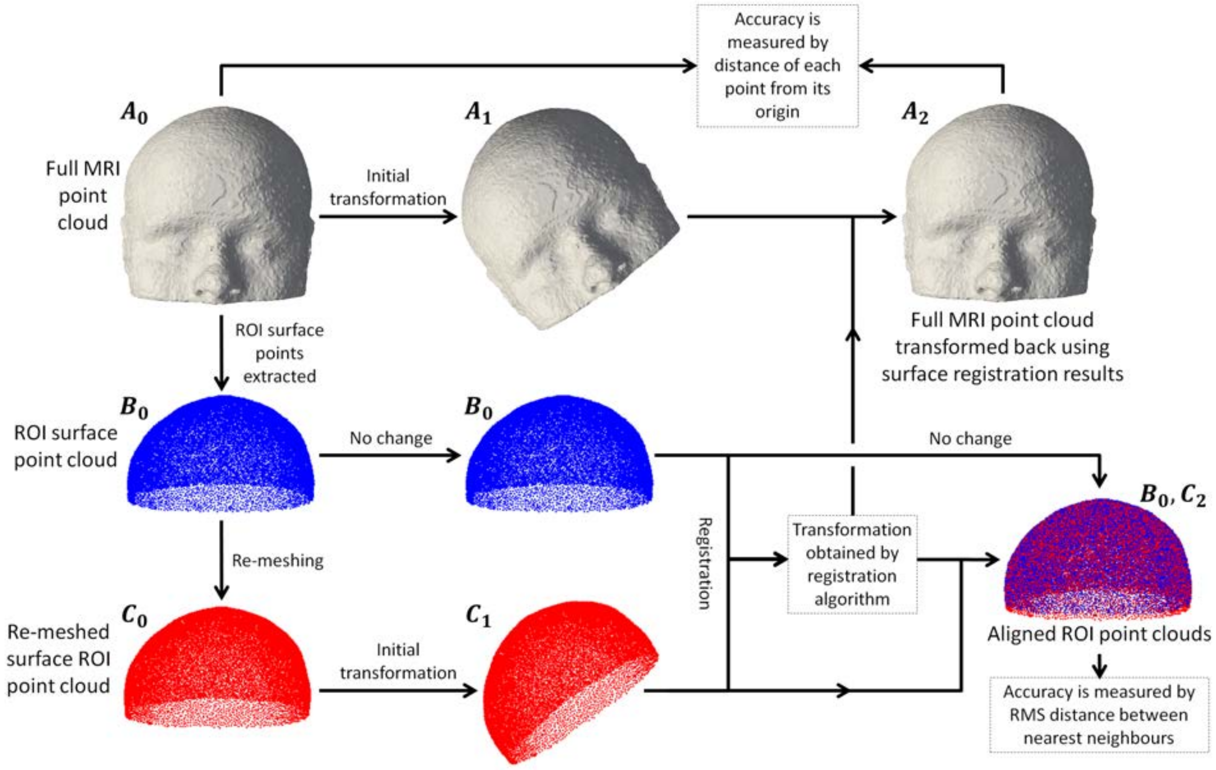

FIGURE 7.1: A full volume point cloud A_0 (shown as a mesh) extracted from MRI data is used to determine errors within the head based on ROI surface point cloud registration. Registration is performed between B_0, an ROI surface point cloud extracted from A_0, and C_0, a re-meshed version of B_0. A_0 and C_0 are put through the same initial transformation to give A_1 and C_1. A registration process is then carried out to determine the transformation needed to register C_1 to B_0. This resulting transformation is then applied to A_1 to give A_2. The error at each point in A_2 as a result of the surface registration between C_1 and B_0 is given by the Euclidean distance between that point and the corresponding point in A_0.

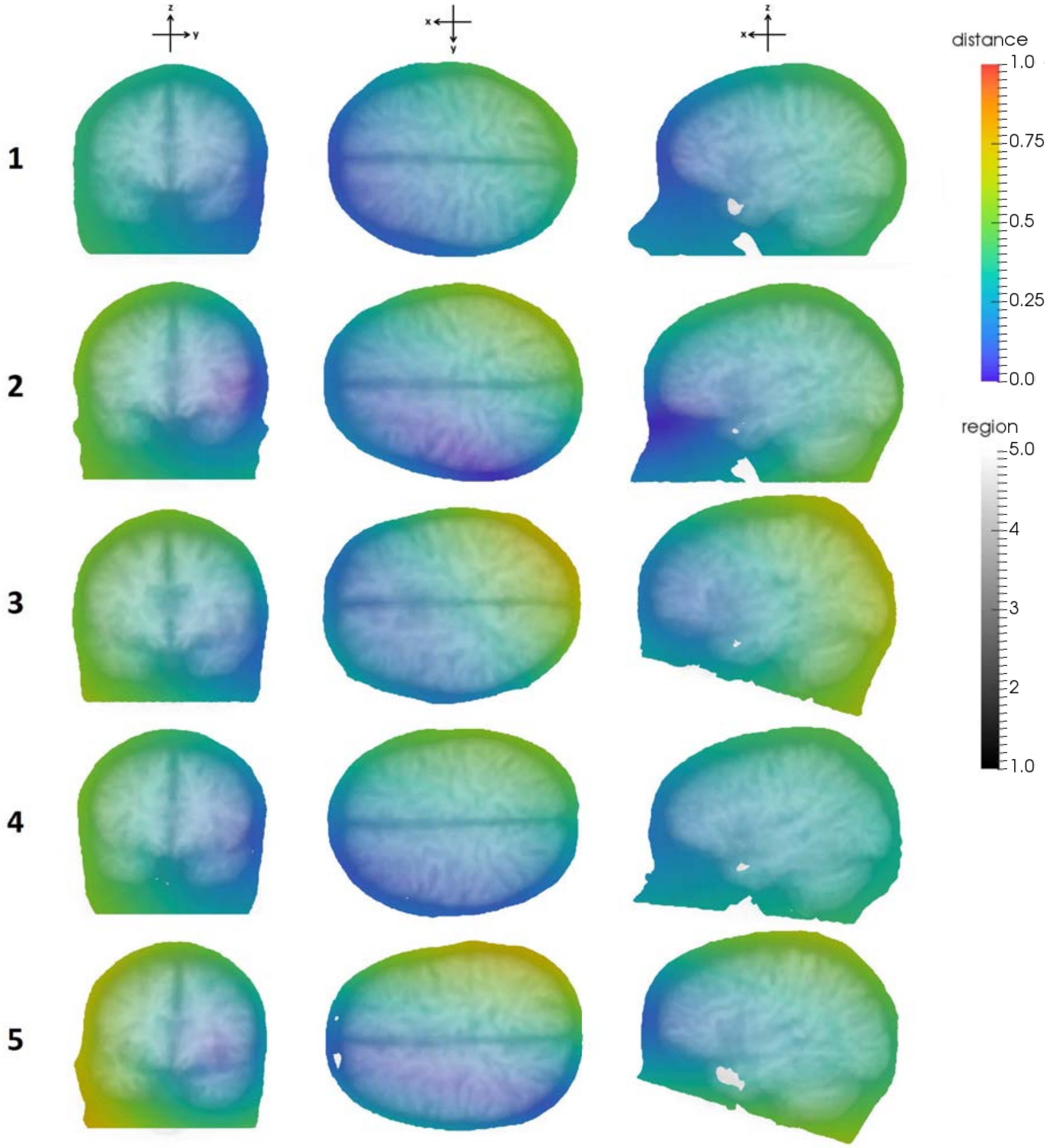

FIGURE 7.2: Slices through point clouds from five MRIs (1-5): colour shows RMS error after alignment by ICP from an initial rotation of $\frac{\pi}{5}$ radians about x-axis and translation of 20 mm in x, y, and z directions. Slices shown are through the origin, normal to (left to right) the x (seen from front), z (seen from above, front is on left side), and y (seen from left side) axes. Head region is superimposed in transparent greyscale.

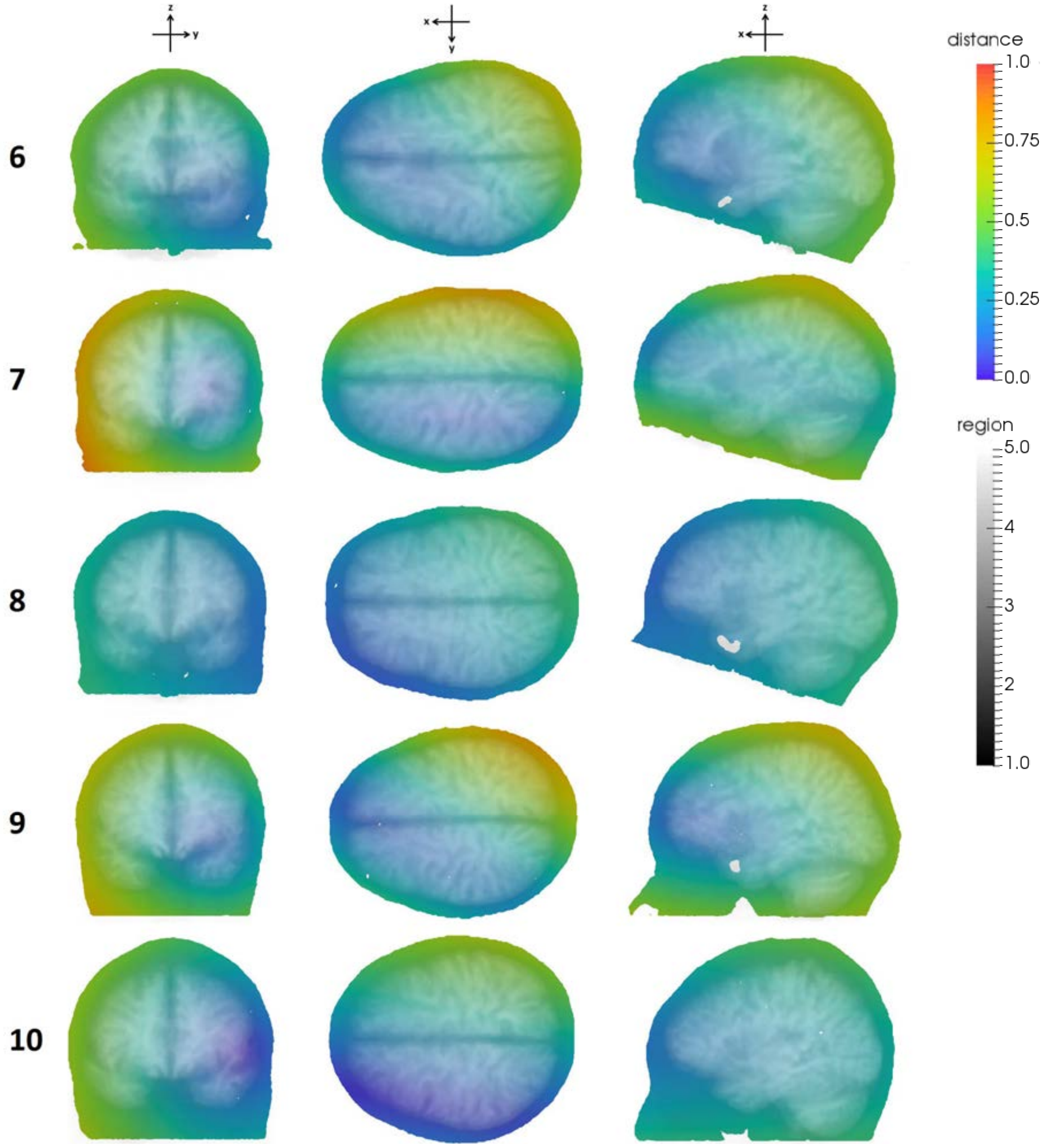

FIGURE 7.3: Slices through point clouds from five MRIs (6-10): colour shows RMS error after alignment by ICP from an initial rotation of $\frac{\pi}{5}$ radians about x-axis and translation of 20 mm in x, y, and z directions. Slices shown are through the origin, normal to (left to right) the x (seen from front), z (seen from above, front is on left side), and y (seen from left side) axes. Head region is superimposed in transparent greyscale.

region and subject were found ($p < 2.2 \times 10^{-16}$). There was a general trend of lower distances in regions nearer the centre of the head. Since the point clouds are being registered from a rotated position and are translated to bring their centres of mass together, absolute distances can be expected to be greater further from the axis of rotation in the centre of the point cloud. Post hoc tests were performed using Benjamini-Hochberg adjustment; more than 98% of comparisons were significant ($p < 0.01$).

7.4 The effect of rotation about different axes

This work has so far used a single direction of rotation to test registration algorithms: positive rotation about the x-axis. As seen in section 7.3, when using ICP, this has mainly resulted in an alignment which is closer on the left side of the head: the opposite side to that toward which the re-meshed point cloud was initially rotated. This suggests that the algorithm gets stuck in a local minimum on this side; if so, it would be expected that an initial rotation in the opposite (negative) direction about the x-axis would result in an alignment which is closer on the right side of the head.

In order to assess the effect of rotation in both directions about the x-, y-, and z-axes, six initial positions for the source point cloud were defined by putting the initial re-meshed ROI point cloud through rotations of $\pi/5$ radians in either the positive and negative direction about the x-, y-, or z-axis. $\pi/5$ radians was chosen as being large enough to test the algorithm, but not so large that the point clouds could be turned upside down. Only head '1' was tested. Each rotated point cloud was translated by 20 mm in each of the x, y, and z directions. The point clouds were then registered to the original ROI point cloud using ICP, as described in section 4.4.4 and the corresponding errors for the full head were determined (Figs. 7.6 and 7.7).

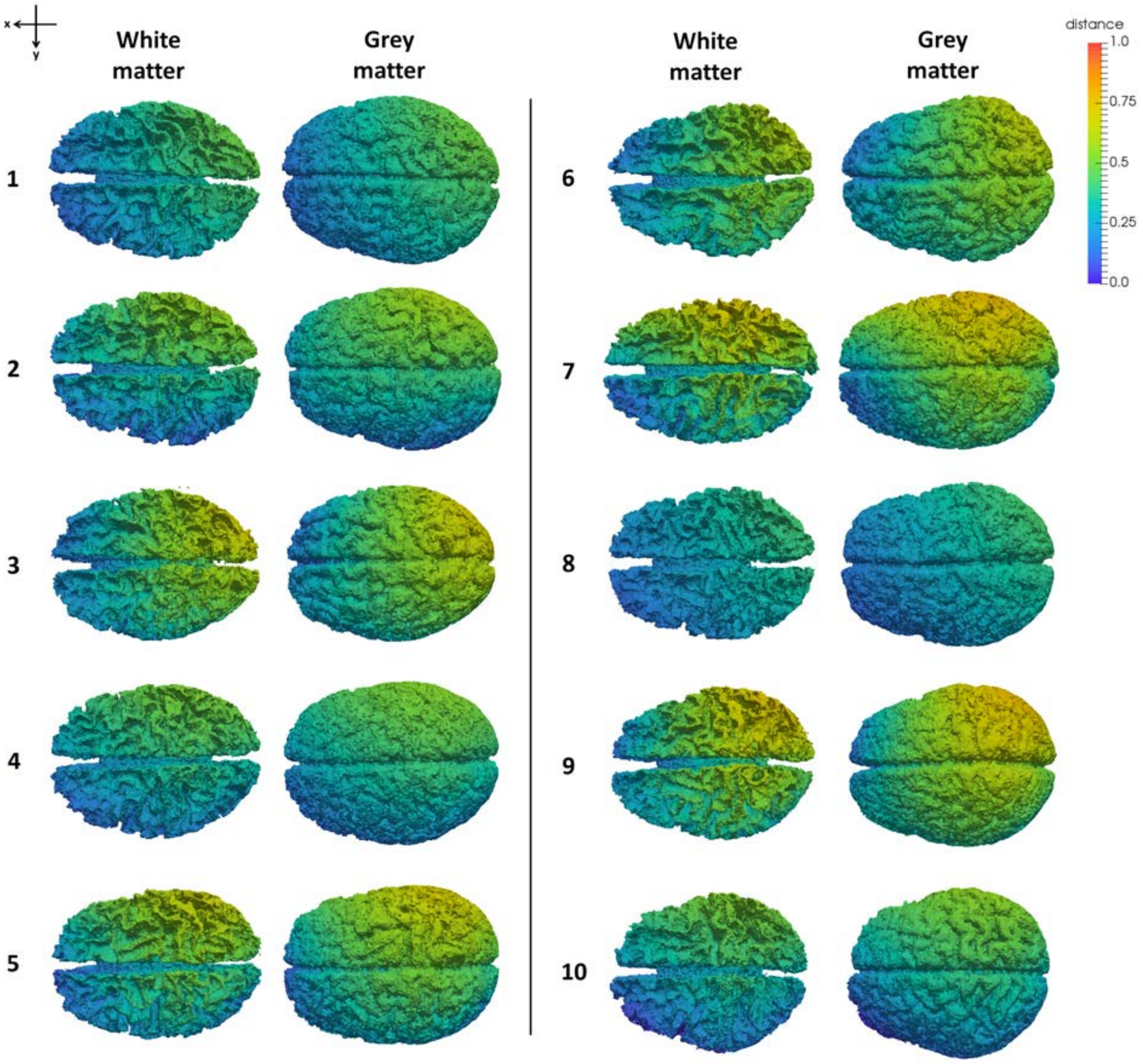

FIGURE 7.4: Errors at the surfaces of white and grey matter for the ten heads in Figs. 7.2 and 7.3.

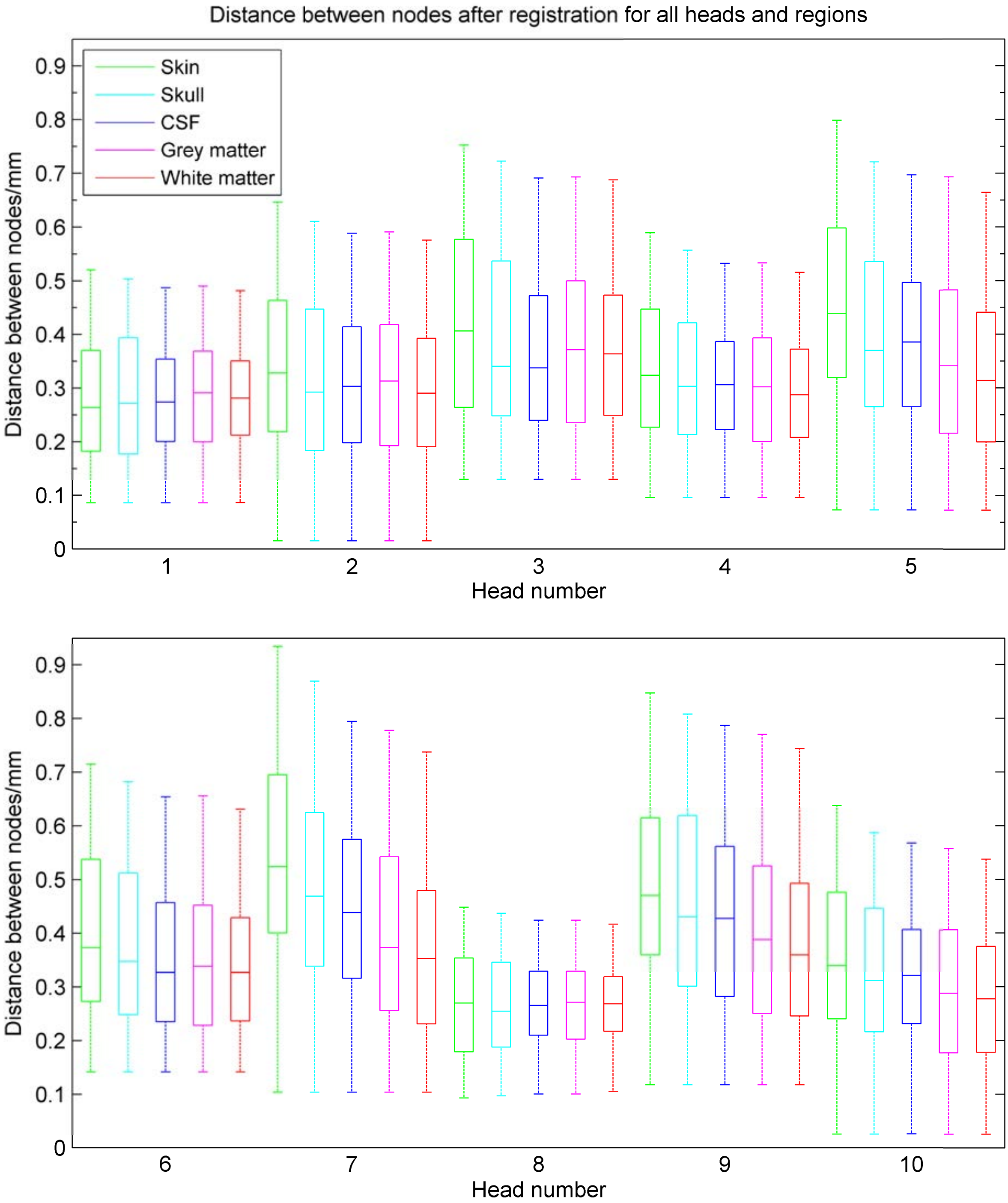

FIGURE 7.5: Node distances for each region for the ten heads in Figs. 7.2 and 7.3.

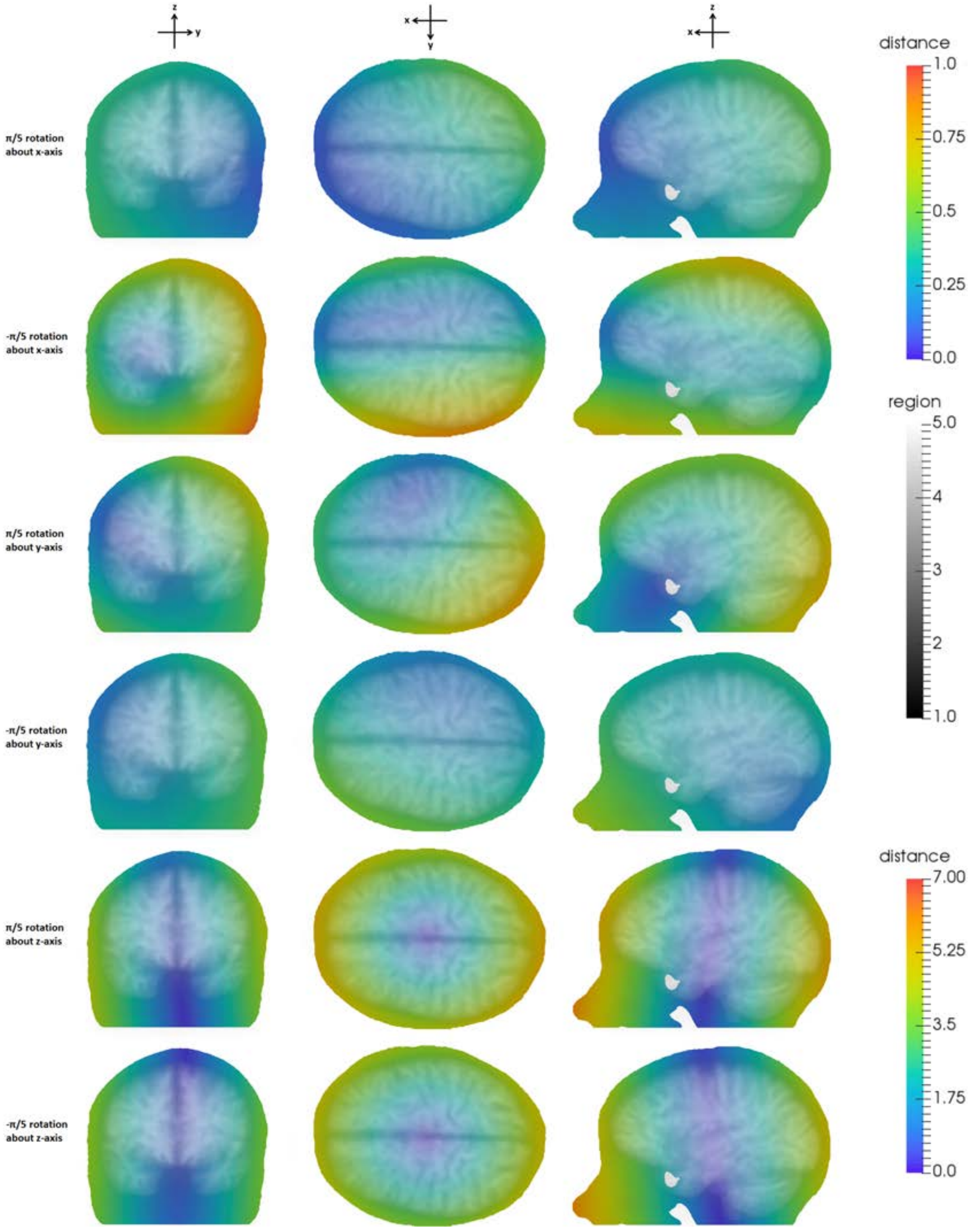

FIGURE 7.6: The effect of positive and negative initial rotation about the x-, y-, and z-axes on volumetric error in mm. For rotation about the x- and y-axes, all errors are less than 1 mm; for rotation about the z-axis, they are up to 6.2 mm. All point clouds were given an initial translation of 20 mm in all directions.

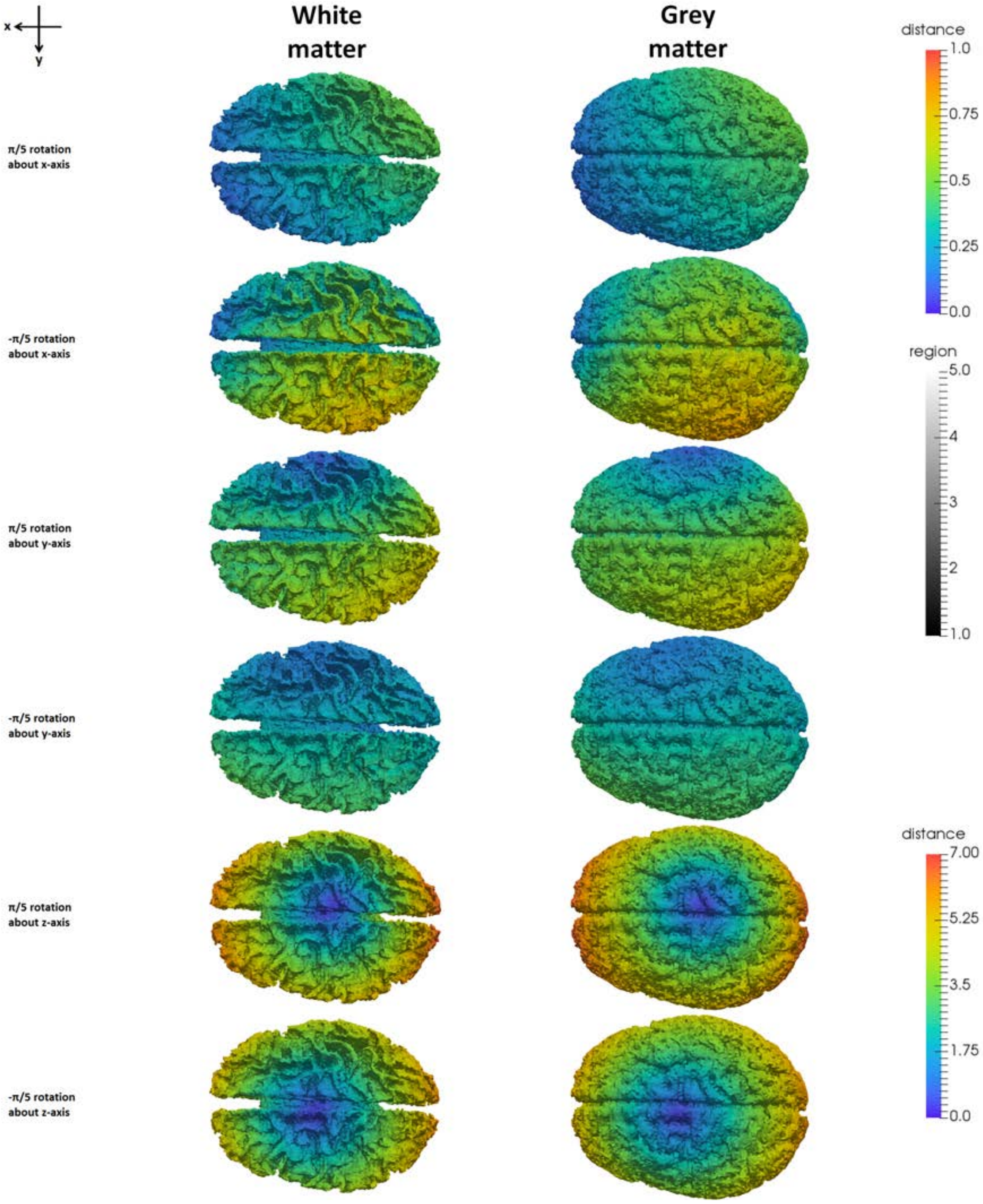

FIGURE 7.7: Errors at the surface of white and grey matter for the registrations in Fig. 7.6.

Initial rotation in the negative direction about the x-axis resulted in closer registration on the right of the head, and a poorer registration on the left side, the opposite to the result when the rotation was in the positive direction. The magnitude of the separation between aligned heads on the less well aligned side of the head was greater for negative than for positive initial rotation. Rotation in the positive and negative direction about the y-axis (approximately equivalent to rotating the head forwards and back, respectively) resulted in closer alignment at the front and back of the head respectively, but in both cases the closer region was more on the right than the left side of the head. In all cases, the greatest distance between corresponding points was 0.972 mm. Where the rotation was about the z-axis in the positive or negative direction (turning the head to the left and right respectively about a vertical axis through the centre), the resulting alignment was considerably less close than for x and y rotation, with a distance of up to 6.18 mm between corresponding points (Figs. 7.8, 7.9). The median distance for points after +z or -z rotation was 3.02±1.14 mm, as compared with 0.329±0.172 mm for x rotation and 0.335±0.151 mm for y rotation. The alignment was worse at greater distance from the axis and in both cases was slightly worse in the direction of the initial rotation, suggesting that in this case the algorithm became stuck in a local minimum before the point cloud was fully rotated back to the starting position.

Kruskal-Wallis testing showed significant effects on error of region and initial rotation ($p < 2.2 \times 10^{-16}$). Post hoc tests showing significant differences ($p < 0.01$) for all combinations of regions and initial rotation, except for two, which did not appear to be meaningful (between region 2, +y rotation and region 4, -x rotation; region 3, +x rotation and region 4, -y rotation).

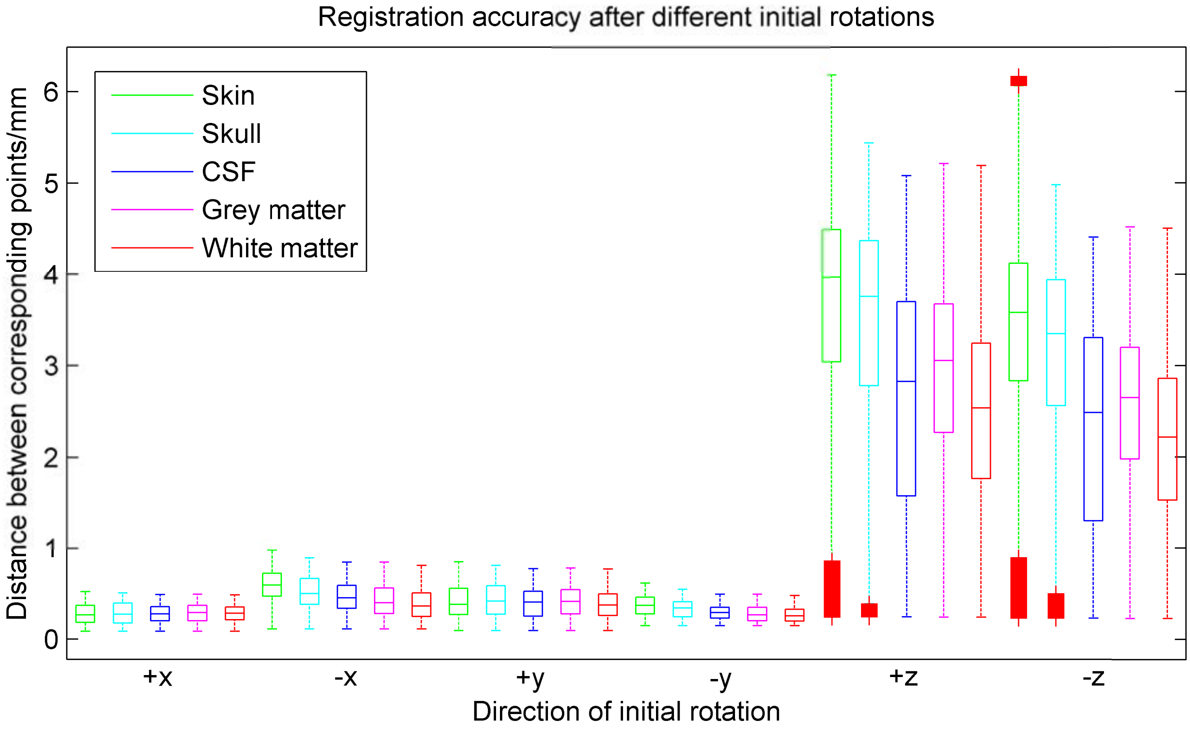

FIGURE 7.8: Distances between corresponding points after registration from initial rotations of $\frac{\pi}{5}$ radians in the positive and negative directions about the x-, y-, and z-axes.

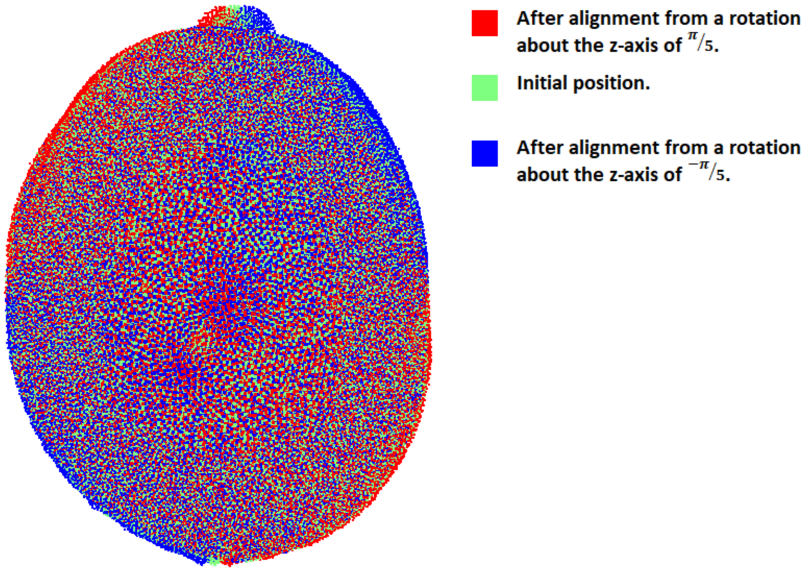

FIGURE 7.9: The position of the point cloud after ICP alignment from rotations of $\frac{\pi}{5}$ and $\frac{-\pi}{5}$ radians about the z-axis, shown from above.

7.5 The effect of prealigning point clouds using principal component analysis

The results of section 7.4, suggest that initial rotations about the z-axis have a much larger effect on registration accuracy than those about the x- and y-axes. A better initial alignment between point clouds could mitigate this effect. The registrations described in section 7.4 were repeated, but this time the re-meshed ROI point clouds were globally aligned using principal component analysis before registration as described in section 4.4.3. The initial ROI point clouds were positioned so that their principal components were approximately aligned with the x-, y-, and z-axes, so this process should bring the transformed, re-meshed point clouds back into closer alignment with the originals.

The prealignment step resulted in much better alignment between registered point clouds, irrespective of about which axis the point cloud had initially been rotated and in which direction (Figs. 7.10 and 7.11) and all corresponding point distances were less than 0.451 mm (Fig. 7.12). The median values were 0.272±0.066 mm for all initial directions of rotation. All initial rotations resulted in a slightly closer alignment at the front of the head than at the back. Kruskal-Wallis tests were performed; there was a significant effect of region ($p < 2.2 \times 10^{-16}$), but not of initial rotation ($p = 1$), suggesting that prealignment eliminates the effect of initial transformation.

Prealignment was also performed for all heads using the initial rotation of $\frac{\pi}{5}$ radians about the x axis (Figs. 7.13, 7.14 and 7.15), again resulting in closer median alignment (0.283±0.087 mm) than the equivalent registrations without using prealignment with PCA, for all regions and most heads (Figs. 7.16 and 7.16). Kruskal-Wallis testing showed significant effects on error of subject and region ($p < 2.2 \times 10^{-16}$). Over 97% of post hoc comparisons were significant ($p < 0.01$).

7.6 Conclusion

In this chapter, the errors at points throughout the head as a result of some of the ICP surface registrations performed in chapters 4 and 5 have been determined. Registrations performed with point clouds from ten subjects which had been rotated $\frac{\pi}{5}$ radians about the x-axis resulted in a median error at points throughout the head of 0.328±0.155 mm. The effect of initial rotation about each of the three main axes was also been examined. Positive and negative initial rotations about the x-axis resulted in a slightly poorer alignment on the side towards which the point cloud had initially

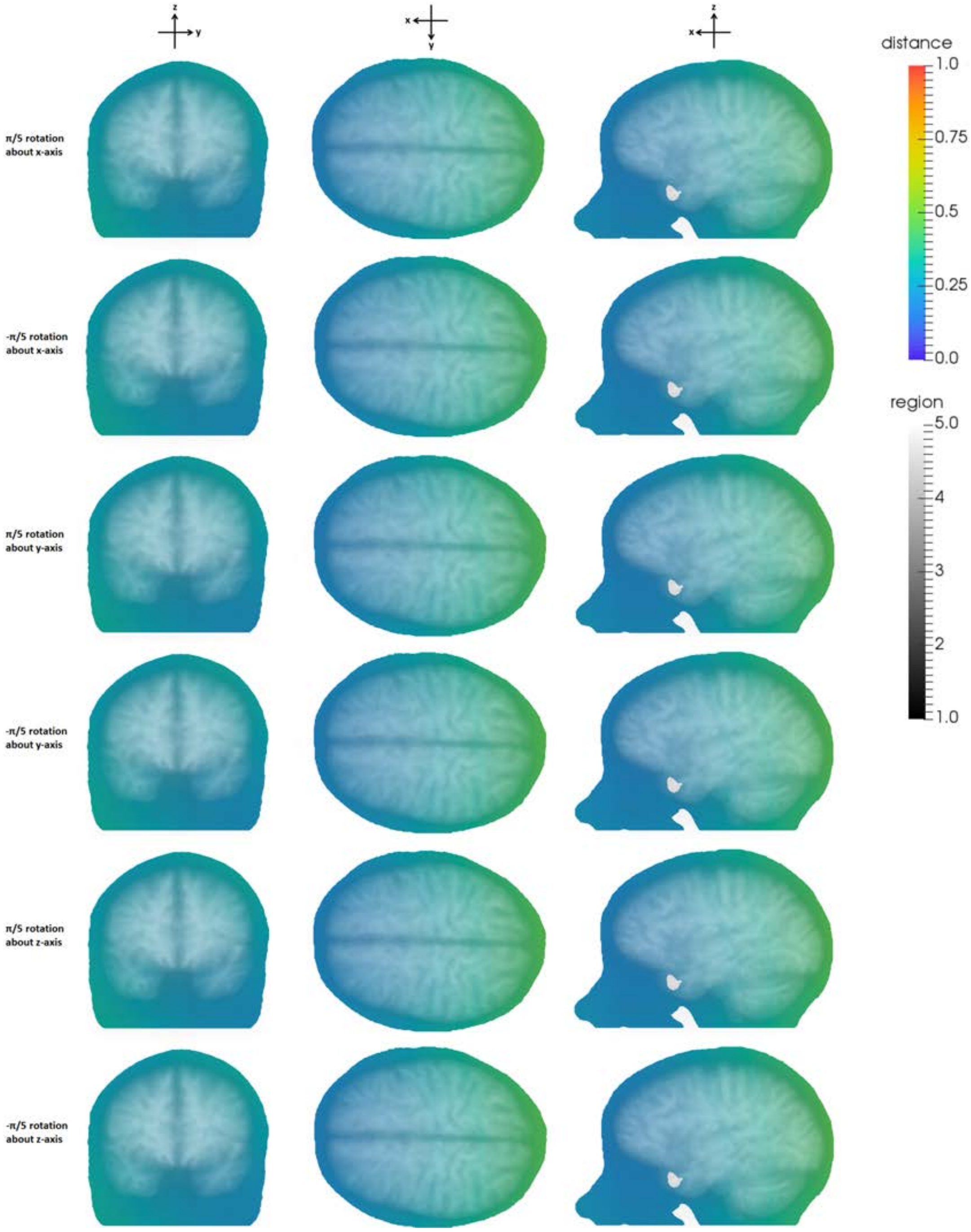

FIGURE 7.10: The effect of positive and negative initial rotation about the x-, y- and z-axes on volumetric error in mm, having performed an initial alignment using PCA. All errors are now less than 1 mm. All point clouds were given an initial translation of 20 mm in all directions.

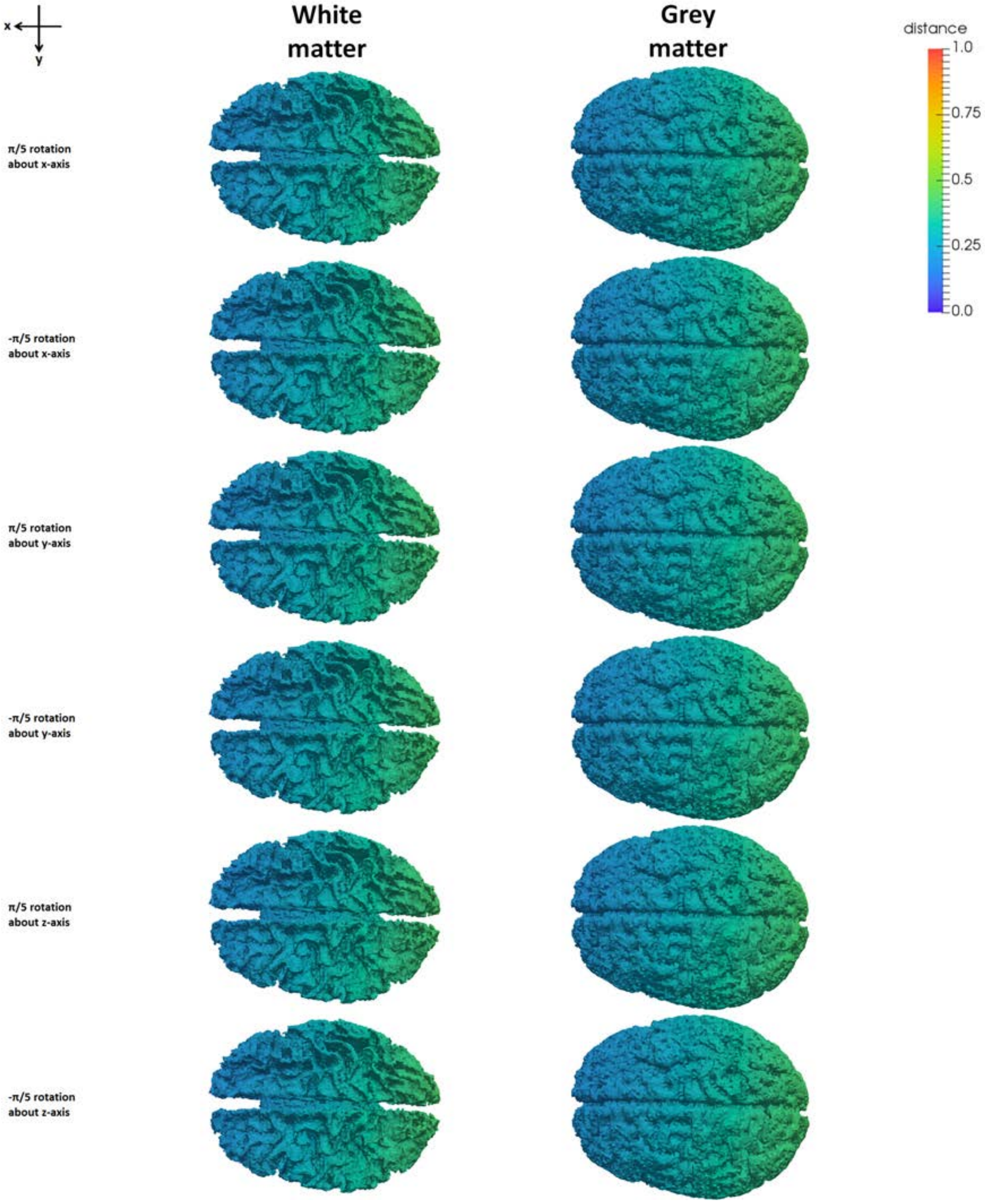

FIGURE 7.11: Errors at the surface of white and grey matter for the registrations in Fig. 7.10.

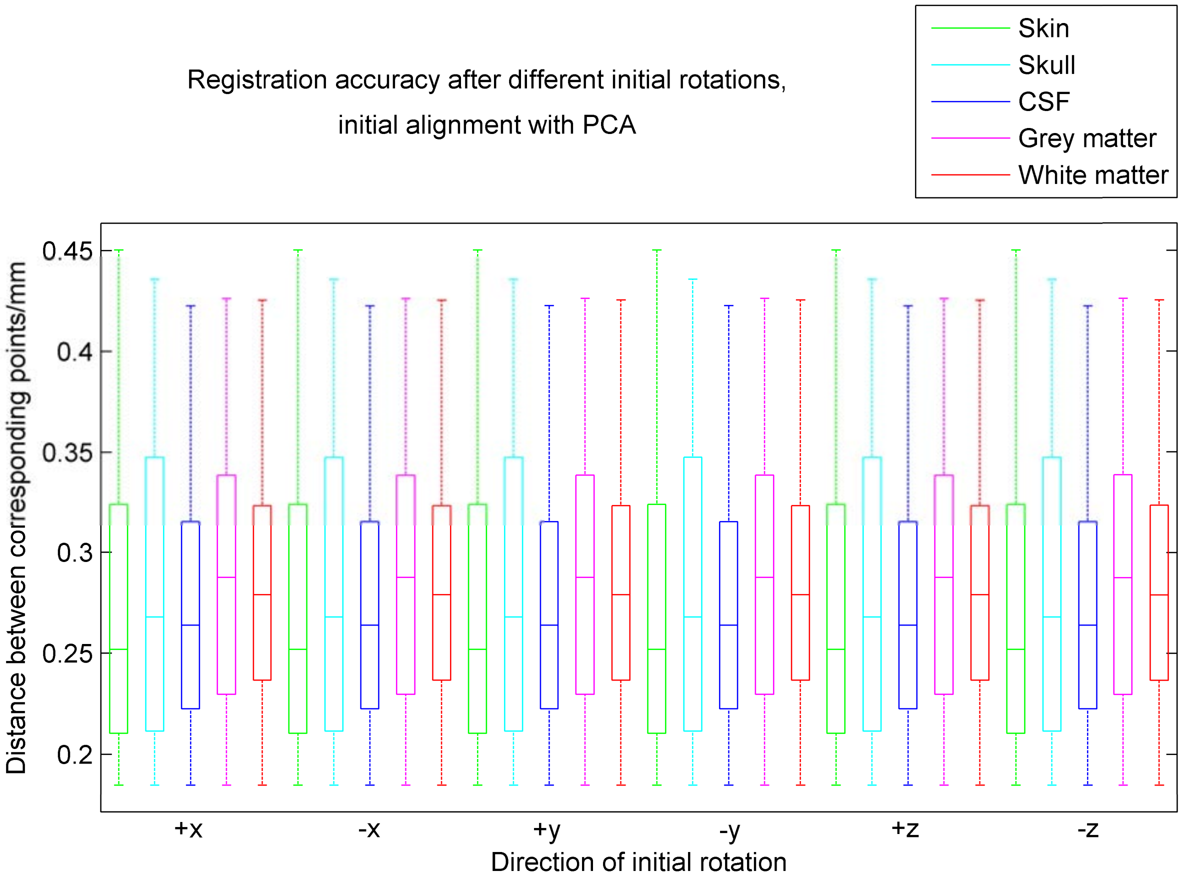

FIGURE 7.12: Distances between corresponding points after registration from initial rotations of $\frac{\pi}{5}$ in the positive and negative directions about the x-, y-, and z-axes, after alignment with PCA.

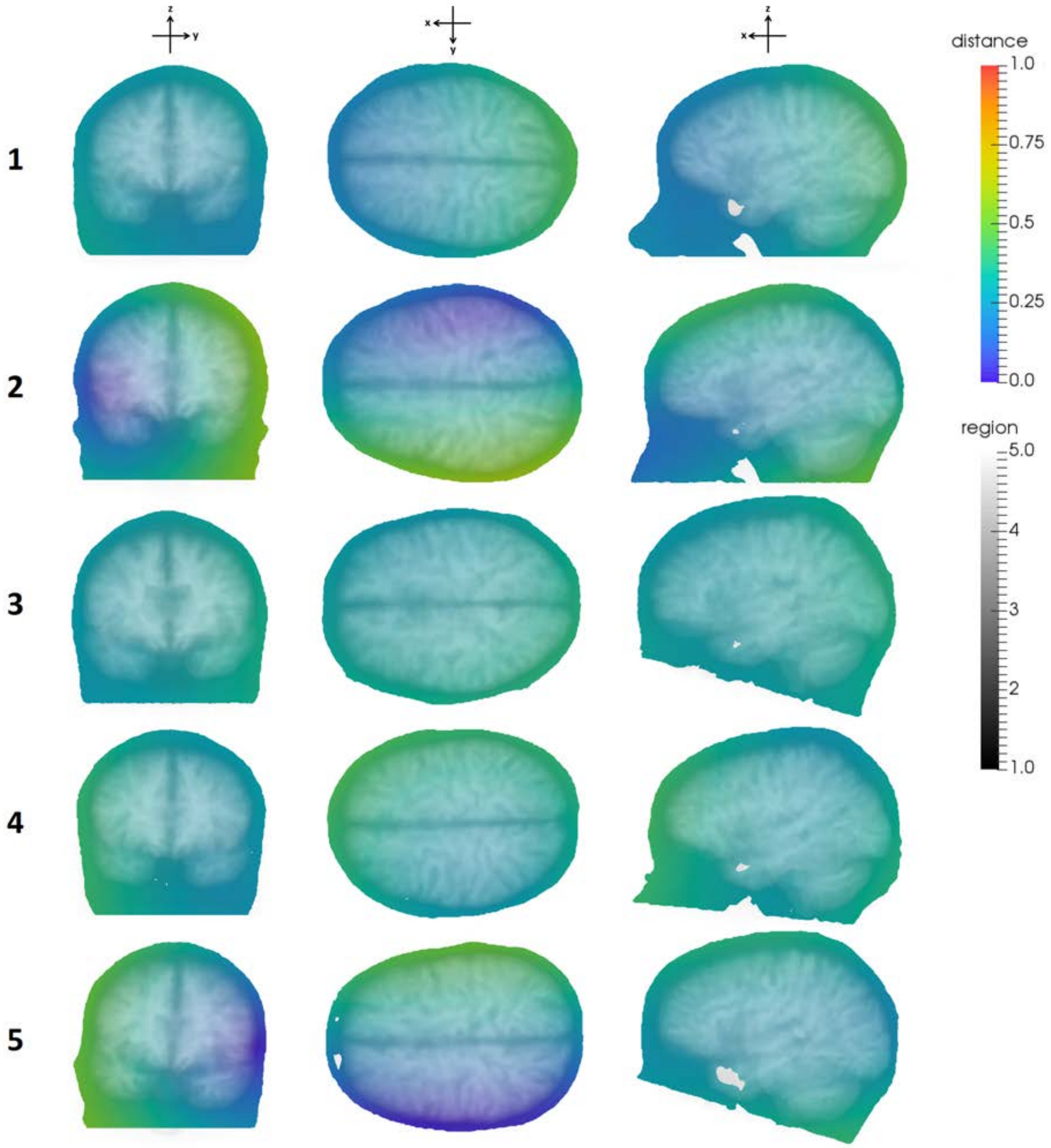

FIGURE 7.13: Slices through point clouds from five MRIs (1-5); colour shows RMS error after alignment by ICP from an initial rotation of $\frac{\pi}{5}$ about x-axis and translation of 20 mm in x, y and z directions. Prealignment with PCA was used. Slices shown are through the origin, normal to: (left to right) the x (seen from front), z (seen from above, front is on left side) and y (seen from left side) axes. Head region is superimposed in transparent greyscale.

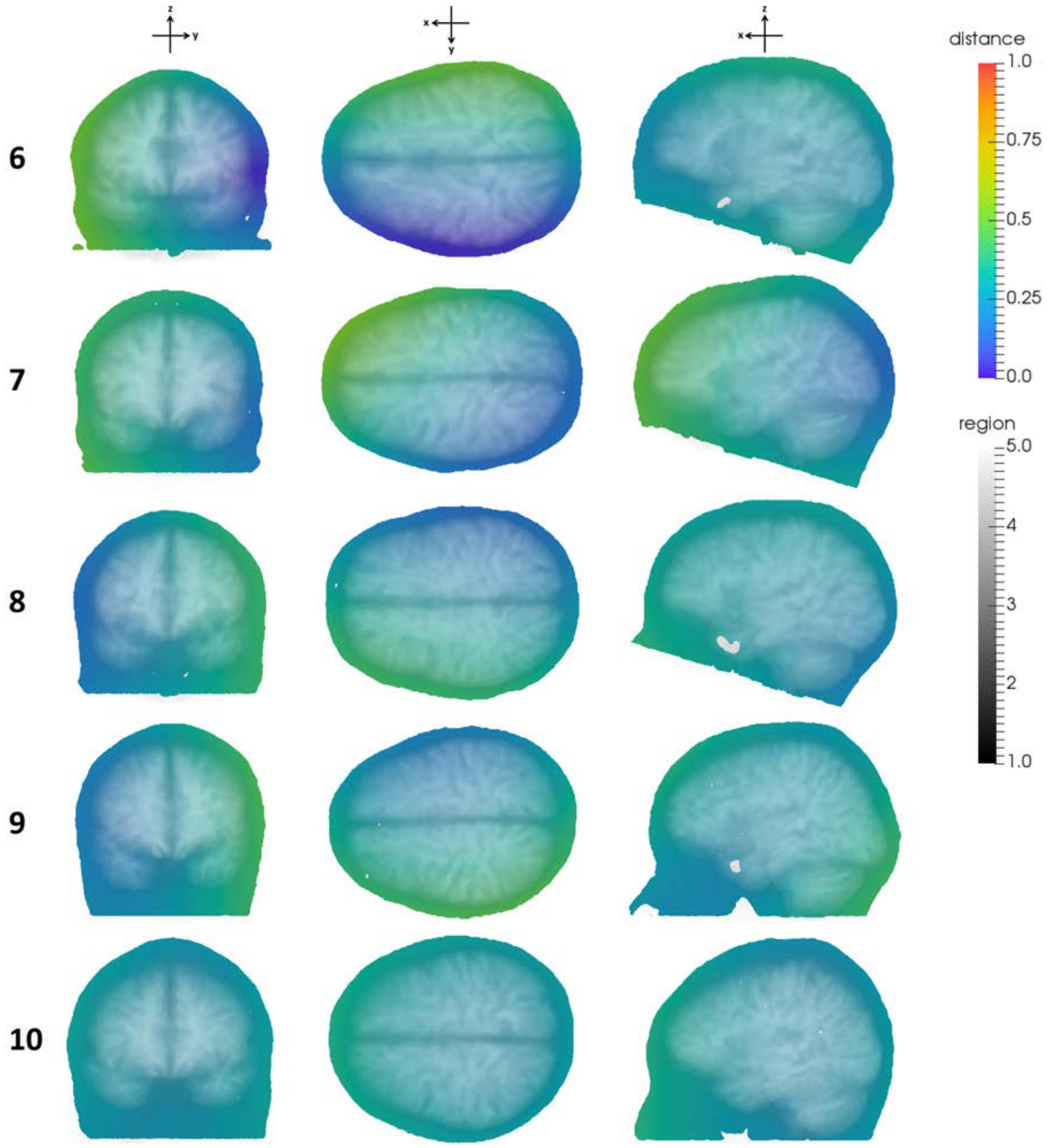

FIGURE 7.14: Slices through point clouds from five MRIs (6-10); colour shows RMS error after alignment by ICP from an initial rotation of $\frac{\pi}{5}$ about x-axis and translation of 20 mm in x, y and z directions. Prealignment with PCA was used. Slices shown are through the origin, normal to: (left to right) the x (seen from front), z (seen from above, front is on left side) and y (seen from left side) axes. Head region is superimposed in transparent greyscale.

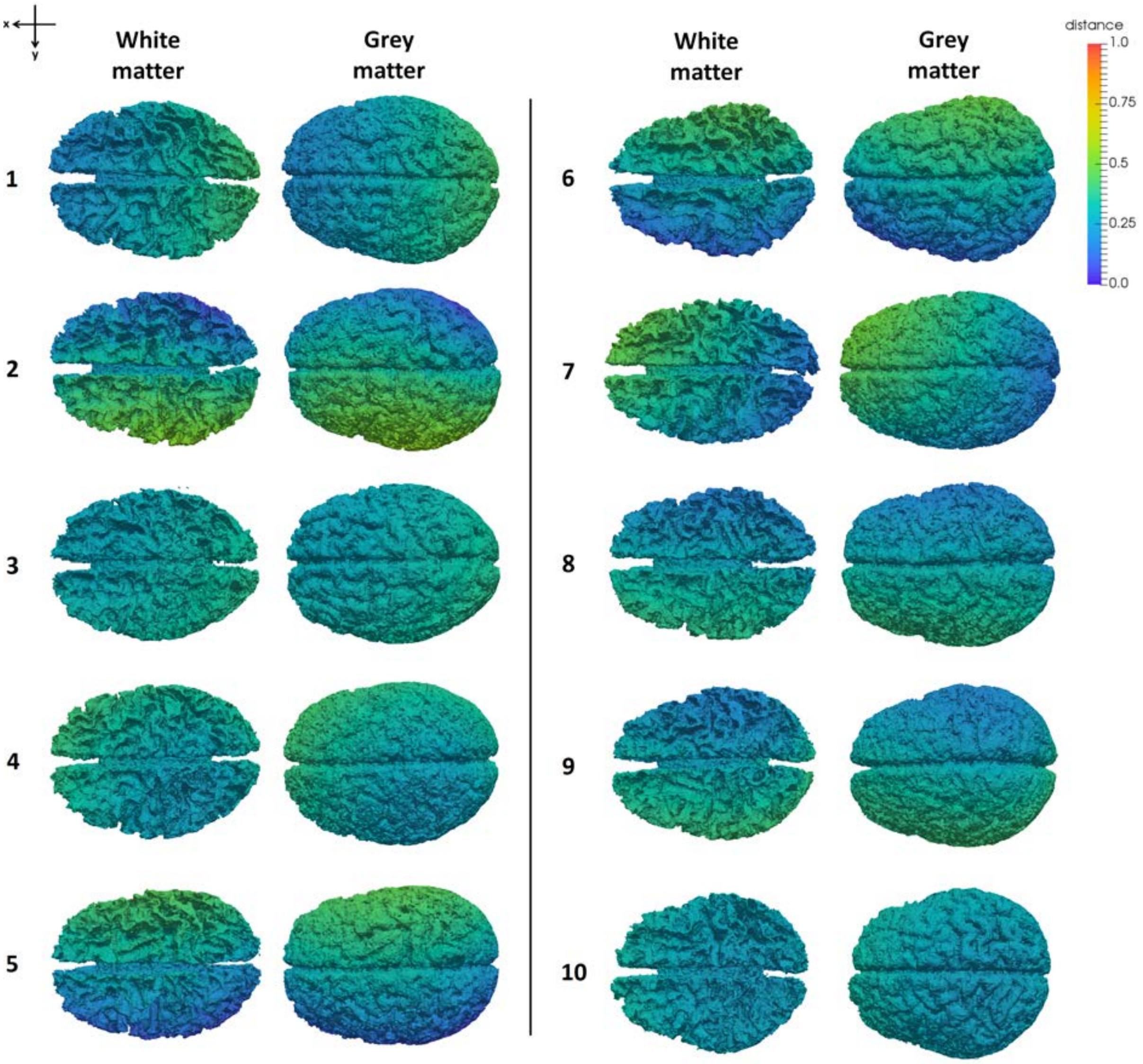

FIGURE 7.15: Errors at the surfaces of white and grey matter for the ten heads in Figs. 7.13 and 7.14. Prealignment with PCA was used.

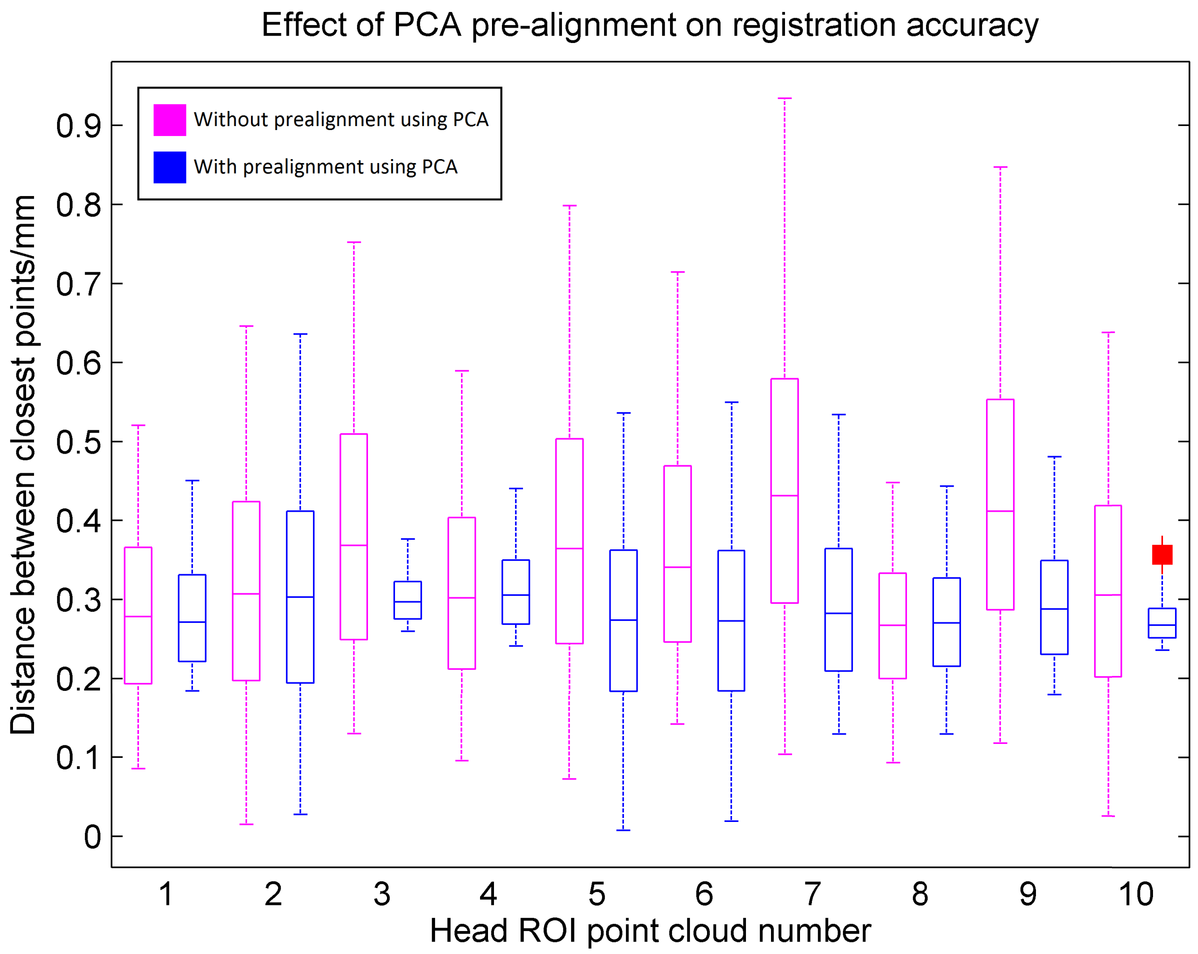

FIGURE 7.16: Registration accuracy in whole head, across all ten point clouds, with and without prealignment with PCA. Surface registration using from an initial transformation of $\frac{\pi}{5}$ rotation about the x-axis and 20 mm translations in the x, y and z directions was performed. The initial transformation was applied to the full point cloud, followed by the transformation calculated by the registration algorithm and the distance of each point from its initial position was found. Red crosses show outliers.

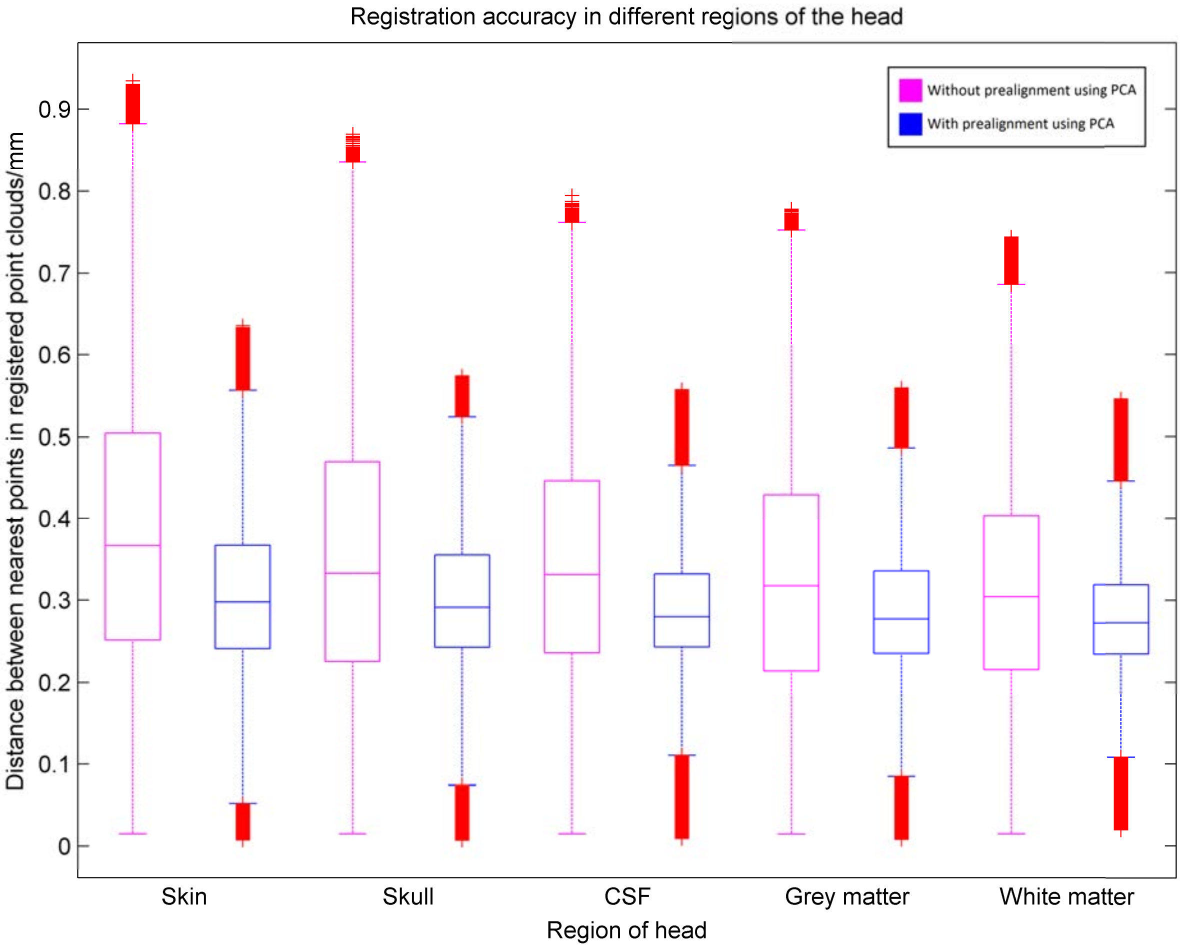

FIGURE 7.17: Registration accuracy in different regions of the head, across all ten point clouds, with and without pre-alignment with PCA. Surface registration using from an initial transformation of $\frac{\pi}{5}$ rotation about the x-axis and 20 mm translations in the x, y and z directions was performed. The initial transformation was applied to the full point cloud, followed by the transformation calculated by the registration algorithm and the distance of each point from its initial position was found. Red crosses show outliers.

been rotated and a median error of 0.329±0.172 mm. Initial rotation about the (vertical) z-axis resulted in larger errors than rotations about the other two axes, with a median error of 3.03±1.14 mm. Prealigning the point clouds using principal component analysis eliminated the differences in results between the different directions of initial rotation and resulted in submillimetre differences at all points throughout the head, with a median of 0.283±0.087 mm for all heads after +x rotation, and 0.272±0.066 mm for the single head, with positive and negative x, y, and z rotation.

This suggests that the submillimetre errors required in neurosurgery may be achievable using the ICP surface registration method, if prealignment is used. However, the successful application of prealignment may rely on the successful imaging of the ROI, which may be difficult if some of the head is obscured. In addition, these registrations have been performed using idealised point clouds, which may lack the faults of real surface capture data. Noisy data has not been tested in this chapter, but the results of chapter 5 suggest that the accuracy of the ICP surface registration algorithm is not affected by the addition of Gaussian noise with a standard deviation of up to 10% of the standard deviation of the point cloud.

Chapter 8

Conclusions and Further Work

The aim of this work is to move towards registration between surface capture images of a patient during neurosurgery and preoperative CT or MRI data, in order to accurately locate target points within the head. This will permit the patient to be moved during surgery and re-registered, allowing easier access to all parts of the head. This has been performed using idealised surface data extracted from MRI images to represent surface capture data; three registration algorithms have been tested.

8.1 Device Comparison

In order to perform registration in surgery, a suitable imaging device will be required. Developing an imaging device is beyond the scope of this project, but in order to investigate what type of data could be produced, two imaging devices were investigated in chapter 3: the in-house Birmingham Surface Capture System and the Microsoft Kinect v1. Both devices were used to image a phantom head, which had been created from subject MRI data. These images were then registered using the Iterative Closest Point (ICP) algorithm to the ground truth mesh for the phantom. The Birmingham system images were found to correspond more closely to the ground truth than the Kinect images, with a median distance from the data points to the nearest ground truth points of 0.269 mm, as compared with 1.80 mm for the Kinect; the Birmingham system also produced denser point clouds. Although this method allowed us to form a numerical assessment of how well the point clouds matched the ground truth, it was impossible to be sure how much of the error resulted from the imaging system and how much from the performance of the registration algorithm.

8.2 Partial Registration Using ICP

During surgery, the patient may be draped, or obscured by surgical equipment and it may not be possible for a surface capture imaging system to get a full view of the head. For this reason, in chapter 4, partial registration of point clouds using ICP was examined. Ten representative surface point clouds were extracted from patient MRI data and a region of interest defined excluding facial features which might be obscured or distorted in surgery; the ROI point clouds were re-meshed to provide an idealised point cloud to represent surface capture data.

Several forms of partial registration using ICP were investigated with this data. The point cloud density was reduced by randomly removing between 10% and 90% of points from the point clouds. It was found that as many as 60% of the total points could be removed without significantly affecting registration accuracy, but this result is specific to the simulated data used and might not apply to real surface capture data. Reducing point cloud density could be one way of shortening processing time, depending on initial point cloud density and the accuracy required.

Further partial registration was performed by dividing the ROI into octants, to determine how accurately registration could be performed using only parts of the head surface. One method of registration was to use the octant centres of mass as landmarks. Accuracy is limited in this case by the small number of landmarks and this method would require an image of the full region of interest, so it would not be useful if only a partial view were available.

Only part of the head may be available for imaging at any one time, but it may be possible to gain multiple surface images and combine the data. In order to investigate how much of the surface is needed to register the full surface sufficiently accurately, experiments were performed in which a single octant was initially used to perform registration and the RMS distance between point clouds was recorded as subsequent octants were added to the registration process. Registration was also performed with each possible combination of octants (from one to eight in total) simultaneously, to examine registration accuracy when using different amounts and parts of the surface.

For sequential registration, accuracy was to some extent affected by the initial octant chosen for registration, but for six of the eight possible starting octants RMS distance decreased from a mean of 0.861±0.067 mm after using the first octant to 0.813±0.026 mm after adding the second. When different combinations of octants were used simultaneously, accuracy increased with number of octants in a similar manner to the sequential method, although overall registration speed was significantly slower. Use of three octants gave a mean RMS distance of 0.812±0.025 mm. This suggests that registration using as little as a quarter of the defined ROI can be as accurate as using the full head. However, the method depends on defining the ROI, then using this to define octants. This is possible for the preoperative data, but may be more difficult for the surface capture data, depending on what parts of the surface are visible.

8.3 Comparison of ICP and CPD for noisy point clouds

One disadvantage of ICP is that it requires reasonably good initial global alignment in order to find the global minimum. Myronenko and Song [47] suggested that a probabilistic algorithm, Coherent Point Drift (CPD), is more robost to initial starting position and to noise than ICP. ICP and CPD were tested on ROI surface point clouds, as in chapter 4. CPD was used both without and with an option to prenormalise the data before registration and denormalise it afterwards, referred to as CPD1 and CPD2, respectively. Different starting positions were used, different levels of noise and smoothed noise were added to the point clouds, and the effect of prealignment using PCA was examined.

ICP achieved a mean RMS distance of 0.889±0.049 between point clouds, which was unaffected by the initial position of the point clouds (up to $\frac{\pi}{5}$ radians rotation). Noise level had no effect where the noisy point cloud was the source; where the noisy point cloud was the reference, RMS distance increased with noise level. This may be due to the algorithm registering the source to the edge of the noisy point cloud when it was the reference; it should be possible to alter the code to prevent this from happening. ICP performance may have been improved by the fact that the noise was evenly distributed about the surface. It is possible that unevenly distributed outliers could be more problematic for registration accuracy.

CPD1 results were similar to ICP for smaller initial transformations and low noise levels, but RMS distance increased for larger initial transformations and higher noise levels. Prealignment with PCA reduced higher RMS distances.

CPD2 results were poorer than ICP in all cases. Noise had no effect on accuracy. RMS distance increased with initial transformation, except when prealignment with PCA was used and the ground truth was the reference, when it decreased with initial transformation. Prealignment was associated with a small, non-significant, improvement in RMS distance. Smoothing the added noise made little difference to the results for any algorithm, although only one method and level of smoothing was tried.

8.4 3D Normal Distribution Transform

In chapter 6 a further probabilistic registration algorithm, the 3D Normal Distribution Transform (3D-NDT) algorithm, was tested and compared with ICP and CPD. Similarly to ICP, 3D-NDT was not affected by initial rotations of up to $\frac{\pi}{5}$ radians, although rotations of $\frac{\pi}{2}$ or more can lead to a local minimum for these ROI point clouds in which the heads are inverted with respect to each other. A mean RMS distance of 0.882±0.052 mm was achieved across all initial transformations, as compared with 0.884±0.048 mm for ICP. Where noise was used, RMS distance increased with noise level from 0.883±0.052 mm for 1% noise to 1.04±0.10 mm for 10% noise, where the noisy cloud was the source; similar results were obtained when the noisy cloud was the reference. This performance was poorer at higher noise levels than ICP, where the noisy point cloud was the source, although not where the noisy point cloud was the reference. The reasons for this are discussed above (section 8.3). Overall, ICP was the most accurate of the registration algorithms tested.

8.5 Accuracy at target point

In order to safely perform neurosurgical procedures, it is important that registration be sufficiently accurate at the target point within the head, as well as the entry point and the path in between. Submillimetre accuracy is essential for some applications, including the treatment of Parkinson's disease [56]. Full volume point clouds were extracted from the MRI data of the ten subjects used previously. Surface registration was performed as before using ICP. Each full volume point cloud was transformed to the location of the corresponding source surface point cloud before registration; the transformation calculated by the registration algorithm was then applied. The Euclidean distance of each point in the full volume point cloud from its starting position gave the error at that point.

Each point in the full volume point cloud was assigned to one of five regions within the head, so accuracy at the skin, skull, cerebrospinal fluid, white matter and grey matter could be determined. The results for each of the ten heads when initiallyl transformed by a positive rotation about the x-axis were similar, attained a median distance of 0.328±0.155 mm across all heads and regions. The effect of altering the initial rotation to be about the x-axis in the negative direction, or the y- and z-axes in either direction, was examined. Rotation about the z-axis was found to result in significantly larger errors: a median of 3.03±1.14 mm, as compared to 0.329±0.172 mm and 0.335±0.151 mm for x and y rotation, respectively. Using prealignment with PCA for the surface point clouds reduced the error, particularly for rotations about the z-axis, to a median of 0.272±0.066 mm for all initial rotations.

This is well within the submillimetre accuracy required in neurosurgery and compares well with reported application accuracies of 1.29 mm using fiducial markers [6] and 0.86±0.32 mm in a frame-based configuration [7]. However, registration accuracy has been examined using idealised point clouds only; surface capture images taken during surgery might be more noisy and less dense. Additionally, the full surface ROI might not be available and performing prealignment with PCA might not be practicable in these circumstances, which could reduce imaging accuracy. Finally, these errors are based on registration alone and do not take into account error due to the mechanical accuracy of the neurosurgical robot or the imaging device.

8.6 Limitations of this work

There are a number of limitations to this work. Most of the registration has been performed using idealised point clouds produced from MRI data. This was done in order that the errors caused by the registration algorithm might be kept separate from the errors inherent to any imaging device. However, while the idealised point clouds may be representative of the MRI data they were taken from, there is no guarantee that they are representative of surface capture data, of a surface obtainable from CT data, or even of the data available from a real preoperative MRI, which could have different signal weighting and contrast.

For much of the work only registration from an initial position of rotation about the x-axis was considered; when rotation about the y- and z-axes were considered, for ICP only, a much larger RMS error was the result for rotation about the z-axis. Additionally, each direction of rotation was considered separately and not in combination. Prealignment using principal component analysis was found to negate the negative effect of initial rotation about the z-axis, but would require a view of the full region of interest to be successful.

A robot system was not used to test the registration algorithms described and the work does not take into account the contributions from the target error of the robot or imaging system, testing only the potential registration algorithms. However, as reported in section 2.3.1.2, Kajita et al. [89] measure an RMS mechanical accuracy for the neuromate® of just 0.12±0.10 mm.

Scaling terms have not been considered as they were not required for the registrations tested. However, they could be necessary if the surface capture system of the preoperative CT/MRI data does not include absolute size data. The algorithms used here can be modified to include scaling terms.

Most of the registration methods would require a full view of the head, or would require the data to include the parts of the head (the inion and the nasion) which are needed to define the position of the octants on the head. Current neurosurgical practice does not necessarily require the whole head to be shaved for surgery, which makes obtaining a surface capture image of the head surface difficult. Only one way of splitting the ROI into parts was tested and registration accuracy may have been affected by the shape of the parts chosen. Partial registration using octants and by reducing point cloud density was only performed using the ICP algorithm, not CPD or 3D-NDT.

8.7 Further Work

It would be useful to test the algorithms, including scaling terms, with real surface capture point clouds, ideally taken under surgical conditions, to determine accuracy under these circumstances. It would also be useful to produce surface point clouds from corresponding CT and MRI data and register to these. Initial tests could be performed using a head-shaped CT/MRI compatible phantom, although the surfaces produced by CT/MRI scans of such a phantom might not be equivalent to those taken from human scans, in which case a human subject would be better. To determine the error in the registration algorithm, CT/MRI visible fiducial markers could be stuck to the outside of the phantom or subject. Registration would be performed using surface registration algorithms only; the resulting transformation would be applied to the fiducial markers in the source image, and the distance of these from the fiducial markers in the reference image would provide a measure of registration accuracy. If the physical shape of the markers affected the shape of the surface capture data, the markers could be replaced with pen marks for surface capture imaging. If the registration algorithm is ultimately used in surgery, intra-operative CT imaging could be performed to ensure accuracy.

As the full region of interest (ROI) head surface as used in this work might not easily be available for imaging, due to the patient's hair or to other obstacles that might be present during surgery, it would be useful to do further work to identify the parts of the head that could be practicably imaged: these could be used further to test the registration methods described. Possible other methods of defining the ROI could be devised, such as by using other features, perhaps the ears. Work would have to be done to ensure that the specific features used were not subject to distortion, or obscured during surgery. Methods of dividing up the ROI other than the octants used in chapter 4 could also be tested, by dividing into a different number of shapes or into a different pattern. This would rely on the ability to image appropriate features in order to define the relevant regions. These partial registration methods could also by tested with CPD, 3D-NDT and other suitable algorithms.

In addition to testing the algorithms with real data, a study using the neuromate®, or a similar stereotactic robot, would be beneficial. This could again be done in a phantom study, to determine registration accuracy with the algorithm and robot combined. The practicality and effect of mounting a surface capture device on a robot arm could be examined. As a range of tools and accessories can already be mounted on the neuromate®, developing a mountable imaging device is perfectly feasible. It would however be necessary for the position of the camera relative to the robot end effector to be known with a high degree of accuracy in order for registration to be successfully performed.

The registration methods used are relatively slow in their current implementation and it would be beneficial to reduce registration time as much as possible, especially if it is to be performed during surgery. Times taken for current neuromate® registration are in the region 5-10 minutes (see section 2.2.1), but a shorter time would be preferable for intra-operative registration. One method of increasing registration speed would be to simply use a sparser point clouds. Tests in chapter 4 using the ICP algorithm suggested that point cloud density could be reduced by up to 60% without reducing registration accuracy, but this was based on a surface extracted from MRI data only; more work would have to be done using surface point clouds extracted from CT and surface capture imaging to determine the necessary point cloud density for sufficiently accurate registration. Methods for improving ICP processing time could include using parallel processing or a k-d tree data structure. Machine/deep learning techniques could also be used to improve registration algorithm efficiency.

Bibliography

[1] Edward A Spiegel et al. “Stereotaxic apparatus for operations on the human brain”. In: *Science* 106.2754 (1947), pp. 349–350.

[2] Victor Horsley and Robert Henry Clarke. “The structure and functions of the cerebellum examined by a new method.” In: *Brain* 31.1 (1908), pp. 45–124.

[3] C Haegelen et al. “Stereotactic robot-guided biopsies of brain stem lesions: Experience with 15 cases”. In: *Neurochirurgie* 56.5 (2010), pp. 363–367.

[4] Wuttipong Tirakotai et al. “The evolution of stereotactic guidance in neuroendoscopy”. In: *Child’s Nervous System* 20.11-12 (2004), pp. 790–795.

[5] Francesco Cardinale et al. “Stereoelectroencephalography: surgical methodology, safety, and stereotactic application accuracy in 500 procedures”. In: *Neurosurgery* 72.3 (2013), pp. 353–366.

[6] TRK Varma and P Eldridge. “Use of the NeuroMate stereotactic robot in a frameless mode for functional neurosurgery”. In: *The International Journal of Medical Robotics and Computer Assisted Surgery* 2.2 (2006), pp. 107–113.

[7] Qing Hang Li et al. “The application accuracy of the NeuroMate robot - A quantitative comparison with frameless and frame-based surgical localization systems”. In: *Computer Aided Surgery* 7.2 (2002), pp. 90–98.

[8] Yik San Kwoh et al. “A robot with improved absolute positioning accuracy for CT guided stereotactic brain surgery”. In: *Biomedical Engineering, IEEE Transactions on* 35.2 (1988), pp. 153–160.

[9] Douglas R Ewing et al. “Robots in the operating room—the history”. In: *Surgical Innovation* 11.2 (2004), pp. 63–71.

[10] B Davies. “A review of robotics in surgery”. In: *Proceedings of the Institution of Mechanical Engineers, Part H: Journal of Engineering in Medicine* 214.1 (2000), pp. 129–140.

[11] Francisco PM Oliveira and Joao Manuel RS Tavares. “Medical image registration: a review”. In: *Computer methods in biomechanics and biomedical engineering* 17.2 (2014), pp. 73–93.

[12] Barbara Zitova and Jan Flusser. “Image registration methods: a survey”. In: *Image and vision computing* 21.11 (2003), pp. 977–1000.

[13] Jianwen Luo and Elisa E Konofagou. “A fast normalized cross-correlation calculation method for motion estimation”. In: *IEEE transactions on ultrasonics, ferroelectrics, and frequency control* 57.6 (2010), pp. 1347–1357.

[14] Y Raghavender Rao, Nikhil Prathapani, and E Nagabhooshanam. “Application of normalized cross correlation to image registration”. In: *International Journal of Research in Engineering and Technology* 3.5 (2014), pp. 12–16.

[15] Misganu Debella-Gilo and Andreas Kääb. “Sub-pixel precision image matching for measuring surface displacements on mass movements using normalized cross-correlation”. In: *Remote Sensing of Environment* 115.1 (2011), pp. 130–142.

[16] Milos Malinsky et al. “Registration of FA and T1-weighted MRI data of healthy human brain based on template matching and normalized cross-correlation”. In: *Journal of digital imaging* 26.4 (2013), pp. 774–785.

[17] Hassan Foroosh, Josiane B Zerubia, and Marc Berthod. “Extension of phase correlation to subpixel registration”. In: *IEEE transactions on image processing* 11.3 (2002), pp. 188–200.

[18] Daniel Foley et al. “Phase correlation applied to the 3D registration of CT and CBCT image volumes”. In: *Physica Medica: European Journal of Medical Physics* 32.4 (2016), pp. 618–624.

[19] Jakub Bican and Jan Flusser. “3D Rigid registration by cylindrical phase correlation method”. In: *Pattern Recognition Letters* 30.10 (2009), pp. 914–921.

[20] Ilker Hacihaliloglu et al. “Non-iterative partial view 3D ultrasound to CT registration in ultrasound-guided computer-assisted orthopedic surgery”. In: *International journal of computer assisted radiology and surgery* 8.2 (2013), pp. 157–168.

[21] Josien PW Pluim, JB Antoine Maintz, and Max A Viergever. “Mutual-information-based registration of medical images: a survey”. In: *IEEE transactions on medical imaging* 22.8 (2003), pp. 986–1004.

[22] Adrian Andronache et al. “Non-rigid registration of multi-modal images using both mutual information and cross-correlation”. In: *Medical image analysis* 12.1 (2008), pp. 3–15.

[23] Dirk Loeckx et al. “Nonrigid image registration using conditional mutual information”. In: *IEEE transactions on medical imaging* 29.1 (2010), pp. 19–29.

[24] Jiann-Der Lee et al. “Medical augment reality using a markerless registration framework”. In: *Expert Systems with Applications* 39.5 (2012), pp. 5286–5294.

[25] Jiaolong Yang, Hongdong Li, and Yunde Jia. “Go-icp: Solving 3d registration efficiently and globally optimally”. In: *Computer Vision (ICCV), 2013 IEEE International Conference on*. IEEE. 2013, pp. 1457–1464.

[26] Daniel Münch, Benoît Combès, and Sylvain Prima. “A modified ICP algorithm for normal-guided surface registration”. In: *Medical Imaging 2010: Image Processing*. Vol. 7623. International Society for Optics and Photonics. 2010, 76231A.

[27] Yang Chen and Gérard Medioni. “Object modelling by registration of multiple range images”. In: *Image and vision computing* 10.3 (1992), pp. 145–155.

[28] Aleksandr Segal, Dirk Haehnel, and Sebastian Thrun. “Generalized-icp.” In: *Robotics: science and systems*. Vol. 2. 4. 2009, p. 435.

[29] Jacopo Serafin and Giorgio Grisetti. “NICP: Dense normal based point cloud registration”. In: *Intelligent Robots and Systems (IROS), 2015 IEEE/RSJ International Conference on*. IEEE. 2015, pp. 742–749.

[30] Sangkyun Shin et al. “Markerless registration for intracerebral hemorrhage surgical system using weighted Iterative Closest Point (ICP)”. In: *Engineering in Medicine and Biology Society (EMBC), 2012 Annual International Conference of the IEEE*. IEEE. 2012, pp. 5306–5309.

[31] Lei Zhang, Sung-In Choi, and Soon-Yong Park. “Robust ICP registration using biunique correspondence”. In: *3D Imaging, Modeling, Processing, Visualization and Transmission (3DIMPVT), 2011 International Conference on*. IEEE. 2011, pp. 80–85.

[32] Alexander Schmidt-Richberg et al. “Diffeomorphic diffusion registration of lung CT images”. In: *Medical Image Analysis for the Clinic: A Grand Challenge* (2010), pp. 55–62.

[33] Yipeng Hu et al. "Deformable vessel-based registration using landmark-guided coherent point drift". In: *International Workshop on Medical Imaging and Virtual Reality*. Springer. 2010, pp. 60–69.

[34] Martin Koch et al. "Towards deformable shape modeling of the left atrium using non-rigid coherent point drift registration". In: *Bildverarbeitung für die Medizin 2013*. Springer, 2013, pp. 332–337.

[35] Parastoo Farnia et al. "An efficient point based registration of intra-operative ultrasound images with MR images for computation of brain shift; A phantom study". In: *Engineering in Medicine and Biology Society, EMBC, 2011 Annual International Conference of the IEEE*. IEEE. 2011, pp. 8074–8077.

[36] Renbo Xia, Jibin Zhao, and Yunpeng Liu. "A robust feature-based registration method of multimodal image using phase congruency and coherent point drift". In: *MIPPR 2013: Pattern Recognition and Computer Vision*. Vol. 8919. International Society for Optics and Photonics. 2013, p. 891903.

[37] Martin Magnusson. "The three-dimensional normal-distributions transform: an efficient representation for registration, surface analysis, and loop detection". PhD thesis. Örebro universitet, 2009.

[38] Todor Stoyanov, Martin Magnusson, and Achim J Lilienthal. "Point set registration through minimization of the L 2 distance between 3D-NDT models". In: *Robotics and Automation (ICRA), 2012 IEEE International Conference on*. IEEE. 2012, pp. 5196–5201.

[39] Ramtin Shams et al. "A survey of medical image registration on multicore and the GPU". In: *IEEE Signal Processing Magazine* 27.2 (2010), pp. 50–60.

[40] Geert Litjens et al. “A survey on deep learning in medical image analysis”. In: *Medical image analysis* 42 (2017), pp. 60–88.

[41] Xi Cheng, Li Zhang, and Yefeng Zheng. “Deep similarity learning for multimodal medical images”. In: *Computer Methods in Biomechanics and Biomedical Engineering: Imaging & Visualization* 6.3 (2018), pp. 248–252.

[42] Martin Simonovsky et al. “A deep metric for multimodal registration”. In: *International Conference on Medical Image Computing and Computer-Assisted Intervention*. Springer. 2016, pp. 10–18.

[43] Guorong Wu et al. “Unsupervised deep feature learning for deformable registration of MR brain images”. In: *International Conference on Medical Image Computing and Computer-Assisted Intervention*. Springer. 2013, pp. 649–656.

[44] Xiao Yang, Roland Kwitt, and Marc Niethammer. “Fast predictive image registration”. In: *Deep Learning and Data Labeling for Medical Applications*. Springer, 2016, pp. 48–57.

[45] Shun Miao, Z Jane Wang, and Rui Liao. “A CNN regression approach for real-time 2D/3D registration”. In: *IEEE transactions on medical imaging* 35.5 (2016), pp. 1352–1363.

[46] Michael Jermyn et al. “Fast segmentation and high-quality three-dimensional volume mesh creation from medical images for diffuse optical tomography”. In: *Journal of biomedical optics* 18.8 (2013), pp. 086007–086007.

[47] Andriy Myronenko and Xubo Song. “Point set registration: Coherent point drift”. In: *Pattern Analysis and Machine Intelligence, IEEE Transactions on* 32.12 (2010), pp. 2262–2275.

[48] Kevin Cleary and Charles Nguyen. “State of the art in surgical robotics: clinical applications and technology challenges”. In: *Computer Aided Surgery* 6.6 (2001), pp. 312–328.

[49] Stephane Lavallee et al. “Image guided operating robot: a clinical application in stereotactic neurosurgery”. In: *Robotics and Automation, 1992. Proceedings., 1992 IEEE International Conference on*. IEEE. 1992, pp. 618–624.

[50] JB Maintz and Max A Viergever. “A survey of medical image registration”. In: *Medical image analysis* 2.1 (1998), pp. 1–36.

[51] Takashi Mitsui et al. “Skin shift and its effect on navigation accuracy in image-guided neurosurgery”. In: *Radiological physics and technology* 4.1 (2011), pp. 37–42.

[52] Hjalmar Bjartmarz and Stig Rehncrona. “Comparison of accuracy and precision between frame-based and frameless stereotactic navigation for deep brain stimulation electrode implantation”. In: *Stereotactic and functional neurosurgery* 85.5 (2007), pp. 235–242.

[53] Maarten Bot et al. “Analysis of stereotactic accuracy in patients undergoing deep brain stimulation using Nexframe and the Leksell frame”. In: *Stereotactic and functional neurosurgery* 93.5 (2015), pp. 316–325.

[54] Justin S Smith et al. “Frame-based stereotactic biopsy remains an important diagnostic tool with distinct advantages over frameless stereotactic biopsy”. In: *Journal of neuro-oncology* 73.2 (2005), pp. 173–179.

[55] Ruben Dammers et al. “Safety and efficacy of frameless and frame-based intracranial biopsy techniques”. In: *Acta neurochirurgica* 150.1 (2008), pp. 23–29.

[56] Junchuan Liu, Yuru Zhang, and Zhen Li. “The application accuracy of neuromaster: a robot system for stereotactic neurosurgery”. In: *Mechatronic and Embedded Systems and Applications, Proceedings of the 2nd IEEE/ASME International Conference on*. IEEE. 2006, pp. 1–5.

[57] Peter A Woerdeman et al. “Application accuracy in frameless image-guided neurosurgery: a comparison study of three patient-to-image registration methods”. In: *Journal of neurosurgery* 106.6 (2007), pp. 1012–1016.

[58] Martin Ortler et al. “Frame-based vs frameless placement of intrahippocampal depth electrodes in patients with refractory epilepsy: a comparative in vivo (application) study”. In: *Neurosurgery* 68.4 (2011), pp. 881–887.

[59] Colors Magazine. 2014. URL: `http://www.colorsmagazine.com/stories/magazine/83/story/switch-on-your-brightest-smile`.

[60] Renishaw plc. 2014. URL: `http://www.renishaw.com`.

[61] Tobias A Mattei et al. “Current state-of-the-art and future perspectives of robotic technology in neurosurgery”. In: *Neurosurgical review* (2014), pp. 1–10.

[62] Renishaw plc. *Statement of Clarification*. Online. Published: 15th January 2014. Accessed: 11th June 2014. URL: `http://www.renishaw.com/en/statement-of-clarification--24144`.

[63] Kumar Abhinav, Savithru Prakash, and David R Sandeman. “Use of robot-guided stereotactic placement of intracerebral electrodes for investigation of focal epilepsy: initial experience in the UK”. In: *British journal of neurosurgery* 27.5 (2013), pp. 704–705.

[64] Afif Afif et al. “Anatomofunctional organization of the insular cortex: a study using intracerebral electrical stimulation in epileptic patients”. In: *Epilepsia* 51.11 (2010), pp. 2305–2315.

[65] Renishaw plc. *Neuromate Technical Data Sheet H-4149-0032-02-A*. URL: `http://resources.renishaw.com/details/Data+sheet%3A+neuromate%C2%AE+stereotactic+robot+system(169731)(52312)`.

[66] Ruben Geevarghese et al. “Registration accuracy of CT/MRI fusion for localisation of deep brain stimulation electrode position: an imaging study and systematic review”. In: *Stereotactic and functional neurosurgery* 94.3 (2016), pp. 159–163.

[67] Jorge Gonzalez-Martinez et al. “Robot-assisted stereotactic laser ablation in medically intractable epilepsy: operative technique”. In: *Operative Neurosurgery* 10.2 (2014), pp. 167–173.

[68] Michel Lefranc et al. “Frameless robotic stereotactic biopsies: a consecutive series of 100 cases”. In: *Journal of neurosurgery* 122.2 (2015), pp. 342–352.

[69] Michel Lefranc et al. “The impact of the reference imaging modality, registration method and intraoperative flat-panel computed tomography on the accuracy of the ROSA® stereotactic robot”. In: *Stereotactic and Functional neurosurgery* 92.4 (2014), pp. 242–250.

[70] Demitre Serletis et al. “The stereotactic approach for mapping epileptic networks: a prospective study of 200 patients”. In: *Journal of neurosurgery* 121.5 (2014), pp. 1239–1246.

[71] Sumeet Vadera et al. “Frameless stereotactic robot-assisted subthalamic nucleus deep brain stimulation: case report”. In: *World neurosurgery* 97 (2017), 762–e11.

[72] Nicholas Brandmeir, Vinita Acharya, and Michael Sather. “Robot assisted stereotactic laser ablation for a radiosurgery resistant hypothalamic hamartoma”. In: *Cureus* 8.4 (2016).

[73] Mayur Jayarao and Lawrence S Chin. “Robotics and its applications in stereotactic radiosurgery”. In: *Neurosurgical Focus* 23.6 (2007), E5. DOI: `10.3171/FOC-07/12/E6`.

[74] W Kilby et al. “The CyberKnife® robotic radiosurgery system in 2010”. In: *Technology in cancer research & treatment* 9.5 (2010), pp. 433–452.

[75] Anthony K Ho et al. “A study of the accuracy of cyberknife spinal radiosurgery using skeletal structure tracking”. In: *Operative Neurosurgery* 60.suppl_2 (2007), ONS–147.

[76] Dongshan Fu and Gopinath Kuduvalli. “A fast, accurate, and automatic 2D–3D image registration for image-guided cranial radiosurgery”. In: *Medical physics* 35.5 (2008), pp. 2180–2194.

[77] Zhiping Mu, Dongshan Fu, and Gopinath Kuduvalli. “Multiple fiducial identification using the hidden Markov model in image guided radiosurgery”. In: *Computer Vision and Pattern Recognition Workshop, 2006. CVPRW’06. Conference on*. IEEE. 2006, pp. 92–92.

[78] Claire Montgomery and Mark Collins. “An evaluation of the BrainLAB 6D ExacTrac/Novalis Tx System for image-guided intracranial radiotherapy”. In: *Journal of Radiotherapy in Practice* 16.3 (2017), pp. 326–333.

[79] Naoki Hayashi et al. “Assessment of spatial uncertainties in the radiotherapy process with the Novalis system”. In: *International Journal of Radiation Oncology • Biology • Physics* 75.2 (2009), pp. 549–557.

[80] Thierry Gevaert et al. “Setup accuracy of the Novalis ExacTrac 6DOF system for frameless radiosurgery”. In: *International Journal of Radiation Oncology • Biology • Physics* 82.5 (2012), pp. 1627–1635.

[81] Jian-Yue Jin et al. “2D/3D image fusion for accurate target localization and evaluation of a mask based stereotactic system in fractionated stereotactic radiotherapy of cranial lesions”. In: *Medical physics* 33.12 (2006), pp. 4557–4566.

[82] XL Chen et al. “Deep brain stimulation”. In: *Interventional neurology* 1.3-4 (2013), pp. 200–212.

[83] Wilder Penfield and Edwin Boldrey. “Somatic motor and sensory representation in the cerebral cortex of man as studied by electrical stimulation.” In: *Brain: A journal of neurology* (1937).

[84] Joel S Perlmutter and Jonathan W Mink. “Deep brain stimulation”. In: *Annual review of neuroscience* 29 (2006), p. 229.

[85] MR Bergström et al. “Electrical stimulation of the thalamic and subthalamic area in cerebral palsy”. In: *Acta physiologica Scandinavica* 67.2 (1966), pp. 208–213.

[86] CW Sem-Jacobsen. “Depth electrographic stimulation and treatment of patients with Parkinson’s disease including neurosurgical technique”. In: *Acta Neurologica Scandinavica* 41.S13 (1965), pp. 365–376.

[87] Patricia Limousin et al. “Effect on parkinsonian signs and symptoms of bilateral subthalamic nucleus stimulation”. In: *The Lancet* 345.8942 (1995), pp. 91–95.

[88] AL Benabid et al. “Long-term electrical inhibition of deep brain targets in movement disorders”. In: *Movement Disorders* 13.S3 (1998), pp. 119–125.

[89] Yasukazu Kajita et al. "Installation of a Neuromate Robot for Stereotactic Surgery: Efforts to Conform to Japanese Specifications and an Approach for Clinical Use—Technical Notes". In: *Neurologia medico-chirurgica* 55.12 (2015), p. 907.

[90] Sorin Breit, Jörg B Schulz, and Alim-Louis Benabid. "Deep brain stimulation". In: *Cell and tissue research* 318.1 (2004), pp. 275–288.

[91] Charles N Munyon et al. "Accuracy of frame-based stereotactic depth electrode implantation during craniotomy for subdural grid placement". In: *Stereotactic and functional neurosurgery* 91.6 (2013), pp. 399–403.

[92] Jorge González-Martínez et al. "Technique, results, and complications related to robot-assisted stereoelectroencephalography". In: *Neurosurgery* 78.2 (2016), pp. 169–180.

[93] Kathryn L Holloway et al. "Frameless stereotaxy using bone fiducial markers for deep brain stimulation". In: *Journal of neurosurgery* 103.3 (2005), pp. 404–413.

[94] Daniel von Langsdorff, Philippe Paquis, and Denys Fontaine. "In vivo measurement of the frame-based application accuracy of the Neuromate neurosurgical robot". In: *Journal of neurosurgery* 122.1 (2015), pp. 191–194.

[95] Peter C Warnke and Ashley Ralston. "Image-Guided Brain Biopsy". In: *Image-Guided Neurosurgery* (2015), p. 193.

[96] Timothy Lee et al. "Supratentorial masses: stereotactic or freehand biopsy?" In: *British journal of neurosurgery* 5.4 (1991), pp. 331–338.

[97] Walter A Hall. "The safety and efficacy of stereotactic biopsy for intracranial lesions". In: *Cancer* 82.9 (1998), pp. 1749–1755.

[98] Sodaba Khatab, Wim Spliet, and Peter A Woerdeman. "Frameless image-guided stereotactic brain biopsies: emphasis on diagnostic yield". In: *Acta neurochirurgica* 156.8 (2014), pp. 1441–1450.

[99] JD Caird and JM Drake. "Technical aspects of image-guided neuroendoscopy". In: *Textbook of Stereotactic and Functional Neurosurgery*. Springer, 2009, pp. 807–813.

[100] Florian H Ebner et al. "Developments in neuroendoscopy: trial of a miniature rigid endoscope with a multidirectional steerable tip camera in the anatomical lab". In: *Neurosurgical review* 35.1 (2012), pp. 45–51.

[101] Henry WS Schroeder et al. "Frameless neuronavigation in intracranial endoscopic neurosurgery". In: *Journal of neurosurgery* 94.1 (2001), pp. 72–79.

[102] Hector RA Basevi et al. "Simultaneous multiple view high resolution surface geometry acquisition using structured light and mirrors". In: *Optics express* 21.6 (2013), pp. 7222–7239.

[103] Paolo Cignoni, Massimiliano Corsini, and Guido Ranzuglia. "Meshlab: an open-source 3d mesh processing system". In: *Ercim news* 73.45-46 (2008), p. 6.

[104] Barak Freedman et al. "Depth mapping using projected patterns". Pat. US20100118123 A1. US Patent 8,493,496. 2013.

[105] Tilak Dutta. "Evaluation of the Kinect$^{\text{TM}}$ sensor for 3-D kinematic measurement in the workplace". In: *Applied ergonomics* 43.4 (2012), pp. 645–649.

[106] Shahram Izadi et al. "KinectFusion: real-time 3D reconstruction and interaction using a moving depth camera". In: *Proceedings of the 24th annual ACM symposium on User interface software and technology*. ACM. 2011, pp. 559–568.

[107] Visual Computing Lab ISTI — CNR. *MeshLab*. http://meshlab.sourceforge.net/.

[108] Xue Wu. “Atlas based image reconstruction for diffuse optical imaging of the human brain”. PhD thesis. University of Birmingham, 2016.

[109] Paul J Besl and Neil D McKay. “Method for registration of 3-D shapes”. In: *Robotics-DL tentative*. International Society for Optics and Photonics. 1992, pp. 586–606.

[110] Wolfgang Kabsch. “A solution for the best rotation to relate two sets of vectors”. In: *Acta Crystallographica Section A: Crystal Physics, Diffraction, Theoretical and General Crystallography* 32.5 (1976), pp. 922–923.

[111] Wolfgang Kabsch. “A discussion of the solution for the best rotation to relate two sets of vectors”. In: *Acta Crystallographica Section A: Crystal Physics, Diffraction, Theoretical and General Crystallography* 34.5 (1978), pp. 827–828.

[112] Jakob Wilm. *Iterative Closest Point - File Exchange - MATLAB Central*. 2010. URL: http://www.mathworks.co.uk/matlabcentral/fileexchange/27804-iterative-closest-point.

[113] Gaël Guennebaud, Marcel Germann, and Markus Gross. “Dynamic sampling and rendering of algebraic point set surfaces”. In: *Computer Graphics Forum*. Vol. 27. 2. Wiley Online Library. 2008, pp. 653–662.

[114] Inc. The MathWorks. *MATLAB Release 2013a*. Natick, Massachusetts, United States, 2013.

[115] Andriy Myronenko, Xubo Song, and Miguel A Carreira-Perpinán. “Non-rigid point set registration: Coherent point drift”. In: (2006), pp. 1009–1016.

[116] Jennifer R Cutter et al. “Image-based Registration for a Neurosurgical Robot: Comparison Using Iterative Closest Point and Coherent Point Drift Algorithms”. In: *Procedia Computer Science* 90 (2016), pp. 28–34.

[117] Lei Peng et al. “Robust CPD Algorithm for Non-Rigid Point Set Registration Based on Structure Information”. In: *PloS one* 11.2 (2016), e0148483.

[118] R Core Team. *R: A Language and Environment for Statistical Computing*. R Foundation for Statistical Computing. Vienna, Austria, 2016. URL: `https://www.R-project.org`.

[119] Yoav Benjamini and Yosef Hochberg. “Controlling the false discovery rate: a practical and powerful approach to multiple testing”. In: *Journal of the royal statistical society. Series B (Methodological)* (1995), pp. 289–300.

[120] Andrew W Fitzgibbon. “Robust registration of 2D and 3D point sets”. In: *Image and Vision Computing* 21.13-14 (2003), pp. 1145–1153.

[121] Cihan Ulaş and Hakan Temeltaş. “3D multi-layered normal distribution transform for fast and long range scan matching”. In: *Journal of Intelligent & Robotic Systems* (2013), pp. 1–24.

[122] Peter Biber and Wolfgang Straßer. “The normal distributions transform: A new approach to laser scan matching”. In: *Intelligent Robots and Systems, 2003.(IROS 2003). Proceedings. 2003 IEEE/RSJ International Conference on*. Vol. 3. IEEE. 2003, pp. 2743–2748.

[123] Peter Biber, Sven Fleck, and Wolfgang Strasser. “A probabilistic framework for robust and accurate matching of point clouds”. In: *Pattern Recognition*. Springer, 2004, pp. 480–487.

[124] Todor Stoyanov et al. “On the accuracy of the 3D normal distributions transform as a tool for spatial representation”. In: *Robotics and Automation (ICRA), 2011 IEEE International Conference on*. IEEE. 2011, pp. 4080–4085.

[125] Jorge J Moré and David J Thuente. “Line search algorithms with guaranteed sufficient decrease”. In: *ACM Transactions on Mathematical Software (TOMS)* 20.3 (1994), pp. 286–307.

[126] Radu Bogdan Rusu and Steve Cousins. “3d is here: Point cloud library (pcl)”. In: *Robotics and Automation (ICRA), 2011 IEEE International Conference on*. IEEE. 2011, pp. 1–4.